Studying the molecular determinants of potassium channel structure and function in membranes by solid-state NMR

Elwin A. W. van der Cruijsen

Studying the molecular determinants of potassium channel structure and function in membranes by solid-state NMR

Vaste-stof NMR studie naar de moleculaire determinanten van de structuur en functie van een kaliumkanaal in membranen

(met een samenvatting in het Nederlands)

Proefschrift

ter verkrijging van de graad van doctor aan de Universiteit Utrecht op gezag van de rector magnificus, prof.dr. G.J. van der Zwaan, ingevolge het besluit van het college voor promoties in het openbaar te verdedigen op woensdag 29 oktober 2014 des middags te 2.30 uur

door

Elwin Antonius Wilhelmus van der Cruijsen

geboren op *18 januari 1985 te Schoonhoven*

Promotor: Prof.dr. M. Baldus

TABLE OF CONTENTS

General Introduction

Membrane proteins

Building compartments is necessary in every living organism to isolate cells from the external environment; to allow cell differentiation and to form cell organelles. These compartments are predominantly assembled by lipid bilayers/membranes. Lipids are composed of a hydrophilic polar head group and hydrophobic nonpolar tails. In an aqueous environment, these molecules assemble together to lipid bilayers by hydrophobic forces. To connect to the molecular environment, to provide a cell with nutrients or build chemical gradients, proteins that span membranes are required (see Figure 1). These proteins have to execute their function in a highly anisotropic environment consisting of the polar region around the lipid head group, the lipophilic bilayer core and an aqueous medium at the membrane periphery.

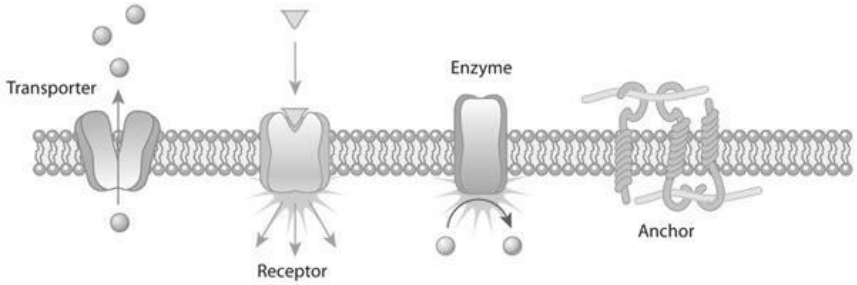

Figure 1 Classification of cellular functions executed by membrane proteins. These include cellular transport, signal recognition and transduction, enzymatic catalysis and cell adhesion as well as anchoring to, for example, the cytoskeleton. Cartoon taken from Ref. [1].

Ion Channels

To balance ion gradients across the membrane, membrane-embedded ion channels act as valves that mediate the selective passage of ions along their concentration gradient. Ion channels have a crucial role in cell signaling, electrical excitability, muscle contraction, cell secretion, signal transduction and gene transcription. To do this in an ordered manner, ion channels are sensitive to specific stimuli such as voltage, ligands, pH or mechanical force.[2]

Potassium channels

The largest and most diverse group amongst ion channel class[2,3] are potassium channels. By selectively conducting K^+ over Na^+, K^+ channels ensure stabilization of the resting membrane potential. For excitable cells, K^+ channels set the resting potential, keep action potentials short and terminate periods of intense activity.[2,4] For some channels, experimental evidence for high concentration and cluster formation has been given.[5,6] The topology of the so called pore-loop class[2] varies in terms of the number of α-helices spanning the lipid bilayer, mainly comprising two or six transmembrane (TM) helices (Figure 2). Channels with six TM are often voltage-gated. These channels are activated by changes in electrical potential near the channel and are critical for, e.g., neurons.

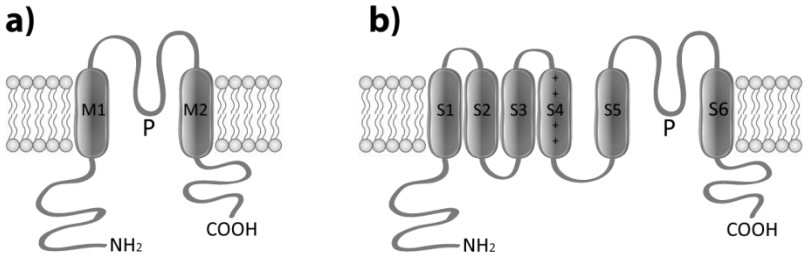

Figure 2. (a) 2TM/P channels which consist of two transmembrane helices with a pore-loop between them, exemplified by inwardly rectifying K^+ channels and by bacterial K^+ channels of the KcsA family. (b) 6TM/P channels, which are the predominant class among ligand-gated and voltage-gated K^+ channels.

KcsA as a prototype.

The simplest architecture within the K^+ channel family consists of two TM helices connected by a pore-loop, representing the structural core of all K^+ channels. The common underlying structural feature of K^+ channels is the so-called pore-lining P-loop containing the highly conserved signature sequence TXGYG.[7] As K^+ channels are tetramers, this signature sequence jointly forms the pore, which selectively conducts K^+ ions, which is also known as the selectivity filter (SF). Similar to the inward-rectifier channel family, the potassium channel from *Streptomyces lividans* (KcsA)[8] gram-positive soil bacterium consists of these two TMs (TM1 and TM2) connected by a pore domain (Figure 3). This pH-gated channel was discovered in 1995 and, because of the high expression in *E. coli* and the limited protein size, became an ideal candidate for structural and functional analysis.[9–16]

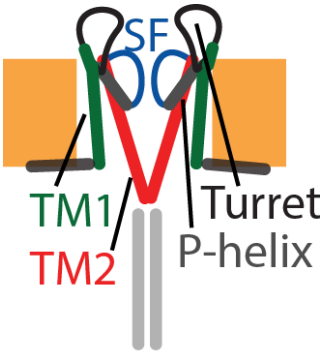

Figure 3. Structural cartoon of KcsA indicating the different regions of the channel topology. Two of the four subunits are drawn for visual clarity.

Function

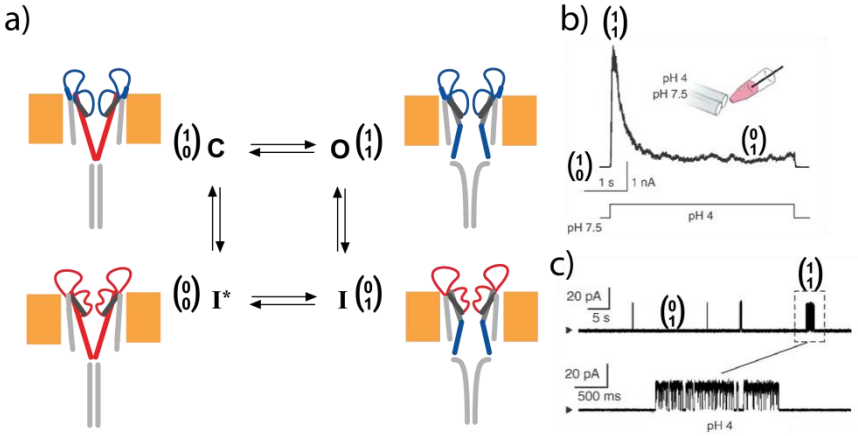

Figure 4. (a) Schematic gating cycle of KcsA with (b) the macroscopic currents activated by a rapid pH jump followed up by inactivation and (c) single-channel steady-state recordings of KcsA obtained in symmetric KCl pH 4 solution are dominated by long closures with short activity-burst. At macroscopic currents and single-channel steady-state recordings the conformational state are indicated. (b) and (c) were adapted from Ref. [12].

The function of KcsA can be explained as a gating cycle.[12,17–23] In the resting state of the channel (1|0) (see Figure 4a), the SF is conductive and the (activation) gate is closed. Upon acid titration the cytoplasmic residues of the activation gate become protonated and repel each other.[23,15] As a result, the TM2 helix moves out, leaving the permeation

pathway open for ions, corresponding to the transition (1|0) to (1|1) in Figure 4b.[12] For a short period in which the channel adopts this (1|1) conformation, ions can flow across the membrane. As shown by the exponential decay from macroscopic patch clamp recordings upon pH-activation, there is a second gating mechanism. As the selectivity filter is not stable when the gate is open it will adopt a collapsed conformation, a process which is called inactivation (corresponding to state (0|1)).[17,18] From the macroscopic response there is no recovery in conductivity of the selectivity filter compared to the original ion flow. Nevertheless the open inactive channel can exhibit an activity-burst on the timescale of milliseconds leading back to the (1|1) conformation. This process can be studied by single channel steady-state recordings where, if there is an activity-burst, give information on the type of conductivity mode (see 'modal gating' below). To complete the gating cycle, the channel returns to the closed collapse (0|0) state. Early structural information on this process was obtained by X-ray crystallography which determined the (1|0) and (0|0) conformations of KcsA in 2001 with a resolution of 2 Å[9].

Modal gating

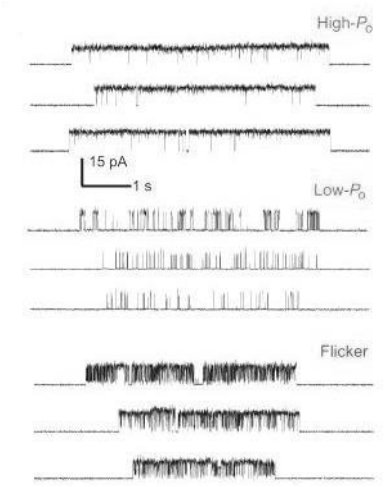

Figure 5 KcsA displays a highly variable kinetic behavior which arises from a combination of three distinct modes of channel activity. Traces are taken from Ref.[24].

Under single channel steady-state conditions, in which the transition between (1|1) and (0|1) is visible, KcsA can show three distinct gating modes, High open probability(P_O), low-P_O and a high-frequency flicker mode[24]. Even during a burst, the channel can abruptly switch between these gating modes, which is a common feature of K^+ channels. To study structure and function of these different gating modes Perozo et al[24] mutated residue E71. This strategy reduced the entry into the C-type inactivated state and stabilized, depending on the residue at position 71, the three kinetically defined gating modes. Residue E71 is situated at the pore helix at the back of the selectivity filter and is, together with W67 and

D80, part of a functionally important triad, which in turn is embedded in a larger hydrogen-bond network.

Lipid dependence

In general, the lipid bilayer actively participates in the control of membrane protein folding, diffusion and function.[25–30] Moreover, the lipid environment can directly influence the function of membrane proteins, including the working of K^+ channels.[26,28,29,31–33]
In particular, functional studies of KcsA showed that negatively charged anionic phospholipids are crucial for KcsA function. [27,31,33] Furthermore, single channel steady-state recordings revealed that Phosphatidylglycerol (PG) stabilizes the open state (1|1), of the channel and simultaneously increases conductance. [27]

Solid-state NMR

In order to investigate the structural basis of membrane protein function, solid-state Nuclear Magnetic Resonance (ssNMR) spectroscopy can be applied. The advantages of using ssNMR spectroscopy for structural investigations of membrane proteins are: (1) no size restriction for the protein to be studied, (2) considerable sample preparative freedom to work with microcrystals or gels and (3) the ability to study structure-function relationship in complex membrane systems in native-like cellular settings. In general ssNMR spectra are influenced by the combined effect of spatial and magnetic interactions of the nuclear spins. In the context of this thesis, the main interactions are:
-The chemical shift is based on the interaction of the external magnetic field with the nucleus via its surrounding electrons. Due to their different electronic environment, the nuclei experience slightly different local magnetic fields. In ssNMR, the chemical shift has an isotropic and an orientation-dependent anisotropic contribution (known as chemical shift anisotropy (CSA)).
-Dipolar couplings are magnetic interactions between nuclei through space. They depend on the internuclear distance and orientation relative to the external magnetic field.
-Scalar couplings are indirect magnetic interactions of nuclei through electron bonds. These isotropic interactions are however usually small in comparison to the dipolar couplings and the CSA.
The presence of the above-mentioned ssNMR interactions, especially of dipolar couplings and CSA, leads to broad spectral lines in static solids.

To obtain information at atomic level, anisotropic interactions can be suppressed by manipulating the spatial as well as the spin components of ssNMR Hamiltonian. While spin decoupling can average the spin part, Magic angle spinning (MAS)[34], i.e., rotating the sample at an angle of 54.7 degrees with respect to the external magnetic field, is usually applied to average out the spatial part of such interactions (see Figure 6). If the spinning rate exceeds the largest interaction of the considered spin species, it will lead to time-averaging of the anisotropic spin-interactions leaving only isotropic contributions.

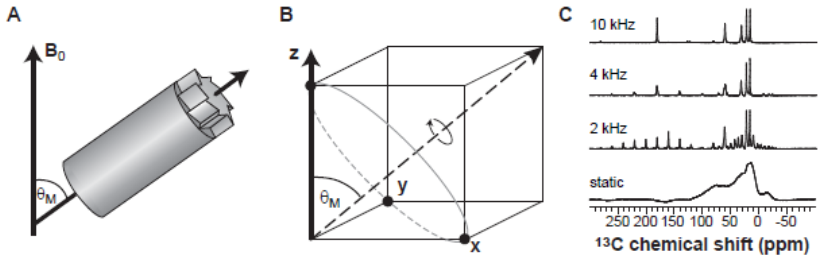

Figure 6. The sample rotor (a) with spinning axis aligned at the magic angle with respect to the external magnetic field B_0 creates a cubic symmetry at this magic angle (b). ^{13}C spectra of uniformly labeled valine obtained with various MAS rates. (b) and (c) is taken from[35,36], respectively.

On the other hand, anisotropic dipolar interactions provide a rich source of structural information, coding for internuclear distances. Therefore, recoupling sequences[37] are used to reintroduce such anisotropic interaction in a controlled manner without losing high-resolution information under MAS conditions.

Dynamic Nuclear Polarization. Since sensitivity is one of the major issues of NMR, the spectroscopic sensitivity can be enhanced by choosing recoupling sequences which transfer polarization from high-γ nuclei to low-γ nuclei through dipolar couplings.[38,39] As a consequence, the signal to noise can for, be considerably increase, for example by using cross polarization [38,40] from ^1H to ^{13}C nuclei. To further enhance the ssNMR signal, dynamic nuclear polarization transfer (DNP[41]) that transfers polarization from unpaired electrons is gaining increased attention. Electrons have a gyromagnetic ratio that is 660 higher than ^1H.[42] Today, DNP experiments can be conducted on commercially available ssNMR spectrometers equipped with a gyrotron, where microwaves are created to irradiate the ssNMR sample containing polarizable (bi)radicals. For optimal signal enhancement, DNP experiments thus far have been conducted at low temperatures (LT)

around 100 K. In practice, measures are usually taken to cryoprotect biological samples and soluble DNP agents are contained a glassy matrix. The application of low-temperature (LT)-DNP in combination of MAS[34] and the use of paramagnetic polarizing agents has been employed with increasing applications in material[43] and life sciences[44]. For example, LT-DNP under MAS has been used to study membrane-associated peptides[45,46] as well as intermediate[47] and ligand-bound membrane protein states[48–50]. In addition, DNP-MAS has been successfully applied on cellular preparations[51–53] and can be used to examine large macromolecular complexes[54].

Scope of this thesis

Using solid-state NMR studies in combination with electrophysiological experiments and molecular dynamics simulations we can deal with increasingly complex bimolecular systems. In this thesis, such approaches are used to address important aspects of the membrane-embedded protein structure of KcsA and its variants in different functional states that so far have remained elusive.

In **chapter 2**, we show that the turret region connecting the outer transmembrane (TM1) helix and the pore helix behind the selectivity filter contributes to K^+ channel inactivation. This finding suggests that the interaction between the K^+ channel turret region and the lipid bilayer exerts an important influence on the selective passage of K^+ through the channel pore. Moreover, the TM1 helix unwinds when the K^+ channel undergoes inactivation and rewinds during the transition to the conductive state.

In **Chapter 3**, we compare structural and functional parameters of specific lipid binding to KcsA and chimeric KcsA-Kv1.3. While the KcsA activity is critically modulated by the specific and cooperative binding of anionic nonannular lipids close to the channel's selectivity filter, the influence of anionic nonannular lipids on KcsA-Kv1.3 is reduced. The diminishing impact can be explained by a point mutation at the corresponding nonannular lipid binding site.

In **Chapter 4**, we show using electrophysiological experiments that strong negatively charged phosphatidic acid (PA) and cardiolipin (CL) stabilize the open state of KcsA and reduce inactivation of the channel. This effect leads to an increase of overall steady state open-probability (Po) of KcsA. The maximal Po of the KcsA was observed for channels in CL lipid bilayer. By ssNMR experiments, we for the first time demonstrate that in CL lipid bilayer the open-conductive conformation of a native K^+ channel pore can be detected.

Chapter 5 we use proton-detected ssNMR on fully protonated channels to probe the existence of water molecules with long residence times at the rear of the selectivity filter, explaining the long recovery kinetics of the inactivation gate.

Chapter 6 focuses on the DNP-enhanced ssNMR experiments. Applied to membrane-embedded KcsA, such studies revealed two conformations for the open activation gate, which is in line with observed low-resolution crystallographic studies using a multi-mutated activation gate. Furthermore, at a temperature of 100 K where motional averaging on the NMR relevant timescale is strongly reduced, we could detect

residue-specific mobility of the selectivity filter in different functional states.

In **Chapter 7**, we introduce a novel method for DNP-enhanced ssNMR by the use of site-directed spin labeling. By creating local spin clusters via site-directed spin labeling applied to KcsA we show that this approach significantly enhances NMR sensitivity and causes signal modulation in a site specific way.

Chapter 2

Importance of lipid–pore loop interface for potassium channel structure and function

Elwin A. W. van der Cruijsen[*#], Deepak Nand[*#], Markus Weingarth[*], Alexander Prokofyev[*,†], Sönke Hornig[†], Abhishek A. Cukkemane[*], Alexandre M.J.J. Bonvin[*], Stefan Becker[§], Raymond E. Hulse[+], Eduardo Perozo[+], Olaf Pongs[†], Marc Baldus[*¶]

*Bijvoet Center for Biomolecular Research, Utrecht University
†Faculty of Medicine, Department of Physiology, Saarland University,
§ Max-Planck-Institute for Biophysical Chemistry, Department of NMR-Based Structural Biology
+Department of Biochemistry and Molecular Biology, Center for Integrative Science, University of Chicago
# contributed equally

Proceedings of the National Academy of Sciences of the U S A. 2013 Aug 6;110(32):13008-13

Abstract

Potassium (K^+) channels allow for the controlled and selective passage of potassium ions across the plasma membrane via a conserved pore domain. In voltage-gated K^+ channels, gating is the result of the coordinated action of two coupled gates: an activation gate at the intracellular entrance of the pore and an inactivation gate at the selectivity filter. By using solid-state NMR structural studies, in combination with electrophysiological experiments and molecular dynamics simulations, we show that the turret region connecting the outer transmembrane helix (transmembrane helix 1) and the pore helix behind the selectivity filter contributes to K^+ channel inactivation and exhibits a remarkable structural plasticity that correlates to K^+ channel inactivation. The transmembrane helix 1 unwinds when the K^+ channel enters the inactivated state and rewinds during the transition to the closed state. In addition to well-characterized changes at the K^+ ion coordination sites, this process is accompanied by conformational changes within the turret region and the pore helix. Further spectroscopic and computational results show that the same channel domain is critically involved in establishing functional contacts between pore domain and the cellular membrane. Taken together, our results suggest that the interaction between the K^+ channel turret region and the lipid bilayer exerts an important influence on the selective passage of potassium ions via the K^+ channel pore.

Introduction

Potassium (K^+) channels are embedded in the plasma membrane to control the selective passage of potassium ions across the lipid bilayer. The channels open and close their conduction pathway by sensing changes in physicochemical parameters such as pH, ligand concentration, and membrane voltage [2]. Structure–function studies on voltage-gated K^+ (Kv) channels suggested that lipid molecules are an integral part of the voltage-sensing domains, which transfer during the gating process electrical charges across the cell membrane [32,55,56]. In some of the available Kv channel crystal structures, lipid molecules appear most densely packed against the pore domain, presumably providing an appropriate environment for the stability and the operation of the gating machinery to open and close the conduction pathway. In general, the activity of Kv pore domains is thought to be determined by the activity of two gates in series, one for activation and one for

inactivation. These gates jointly control the conduction of ions through the pore[17,18,22,57–60]. The activation gate is located at the intracellular entrance of the pore and the inactivation gate is situated toward the extracellular entrance at the selectivity filter (i.e., C-type inactivation). In addition, some potassium channels possess close to the activation gate a receptor for an N-terminal inactivating domain (i.e., N-type inactivation).

The K^+ channel pore domain is conserved across all K^+ channels. It comprises a tetrameric assembly of two transmembrane helices (helices S5 and S6 in Kv channels) connected by a pore loop region consisting of a turret, the pore helix, and the selectivity filter. Although it is now evident that structural changes at the interface between K^+ channel protein and lipid play an important role during the gating process [18,27,33,61–63], including the coupling of voltage-sensor movements to Kv channel activation [64–67], detailed characterization of these structural changes and their implications for K^+ channel gating remain unresolved. In this study, we addressed the structural and functional role of the protein–lipid interface at the pore loop region of a K^+ channel by using a combination of solid-state NMR (ssNMR), electrophysiological recordings, and molecular dynamics (MD) simulations. Previously, we have studied pH-induced activation and inactivation gating as well as ligand binding to KcsA-Kv1.3, a KcsA-channel variant containing the turret region of the Kv1.3 channel [68,69]. Here, we established 3D structural views of the KcsA-Kv1.3 transmembrane helices and the pore loop region before and after channel inactivation. Unexpectedly, we observed significant structural alterations in the pore loop region involving unwinding/rewinding of a helical turn at the C-terminal end of transmembrane helix 1 (TM1; S5) near the protein–lipid interface. Additional ssNMR studies reveal that the structure of this region is largely conserved in the parent KcsA channel and that mutations at the inactivation gate directly affect the structure of the pore loop region as a whole. Combined with MD simulations, our studies suggest that the interface between lipid and K^+ channel pore loop region has an important influence on the stability of the pore structure and the conformational changes associated with K^+ channel gating.

Results

We conducted ssNMR-based structural studies on the chimeric KcsA-Kv1.3 channel[68] (abbreviated henceforth as “Chim”), a construct that exclusively differs in sequence vs. WT KcsA (henceforth “WT”) at amino acid residues 52 to 64 (Fig. 1). Subsequently, we compared our

results to functional data on Kv1.3 channel mutants and to spectroscopic results obtained on WT KcsA and KcsA mutants, which exhibit a constitutively open activation gate [21,70] (henceforth "WTom").

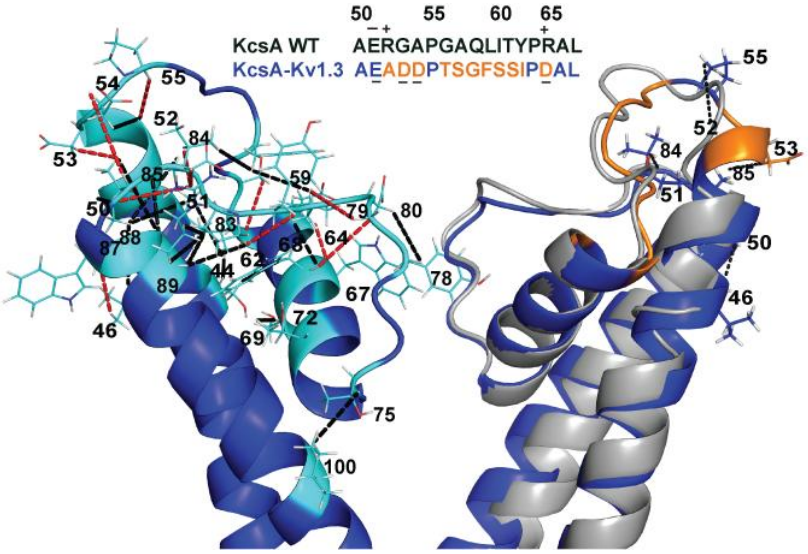

Figure 1. SsNMR analysis of membrane-embedded Chim in the closed conductive state. (*Left*) Cartoon representation of the 3D ssNMR model of the closed state (residues Chim 22–115). Resolved CHHC restraints (highlighted in cyan) identified from the CHHC spectrum (250 µs and 500 µs ^{1}H-^{1}H mixing) that are unambiguous based on the KcsA crystal structure and the available chemical shifts are indicated by black dashed lines. Additional correlations unique for the ssNMR structure of Chim are shown by red dashed lines. (*Right*) Superposition of the Chim structural model (blue) and the KcsA crystal structure (gray) with three resolved ssNMR restraints confirming the extended α-helical turn for the chimeric channel along with their amino acid sequence comparison highlighting (orange) the 11 mutations distinguishing the turret region.

Chim in the Closed Conductive State. We used an ssNMR-based hybrid strategy to establish 3D structural views of Chim before and after C-type inactivation. First, we constructed a homology model of the closed conductive state by using the crystal structure of KcsA [71] [Protein Data Bank (PDB) ID code 3EFF] and constructed a tetramer by using high ambiguity driven docking (HADDOCK) [72] (*Methods*). This model then served to predict and evaluate experimental CC and CHHC correlation experiments as the basis of 3D molecular structures (e.g., ref. [68]. Experimental spectra were recorded on fully ^{13}C,^{15}N-labeled and on fractionally deuterated Chim [73]. Resonance assignments were largely

taken from published work [69]. The monomeric structure of the closed pore domain (residues Chim 22–115), reconstituted in asolectin liposomes, was then calculated in Crystallography and NMR System (CNS) software [74]. Distance restraints were mostly derived by comparing the experimental CHHC spectra acquired with three different mixing times (50, 250, and 500 μs) along with the CC restraints obtained from fractional deuteration studies. Overall, approximately 70% of all expected correlations were visible in CHHC spectra (*Methods*). Additionally, torsion angle restraints obtained from earlier chemical-shift assignments[69] were supplemented during structure calculation in CNS. The final structure, compatible with all experimental data, was characterized by more than 2,000 restraints, including 339 long-range distances. Note that the pore loop region (residues Chim 44–90) was characterized by 156 long-range, 169 medium-range, and 148 sequential distance restraints.

The 3D structural backbone model of the closed channel state is depicted in Fig. 1 (*Left*), together with a selected set of CHHC distance restraints (Fig. 1, dashed lines). The overall channel architecture was in good agreement with the WT KcsA crystal structure [71]. In detail, however, we observed significant differences with respect to the TM1 (S5) pore-loop region. First, TM1 is extended until residue Chim Asp53 and thus contains an additional turn as diagnosed by secondary chemical shifts seen earlier [18] and CHHC restraints obtained here (Fig. 1, *Right*). Second, the turret structure connecting TM1 and pore helix significantly differs from the one of the WT KcsA X-ray structure (Fig. 1, *Right*). The structural changes in this TM1-helix and turret region (henceforth "TM1T region") along with intermolecular contacts detected in our study led to a widening of the pore (data not shown). This observation supports our previous data indicating that reduced steric hindrance in a widened Chim pore facilitates binding of the scorpion toxin Kaliotoxin (KTX) at the extracellular mouth of the channel [75].

C-Type Inactivation Involves Structural Changes in the Pore Loop. Next, we applied a similar ssNMR-based protocol to investigate structural details of open-inactivated state of the Chim channel in the lipid bilayer. Similar to WT KcsA [9], this state can be induced for the Chim channel by triggering inner gate bundle opening at low pH and reducing K^+ concentrations to less than 20 mM [17,18]. Notably, further

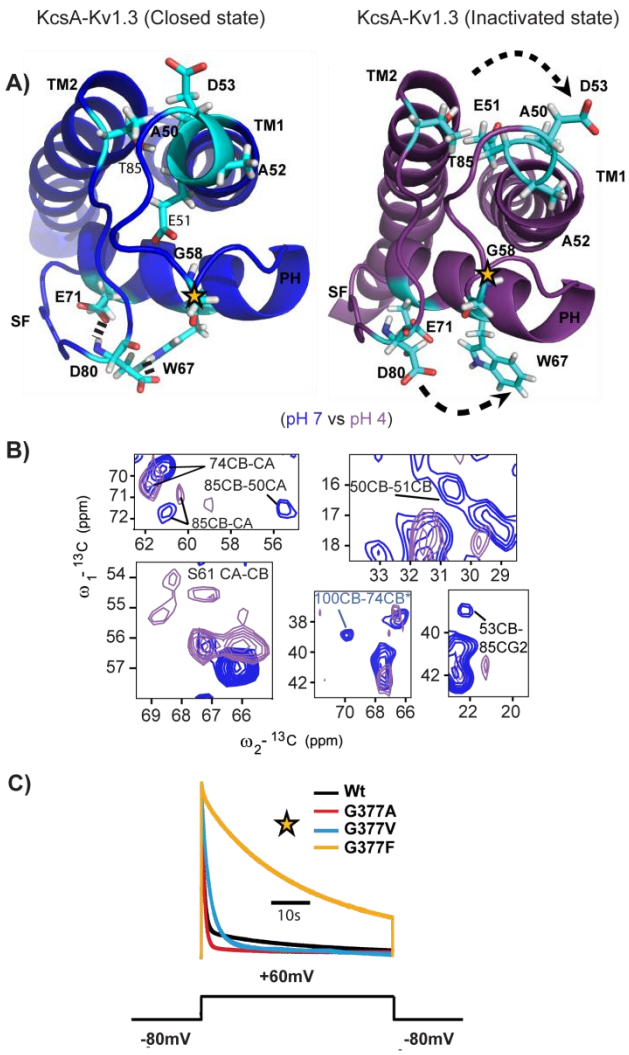

Figure 2. ssNMR-based experiments and functional studies of a selected set of K+ channels. (*A*) Conformational rearrangements observed for the closed (blue) and inactivated (purple) states of Chim embedded in asolectin lipid bilayer. (*B*) Spectral cutouts of (13C,13C) correlation spectra obtained for Chim at pH 7.0 (blue) and pH 4.0 (purple). Chemical-shift changes along with the structural restraints discerning the two channel states are shown. The absence of the intermolecular correlation of Chim 100IleCB to 74ThrCB at pH 4.0 is compatible with a reorientation of the TM2 helix. (*C*) Inactivation time courses of Kv1.3 and mutant Kv1.3 channels expressed in *Xenopus laevis* oocytes as indicated. Outward currents were elicited by the pulse protocol shown beneath the normalized current traces. Gly377 in the turret of Kv1.3 corresponds to Chim Gly58 marked by star in (*A*).

reduction to pH 3.7 did not change our Chim ssNMR spectra, even though macroscopic and single channel measurements suggest that the apparent activation pK_a is closer to pH 4.2 for WT KcsA [76]. For the analysis of the ssNMR data, an initial 3D structural model was constructed by using torsion angle restraints in channel regions known to undergo conformational changes after inactivation [17,18]. The resulting monomer fold was, in the second stage, evaluated by using long-range correlations detected in the CHHC data. The final structure revealed distinct structural rearrangements in several domains of the channel compared with the closed-conductive state (Fig. 2*A*). First, we confirmed earlier backbone chemical-shift changes in the selectivity filter residues [17,18]. In line with X-ray results on constitutively open truncated KcsA mutants [21,22], the selectivity filter in its inactivated state is reminiscent of that of a filter under low ionic conditions [PDB ID code IK4D [9]]. Second, the absence of the observed intermolecular correlation Ile100CB–Thr74CB observed in the closed conductive state (Fig. 2*B*) and the distinct chemical-shift changes in the transmembrane helix 2 (TM2)—together with earlier results using water-edited ssNMR spectroscopy [77]—suggest that the TM2 helix rotates during K^+ channel opening, as proposed from KcsA X-ray structural analyses [21]. Further analysis of our data suggests an opening of the activation gate by approximately 23 Å, as defined by the Cα–Cα intersubunit distance at positions WT/Chim Thr112 [21], and close to the physiologically relevant opening in the full-length channel [78].

Finally, we found that several medium- and long-range correlations observed for the turret region in the closed conductive state vanished after inactivation, e.g., the one comprising Chim Asp53 to Chim Thr85 (Fig. 2*B*), whereas new correlations appeared, e.g., the one comprising Chim Thr56 to Chim Pro83. In the structural ensemble, these alterations in distance and dihedral angle restraints are characteristic of a destabilization and outward rotation of the extended TM1 helix accompanied by a loss of the multipoint hydrogen-bond network of Chim Glu71, Chim Asp80, and Chim Trp67 (Fig. 2*A*). Although a distinct set of residues in the turret and the pore helix were absent in our multidimensional correlation spectra (Chim Ala50, Glu51, Asp64, and Tyr82), the results clearly indicate that conformational changes in the turret region accompany Chim inactivation. Importantly, back-titration to pH 7 fully restores the closed conductive state.

Previously, we have shown that Chim Gly58 in the turret region is a key residue for C-type inactivation-sensitive binding of KTX [68,75]. The conformational changes we observed between the closed and the open-inactivated state suggested that bulky residues at position 58 not only interfere with KTX binding, but also with C-type inactivation. As the Kv1.3 channel exhibits a pronounced C-type inactivation, we tested the effect of bulky side chains at position G377 (equivalent to Chim Gly58) on C-type inactivation in the Kv1.3 channel. We mutated Kv1.3 residue Gly377 to alanine, valine, and phenylalanine, respectively (Fig. 2*C*) and recorded macroscopic currents in *Xenopus* oocytes with a two-electrode voltage clamp. Although current–voltage relations, time rise to peak, and deactivation kinetics of WT and mutant Kv1.3 channels showed no significant differences (Table S2), mutating Kv1.3 G377V and especially Kv1.3 G377F markedly slowed the time course (τ_{inact}) of Kv1.3 C-type inactivation [Kv1.3, τ_{inact} = 0.66 ± 0.02 s (SEM); Kv1.3 G377A, τ_{inact} = 0.82 ± 0.01 s; Kv1.3 G377V, τ_{inact} = 3.61 ± 0.20 s; Kv1.3 G377F, τ_{inact} = 28.6 ± 0.8 s; n = 3–5; Fig. 2*C*). Combining the structural and functional data suggests that bulky side chains at turret residue Chim Gly58 affect the closure of the inactivation gate at the selectivity filter.

*Pore Loop Structure Is Defined by a Combination of Protein–Lipid and Protein–Protein Interactions.*The sequences of WT and Chim differ only by 11 aa in the turret region (Fig. 1). Structural changes observed between Chim in lipid bilayers and the crystal structure of WT KcsA could therefore be induced by changes in protein sequence and/or the presence of the lipid bilayer. To examine the influence of protein sequence, we investigated the structure of WT KcsA by ssNMR in lipid bilayers. Similar to the chimeric channel, we conducted a series of multidimensional ssNMR experiments to obtain resonance assignments and structural restraints for the WT pore loop region. We could readily assign turret residues specific for WT and generate a 3D model of WT in lipid bilayers by using a series of CHHC experiments. The resulting structure is shown in Fig. 3*A* in red, with specific medium to long-range restraints annotated in cyan and dotted lines. We compared our results vs. the 3D structure of Chim (Fig. 3*A*, *Right*, blue) and the X-ray structure of WT (Fig. 3*A*, *Right*, gray). Structures of the selectivity filter and TM1/TM2 helices are in good agreement. In contrast, we observed significant structural differences in the turret region, including an elongation of the TM1 helix for bilayer embedded WT and Chim channels. Notably, our ssNMR results are in

good agreement with earlier electron paramagnetic resonance (EPR) work on WT KcsA in asolectin liposomes [76]. The EPR data indicated that TM1 helix extends until WT Arg52.

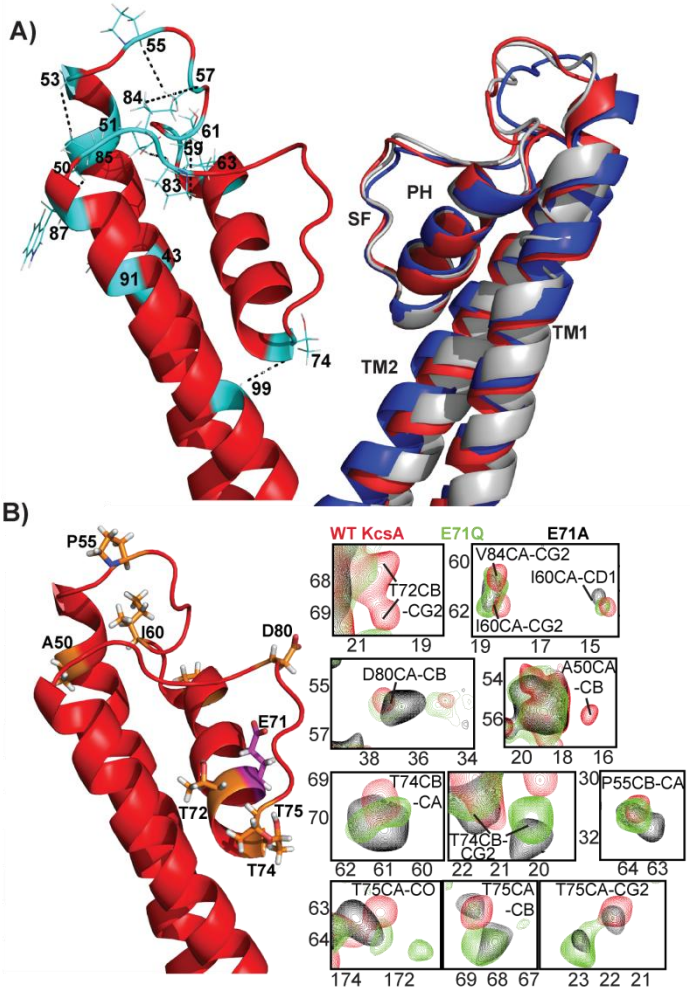

Figure 3. (*A*) ssNMR-based structural model of membrane-embedded KcsA (WT) in the closed conductive state. (*Left*) Cartoon representation of the 3D ssNMR model of the closed state of KcsA (residues WT 22–115). Resolved CHHC restraints (highlighted in cyan) identified from the CHHC spectrum (250 µs 1H-1H mixing) that are unambiguous based on the ssNMR assignments. (*Right*) Superposition of the KcsA structural model (red), KcsA-Kv.1.3 (blue), and KcsA crystal structure (gray). (*B*) WTom Glu71 mutants change the conformation of the pore-loop of KcsA. (*Left*) Cartoon representation of KcsA with the mutation site E71 (purple), with residues exhibiting ssNMR shifts (blue) or peak doubling in the two mutants. (*Right*)

(13C,13C) Correlation spectra obtained for WT (red), WTom E71Q, and WTom E71A (green and black, respectively), at pH 7.4, 50 mM [K+] reconstituted in asolectin.

Previous work has shown that mutations in the pore loop region can have a profound influence on inactivation gating of K^+ channels [12,24,62,79]. We investigated the influence of mutations at the pore-helix position Glu71 on the pore loop structure by comparing ssNMR data on WT KcsA (Fig. 3*B*, red) to spectra obtained on E71Q (Fig. 3*B*, green) and E71A (Fig. 3*B*, black) mutants. As expected [24], we observed chemical-shift variations at residue WTom Asp80 that is part of a multipoint hydrogen-bond network including Glu71 in WT [12] for WTom E71Q and E71A. Interestingly, we also observed a disappearance of the extended α-helix (as diagnosed by WTom Ala50) for both gating mode mutants. Additional turret residues including WTom Ile60 and WTom Pro55 exhibited chemical shift changes and peak doubling, respectively (indicated in orange on the 3D structure in Fig. 3*B*). These spectral variations extended to the pore helix (WTom Thr72) and residues in the selectivity filter (WTom Thr74/Thr75). Cross peaks for selectivity filter residues differed by approximately 2 ppm compared with correlations seen for WT KcsA in the conductive state (Fig. 3*B*, red). These observations would be compatible with increased molecular mobility around WTom Thr74/WTom Thr75. Indeed, previous MD simulations showed a considerable increase in the frequency and lifetime of WT Val76 reorientation in the WT E71Q mutant correlated with short-lived flicker states in WT E71Q single-channel recordings [24]. Taken together, our results on KcsA are consistent with the view that the pore loop region functions as a functional unit that includes the extended TM1 helix coupled via the turret to the inactivation gate and extending all the way to the pore–TM2 interface. This view is in remarkable agreement with previous mutational studies in Shaker Kv channels [62].

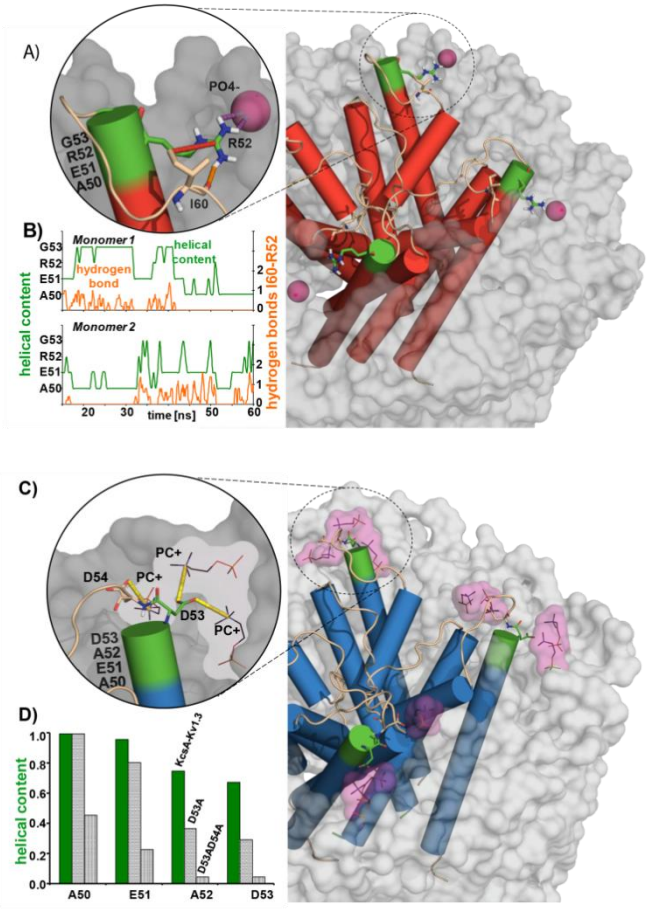

Figure 4. (*A*) Structural snapshot of WT illustrating the intramolecular hydrogen bond between the WT Arg52 amidine group and WT Ile60CO (orange lines) and intermolecular protein–lipid interactions (magenta lines) that stabilize the helical elongation of the TM1 helix until residue WT Gly53. (*B*) Correlation of the helical propensity of residues WT Ala50 to WT Gly53 (green) and the presence of hydrogen between the WT Arg52 amidine group and WT Ile60CO (orange) evaluated for two monomers of KcsA during a 60-ns MD trajectory. (*C*) Structural snapshot of Chim illustrating the intermolecular protein–lipid electrostatic interactions between negatively charged Chim Asp53 and Chim Asp54 side chains and positively charged phosphatidylcholine headgroups (yellow lines) that stabilize the helical elongation of the TM1 helix until residue Chim Asp53. (*D*) Evaluation of the helical propensity of residues Chim Ala50 to Asp53 (green columns) and the mutants Chim D53A (dashed columns) and Chim D53A/D54A (pointed columns), averaged for monomers and 25 ns of MD trajectories.

To study the molecular details that determine the influence of lipids on the pore loop structure, we resorted to MD simulations for WT and Chim (Fig. 4) embedded in lipid bilayers. In the case of WT (Fig. 4*A*), we observed the formation of an intermolecular hydrogen bond between the WT Arg52 amidine group and WT I60CO (Fig. 4, orange lines) as well as intermolecular protein–lipid interactions (Fig. 4, magenta lines) that we suggest stabilize the helical elongation of the TM1 helix up to residue WT Gly53. The spatial proximity of the WT Arg52 amidine group to WT Ile60 was verified (Fig. 4, red lines) by a tailored ssNMR rotational resonance experiment [80]. During the MD trajectory (Fig. 4*B*), we observed a remarkable correlation between helical propensity of residues WT Ala50 to WT Gly53 (Fig. 4, green) and the presence of hydrogen bonding between the WT Arg52 amidine group and WT Ile60CO (Fig. 4, orange). This view was supported by ssNMR data on the WTom E71A/Q mutants lacking the TM1T helix and exhibiting chemical-shift changes at WTom Ile60 (Fig. 3*B*). In the case of Chim, in which residues 53 and 54 are mutated (Fig. 1 and 4 *C* and *D*), we again observed intermolecular protein–lipid electrostatic interactions, namely between negatively charged Chim Asp53 and Chim Asp54 side chains and positively charged phosphatidyl-choline headgroups (Fig. 4, yellow lines) that stabilize the helical elongation of the TM1 helix up to residue Chim Asp53. Neutralizing Asp-53 and 54 (D53A, D53AD54A; Fig. 4*D*) strongly reduced α-helical propensity of residues 50 to 53, compared with Chim (Fig. 4*D*, green columns).

Discussion

We have used an ssNMR-based strategy to study the 3D structure of a lipid bilayer embedded K^+ channel in its resting as well as its pH-induced inactivated states. Our major finding is an unexpected structural plasticity at the C-terminal end of the TM1-helix and the adjacent turret region, which is sensitive to lipidic environment, protein sequence, and the functional state of the K^+ channel (Fig. 5). We find that the TM1 helix unwinds when the K^+ channel enters the inactivated state and rewinds during the process of repriming into the resting state. This helical unwinding/rewinding is associated with conformational changes within the turret region and the pore helix connecting TM1 and TM2. Our results on KcsA gating mode mutants suggest an intrinsic coupling between the TM1-turret (TM1T) region and the hydrogen-bonding network in the back of the selectivity filter. The network involved in stabilizing the selectivity filter plays an important role in K^+ channel selectivity and inactivation gating. In comparison with crystal structural

data [71], our ssNMR-based structural models of the Chim chimera and WT KcsA in their resting state show an extended TM1 helix toward its C-terminal end. These data are in good agreement with results of earlier EPR work suggesting an elongated TM1 helix for WT KcsA in liposomes [14].

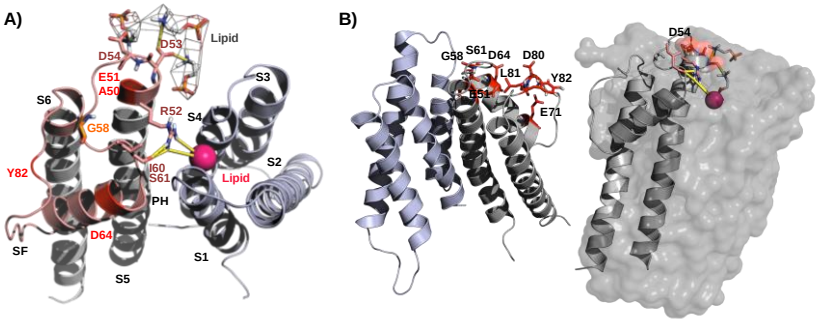

Figure 5. Role of interfacial and turret residues in K+ channel gating and channel stabilization. (*A*) Superposition of the inactivated state of Chim channel (gray) and the X-ray structure of the cyclic nucleotide-regulated K^+ channel MlotiK1 [light blue[81]; PDB ID code 3BEH] obtained by aligning the S5–S6 subunits. Residues highlighted in red (Chim-Ala50, Glu51, Asp64, and Tyr82) exhibit strong signal attenuation of signals after inactivation whereas residues indicated in dark red undergo structural rearrangements after inactivation as shown in Fig 2A. Mutation of Gly377 equivalent to Chim Gly58 (orange) strongly affects the details of C-type inactivation in Kv1.3. Residues WT Ile60, WT Ser61, and WT Asp80 undergo chemical shift changes in KcsA gating mutants. According to MD simulations, TM1T residues 52 (WT) and 53 (Chim) are critically involved in protein–protein (KcsA) as well as protein–lipid (WT and Chim) interactions that stabilize the pore loop structure. (*B*) Side views shown for the case of the MlotiK1 (*Left*) and the Chim case (*Right*) with color coding as in *A*. For the sake of clarity, only a subset of residues is depicted in *B*.

The TM1T conformational change involves the highly conserved amino acid residue E51 (Fig. 5A), which plays an important role for C-type inactivation in K+ channels. In Shaker Kv channels, mutation of E418 (equivalent to KcsA E51) to alanine boosts C-type inactivation [24]. Moreover, contacts between E418 and the turret–TM2 connector region can stabilize [62] the inactivated (E418–V451, equivalent to KcsA E51–V84) or the open state (E418–G452, KcsA E51–T85). In line with the work of Larsson and Elinder [62], we observed structural changes in Chim leading to an outward rotation of TM1T and a concomitant distance increase between E51 and T85 (Fig. 2). In the KcsA channel family,

E51, together with Chim S61 and Chim D64, represent peripheral protein residues, and may act as a point of interaction with the surrounding lipid bilayer. Indeed, our MD studies suggest that these pore loop residues are critically involved in stabilizing the lipid–protein interface (Fig. 5*B*, *Right*). In Kv channels, E51 fulfils a closely related role as part of a conserved residue network that extends into the S1 helix of the voltage sensor [66]. In particular, the S1 T248 residue (Shaker numbering) is found in close proximity to S5 residue Y415 (Chim V48; Fig. 5) and S428 (Chim S61) in the Kv1.2-paddle crystal structure, which presumably corresponds to the open conformation.

Chim G58 (F425 in Shaker), on the contrary, is an important residue in the turret region for K+ channel gating. When comparing the Chim structure before and after activation, substantial conformational changes have occurred around the aromatic cuff that structurally links turret residues Chim G58 and Chim F59 and amino acids around Chim D80 critical for inactivation (Fig. 5*B*, *Left*). Mutating F425 to lysine induces an electrostatic domino effect in the Shaker channel turret, ultimately affecting voltage-dependent gating [27,82]. Here, we show that mutating the equivalent residue G377 to valine and phenylalanine in the turret of the Kv1.3 channel markedly attenuates Kv1.3 C-type inactivation. It is worth noting that mutational studies on the HERG (human ether-a-go-go related gene) channel also demonstrated a functional importance of the turret region for C-type inactivation [63].

In summary, our data highlight the structural plasticity of the TM1T region at the extracellular side of the K+ channel. In turn, this plasticity likely allows the TM1T region to engage in significant and reversible conformational changes during K+ channel gating. Combination of our spectroscopic and MD data helped elucidate the atomic details that dictate the conformation of TM1T in a lipid environment. These studies underline the strong influence of lipids on KcsA channel gating [27,83] and, at the same time, reveal a remarkable flexibility in maintaining lipid–protein and protein–protein contacts across different pore loop sequences. Biochemical work suggested that, during channel folding and assembly, P-loop architecture is already formed in the monomer state [84]. Lipids are likely playing a fundamental role in establishing a defined structure for the monomer. In addition, lipids may also act as a cofactor in conformational changes associated with channel gating transitions [29,83]. In this process, the TM1T region could represent the cornerstone of a trajectory that leads to well defined structural

alterations in pore helix, selectivity filter, and activation gate during channel activation and inactivation.

Metods

Materials and Sample Preparation. Expression, purification, and reconstitution into liposomes was done as described previously [68,70]. Reconstitution was performed at a 100/1 lipid/channel molar ratio. pH titrations were performed by thoroughly washing the proteoliposome pellet with the desired phosphate or citrate buffers, followed by 30 min ultracentrifugation at 125000 × *g* and +4 °C [17].

ssNMR. ssNMR experiments were conducted by using 3.2-mm or 4-mm triple-resonance (^{1}H,^{13}C,^{15}N) magic-angle-spinning (MAS) probe heads at static magnetic fields of 14.1, 16.5 and 18.8 T corresponding to proton resonance frequencies between 600 and 800 MHz (BrukerBiospin). CHHC (e.g., ref. [68]) experiments were recorded at an effective sample temperature of 243 K. The CC correlation experiments were performed with an effective sample temperature varying between 273 K and 280 K. MAS frequencies used were 9.375 kHz (at 600 MHz and 700 MHz) and 12 kHz (800 MHz) for CHHC spectra and 10.92 kHz (700 MHz) for (^{13}C,^{13}C) proton-driven spin diffusion (PDSD) and phase-alternated recoupling irradiation scheme spin diffusion experiments performed under weak coupling conditions [85]. A ^{1}H field strength of 83.3 kHz was used for 90° pulses and small phase incremental alternation 64[86] decoupling during evolution and acquisition. CHHC experiments were acquired with ^{1}H-^{1}H mixing times of 50, 250, and 500 µs by using an initial cross-polarization (CP) step of 700 µs and CP steps of 80 µs enclosing the proton mixing step to select for one bond (C-H) magnetization transfer. Mixing times of 20 ms or 30 ms were used to obtain intraresidue (^{13}C,^{13}C) correlations in PDSD experiments.

MD. MD simulations were carried out using the Groningen Machine for Chemical Simulations (GROMACS) simulations package, version 4.5.3[81], with the Groningen Molecular Simulation computer program package (GROMOS53a6) force field [87]. The simulation systems were represented by the atomic models of Chim and WT KcsA, embedded in a bilayer in an aqueous solution of KCl. Potassium and chloride ions were added to electrostatically neutralize the systems and to mimic 80 mM KCl solutions. The KcsA starting structure was derived from

crystal structure 3EFF (PDB) [71] to probe spontaneous helical elongation of TM1, the Chim starting structure from our ssNMR-based structure model. Mutations in the Chim model were introduced with Pymol (Delano Scientific). All systems were simulation at constant-pressure for at least 25 ns.

Electrophysiology. The expression of Kv1.3, WT and mutant channels in the *Xenopus* oocyte expression system was as described previously [76]. Activation, deactivation time courses, and voltage-conductance relations were measured with test pulses of 100 ms starting from a holding potential of −100 mV. For measurement of Kv1.3 inactivation, we used long test-pulse durations of 60 s at test potentials of +60 mV, where Kv1.3 channels are completely activated. Inactivation time courses and recovery from inactivation were evaluated by using HEKA-PULSEFIT in combination with KaleidaGraph software. Statistical significance was tested by Student *t* test.

Structural analysis and validation. A homology model of KcsA-Kv1.3 in the close conductive state was generated from the tetramer structure of full-length KcsA [71](PDB ID 3EFF) and used to predict CC and CHHC ssNMR spectra. Chemical shift assignments were largely used from previous work[69]. Missing assignments were supplemented by SPARTA backbone predictions and average side chain carbon chemical shifts taken from the BMRB data bank. The structural analysis involved CHHC spectra recorded using mixing time of 50 µs, 250 µs and 500 µs in the closed state and 50 µs and 250 µs in the inactivated state. Data were analyzed with a ^{1}H-^{1}H distance cutoff of 6 Å and a predicted correlation was verified if the signal to noise exceeded a value of 3 in the respective experimental spectrum. Peaks located close to the diagonal of the spectrum or to spinning side bands were manually removed.

Monomer structures for KcsA-Kv1.3 were computed by simulated annealing in CNS [74] starting from an extended conformer (residues 22-160). Homology derived ssNMR ^{1}H-^{1}H distance restraints from CHHC spectra along with the unambiguous resolved long and medium range contacts identified from [^{2}H,^{13}C,^{15}N] KcsA-Kv1.3 and dihedral angle restraints obtained from PREDITOR[88] using experimental chemical shifts and values estimated from the KcsA structural homologue (PDB ID 3EFF) were represented by soft-square-well potentials. Dihedral angles for residues 50-65 containing the 11 mutations distinguishing KcsA and KcsA-Kv1.3 were exclusively based on experimental

chemical shifts. The simulated annealing procedure followed the standard CNS protocol except for an increased number of steps performed during the high temperature (2000), first slow-cooling (6000), and second slow-cooling (5000) annealing stages. We generated 400 structures and selected 20 based on lowest overall energy for further analysis. We observed convergence to a unique structure for the pore domain of KcsAKv1.3 (residues 22–115). Structures of the C-terminal residues 116 to 160 diverged, possibly as a result of an insufficient number of assignments and structural constraints. In addition, residues 1 to 20 were used for assignment (ref. [69]) and cross validation. The final structural models exhibited backbone RMSDs (for residues 44–90 and given in Angstrom) of 0.3 (KcsA-Kv1.3: closed state), 1.0 (KcsA-Kv1.3: inactivated state) and 0.33 (KcsA: closed state).

The ssNMR structural models were validated by back predicting CHHC spectra with ^{1}H-^{1}H distances determined with the lowest energy structure for the closed as well as the inactivated state of KcsA-Kv1.3. Firstly, we confirmed that predicted spectra reproduced experimental cross peak positions. In the second stage, we further analyzed those correlations that were based on unambiguous experimental assignments for KcsA-Kv1.3. Within this subset, we identified 15 additional (medium and long-range) CHHC correlations for the closed state and 4 additional ones for the inactivation state that are unique and unambiguous for the 3D ssNMR models of KcsA-Kv1.3. Likewise, the final structure significantly improved chemical shift predictions using SPARTA [89] for the turret region compared to the starting structure.

The structural model of WT KcsA was obtained using a similar strategy. Firstly, the full-length KcsA [71] (PDB ID 3EFF) structure was used to predict CC and CHHC ssNMR spectra. Resonance assignments for residues that differ from KcsA-Kv1.3 were obtained de-novo. The structural analysis involved CHHC spectra recorded using mixing time of 250 μs and 500 μs (data not shown). Data were analyzed with a ^{1}H-^{1}H distance cutoff of 6 Å and a predicted correlation was verified if the signal to noise exceeded a value of 3 in the respective experimental spectrum. Peaks located close to the diagonal of the spectrum or to spinning side bands were manually removed. The determination of the monomer structure then proceeded as given above using dihedral angle restraints that were updated by the resonance assignments of the mutation site in KcsA (data not shown) vs. KcsA-Kv1.3. The simulated annealing procedure followed the standard CNS protocol except for an increased number of steps performed during the high temperature (1000), first slow-cooling (2000), and second slow-cooling (5000) annealing stages.

*Tetramer generation using Multibody docking.*The KcsA-Kv1.3 tetramer model was calculated using the multi-body docking routine of the HADDOCK web server [72]. Firstly, four identical copies (M1-M4) of the lowest energy monomeric structure for the closed state of KcsA-Kv1.3 (residues 22-115) were obtained using simulated annealing molecular dynamics refinement in CNS. These structures were supplied, along with 23 intermonomer contacts identified from the fractional deuteration studies, as input during the docking run. The C4 symmetry of the tetramer was defined by imposing six C2 symmetry pairs between the monomers M1-M2, M2-M3, M3-M4, M4-M1, M1-M3 and M2-M4. Standard settings were used in the HADDOCK-simulated annealing protocol. All models obtained from the simulated annealing refinement subsequently followed the explicit solvent refinement in DMSO as a mimic for a membrane environment. The final structures were ranked on the basis of total energy.

Chapter 3

Structural Determinants of Specific Lipid Binding to Potassium Channels

Markus Weingarth,[†] Alexander Prokofyev,[‡] Elwin A. W. van der Cruijsen,[†] Deepak Nand,[†] Alexandre M. J. J. Bonvin,[†] Olaf Pongs,[‡] and Marc Baldus[†]

†Bijvoet Center for Biomolecular Research, Faculty of Science, Utrecht University, Padualaan 8, 3584 CH Utrecht, The Netherlands
‡Saarland University, Faculty of Medicine, Department of Physiology, Building 59, 66421 Homburg, Germany

Journal of the American chemical society 2013 Feb 135(10):3983–88

Abstract

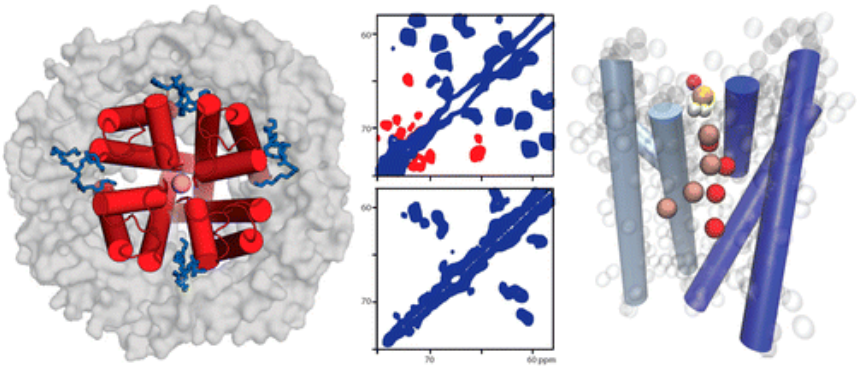

We have investigated specific lipid binding to the pore domain of potassium channels KcsA and chimeric KcsA-Kv1.3 on the structural and functional level using extensive coarse-grained and atomistic molecular dynamics simulations, solid-state NMR, and single channel measurements. We show that, while KcsA activity is critically modulated by the specific and cooperative binding of anionic nonannular lipids close to the channel's selectivity filter, the influence of nonannular lipid binding on KcsA-Kv1.3 is much reduced. The diminished impact of specific lipid binding on KcsA-Kv1.3 results from a point-mutation at the corresponding nonannular lipid binding site leading to a salt-bridge between adjacent KcsA-Kv1.3 subunits, which is conserved in many voltage-gated potassium channels and prevents strong nonannular lipid binding to the pore domain. Our findings elucidate how protein–lipid and protein–protein interactions modulate K^+ channel activity. The combination of MD, NMR, and functional studies as shown here may help to dissect the structural and dynamical processes that are critical for the functioning of larger membrane proteins, including Kv channels in a membrane setting.

Introduction

Structure and function of many membrane proteins are crucially modulated by direct interaction with lipid residues.[26,90–97] These lipids are typically categorized as annular, constituting a shell around the protein and showing relatively weak binding affinity, or as nonannular. The latter are specific lipid residues that bind with high affinity to hydrophobic clefts of membrane proteins, often copurify alongside the protein, and are resolved in crystal

structures. For example, MacKinnon et al. revealed the presence of a diacylglycerol fragment in the crystal structure of the homotetrameric potassium channel KcsA from Streptomyces lividans that requires negatively charged lipids for activity.[33] The location of the lipid fragment in a shallow groove between adjacent channel subunits in proximity to the two positively charged arginine residues R64 and R89 would thus be compatible with a prominent influence of nonannular anionic lipid binding on channel activity.[33] Much research has since been invested to elucidate the nature and affinity of the lipid residues involved in nonannular lipid binding,[27,98,99] although how and if specific lipid residues modulate the activity of the KcsA channel remain elusive.

				64									89			
KcsA	T	Y	P	R	A	L	W	L	W	G	R	L	V	A
KvAP	S	V	F	D	A	L	W	P	I	G	K	V	I	G
hKv1.1	S	I	P	D	A	F	W	I	G	G	K	I	V	G
hKv1.2	S	I	P	D	A	F	W	V	W	G	K	I	V	G
hKv1.3	S	I	P	D	A	F	W	I	G	G	K	I	V	G
hKv1.4	S	I	P	D	A	F	W	V	G	G	K	I	V	A
hKv1.5	S	I	P	D	A	F	W	L	W	G	K	L	V	A
hKv1.6	S	I	P	D	A	F	W	V	G	G	K	I	V	G
hKv1.7	S	I	P	E	S	F	W	V	G	G	K	I	V	G
hKv7.1	S	I	P	D	A	L	W	W	W	G	K	T	I	A
hKv7.2	T	Y	A	D	A	L	W	W	N	G	R	L	L	A
hKv7.3	T	Y	A	D	A	L	W	W	E	G	R	L	I	A
hKv7.4	S	Y	A	D	S	L	W	W	L	G	R	V	L	A
hKv7.5	T	Y	A	D	A	L	W	W	L	G	R	L	V	A

Figure 1. Sequence alignment of KcsA and a series of Kv channels. The positively charged residue pair R64 and R89 of KcsA's extracellular nonannular site is highlighted. It is shown that R64 is replaced by a negatively charged residue in many Kv channels.

KcsA with its inner helix bundle serves as an archetypical pore domain of voltage-gated (Kv) potassium channels, which thus potentially share KcsA's extracellular nonannular site.[100] Interestingly, the positively charged residue R64 in KcsA is replaced by a negatively charged

residue at the equivalent position in many Kv channels, particularly in human Kv1.x (KNCA) and Kv7.x (KCNQ) (Figure 1), although this charge inversion is not conserved throughout the whole KCNx family.

A better understanding of nonannular lipid binding to the pore domain is of general importance to Kv channels. Indeed, specific binding of spingomyelin involving the pore domain was shown to have a prominent influence on Kv channel voltage dependence and gating. [101] Here we have compared the influence of specific lipid binding in KcsA to the chimeric KcsA-Kv1.3, which contains 11 residues of the human Kv1.3 in the turret region,[68,69] including mutation R64D (Figures 1). In a combined approach of extensive coarse-grained molecular dynamics (CGMD)[102,103] simulations on the submillisecond time scale, solid-state NMR (ssNMR), and electrophysiological measurements, we show that nonannular anionic lipid binding in proximity of the selectivity filter correlates with the lipid sensitivity of KcsA activity. In KcsA-Kv1.3, the presence of a salt-bridge at the corresponding nonannular lipid binding site of Kv channels decreases residence times of bound lipids by about 1 order of magnitude. Based on these insights and supported by atomistic MD simulations, we formulate a molecular mechanism how negatively charged lipids could modulate KcsA's activity and discuss the role of a salt-bridge between S5 and S6 helices on Kv channel activity in general.

Results and Discussion

Structural Studies: MD. Several studies, especially by fluorescence spectroscopy[98] and electrophysiological measurements,[99] have confirmed a general preference of anionic over zwitterionic lipids for the extracellular nonannular site of KcsA. Yet, so far, atomic insights have been exclusively brought about by atomistic MD simulations over a length of 20–30 ns,[104] excluding the possibility to monitor lipid binding on the micro- to millisecond time scale. We sought to bridge the time scale gap between experimental and in silico studies by resorting to large-scale CGMD simulations over a total effective simulation time of 0.63 ms (2 × 0.21 ms for KcsA, 0.21 ms for KcsA-Kv1.3), which allowed us to determine quantitative relative affinities for zwitterionic and anionic lipids. Simulations were carried out in mixed DPPC:DPPG bilayers (3:1 molar ratio) (Figure 2a), which roughly correspond to the molar ratio of zwitterionic to anionic lipids in the inner membrane of E. coli,[105] in which both channels were expressed for the experimental part of this study. The CGMD simulations revealed considerable differences

in nonannular lipid binding between KcsA and KcsA-Kv1.3. We observed for both channels nonannular lipid binding to the intersubunit binding site on the microsecond time scale, however, the lifetime of

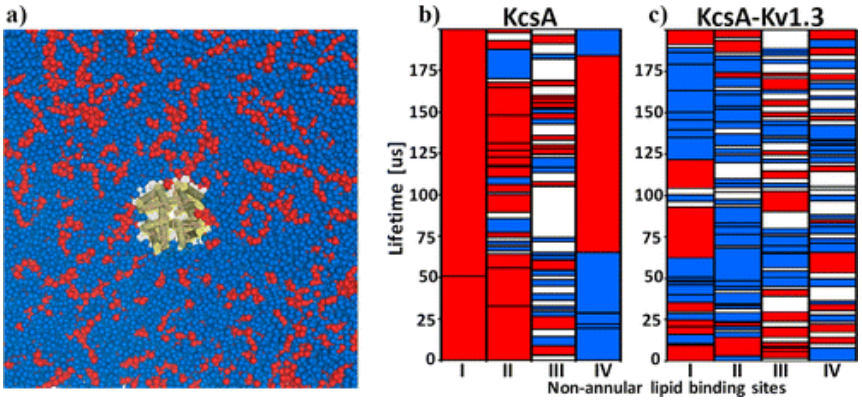

Figure 2. (a) The system used for the CGMD simulations: KcsA/KcsA-Kv1.3 channels were inserted in a large (25 × 25 nm^2) mixed DPPC:DPPG bilayer (3:1 molar ratio). DPPC lipids are highlighted in blue and DPPG lipids in red. The atomic-resolution channel structure is superimposed on its CG representation. (b,c) Evaluation of the lifetimes of bound DPPC (blue) and DPPG (red) for each nonannular site of (b) KcsA and (c) KcsA-Kv1.3 over trajectories of 210 μs. Each blue or red box in the four columns represents a single binding event. The first 10 μs were considered as equilibration period. Periods in which the lifetimes did not exceed 2 μs are indicated in white. During these white periods, the binding sites were usually occupied by DPPC or DPPG in fast exchange and rarely empty. The nonannular sites are plotted in a clockwise order, i.e., grooves I and II are opposite to grooves III and IV, respectively. The numbering of the binding sites is arbitrary.

nonannular DPPG was about 1 order of magnitude longer for KcsA (Figure 2b,c). For KcsA, averaged over a total simulation time of 420 μs, we found lifetimes (without counting for site III) for DPPG and DPPC of 31.8 and 11.6 μs, respectively, while we observed lifetimes for DPPG and DPPC of 5.9 and 4.9 μs, respectively, in KcsA-Kv1.3. A summation over all lifetimes gave rise to an absolute and relative (relative means assuming a 1:1 DPPC:DPPG molar ratio) DPPG occupancy of the nonannular sites of 64 and 84% in KcsA, respectively, which agrees well with fluorescence measurements.[98,106] In KcsA-Kv1.3, however, the preference for anionic lipids is much lower with 37 and 64% absolute and relative DPPG occupancy, respectively. Preliminary GCMD simulations with the KcsA channel embedded in a

3:1 DOPC:DOPG mixture point to an analogous strong preference of anionic over zwitterionic nonannular lipid binding.

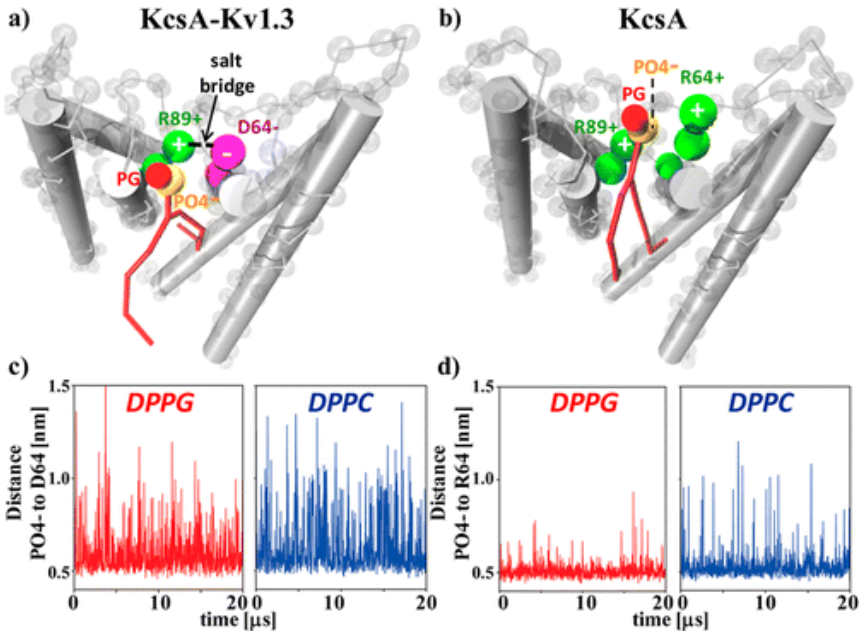

Figure 3. Schematic representation of nonannular lipid binding to (a) KcsA-Kv1.3 and (b) KcsA. Backbone beads are highlighted as gray spheres. (c,d) Trajectories of the distance of the phosphate-groups of bound DPPG (red) and DPPC (blue) to (c) D64 of KcsA-Kv1.3 and (d) R64 of KcsA. The minimum distance of two CG beads is 0.5 nm. In KcsA-Kv1.3, narrowing of the nonannular site by salt-bridge D64–R89 and electrostatic repulsion between D64 and lipid-phosphate groups prevents headgroup anchoring, whereas phosphate groups are ideally sandwiched by R64 and R89 in KcsA.

Interestingly, the CGMD simulations point to cooperativity in the nonannular lipid binding to KcsA. Lipids bound strongly to two sites (sites I and IV in Figure 2b) with lifetimes of more than 100 μs, with moderate affinity to one site (site II) and with little affinity to another binding site (site III). This behavior could be reproduced in a second KcsA simulation and matches well with fluorescence and single channel conductance measurements,[27] which found cooperative behavior in the effect of anionic lipids on channel open probability. This led to a model in which the occupation of three of the four nonannular sites by anionic lipids sufficed for channel activity. [27] Remarkably, MacKinnon and coworkers measured a ratio of 0.7 molecules of copurified lipid per

KcsA monomer,[33] which would also be consistent with strong to moderate binding to only three sites, [33] as the simulations suggest. The cooperative lipid binding, which we observe in the CG simulations seems to be modulated by the bulky side chains of P63 and L86 of adjacent subunits, which may prevent lipid headgroups to approach R64 and R89. Remarkably, the onset of this scenario is also visible in atomistic simulations, which show the narrowing of one nonannular binding pocket by the "lock" P63–L86, which impedes headgroup anchoring and binding of the sn1 lipid chain to the groove between the subunits, while the other three nonannular sites remain accessible.

An analysis of the trajectories revealed the formation of a tight salt-bridge D64–R89 between all adjacent subunits of KcsA-Kv1.3 (Figure 3a), which has a major influence on specific lipid binding. On the one hand, the salt-bridge narrows the nonannular site, and on the other hand, D64 repulses phosphate groups of any bound lipid (Figure 3a,c). This scenario impedes lipid headgroup anchoring on top of KcsA-Kv1.3, irrespectively of the type of headgroup, and generally leads to reduced nonannular lipid lifetimes in comparison to KcsA (Figure 3b). In KcsA the positively charged R64 and R89 can ideally sandwich negatively charged lipid-phosphate groups (Figure 3b,d). This shielding of the two arginine residues by the presence of lipid-phosphate groups in fact stabilizes the KcsA structure. The predominant influence of the charge of residue 64 on nonannular lipid residence times was verified by a CGMD simulation of a R64D-KcsA mutant >50 μs. The results of this simulation showed lipid residence times similar to KcsA-Kv1.3. Moreover, in KcsA-Kv1.3, lipid headgroups do only moderately modulate specific lipid binding (Figure 3c), since both positively charged PC and negatively polarized PG headgroups encounter an attractive and a repulsive partner in the D64–R89 pair. In KcsA, however, the headgroup has a major influence on specific lipid binding. While PC headgroups are repulsed by residues R64 and R89, PG headgroups are attracted and remain tightly bound, which explains the much longer lifetimes for DPPG (Figure 3d). Note that the description of the headgroups as charged beads is presumably a good characterization of nonannular lipid binding to KcsA, which seems to be sensitive to the headgroup's charge, however not to its exact structure.[98,106]

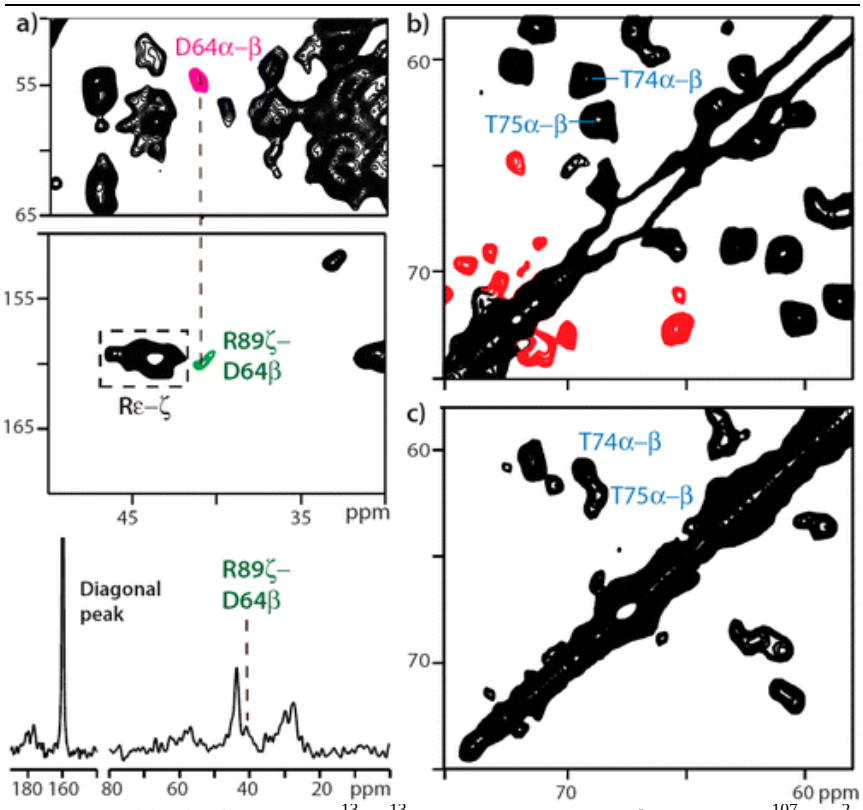

Figure 4. (a) (top) A 2D ^{13}C–^{13}C ssNMR rotational resonance[107] (R^2) experiment confirmed the presence of salt-bridge D64–R89 in KcsA-Kv1.3. (bottom) Cross-section along ω_2 at ω_1 = 159.9 ppm. (b,c) 2D-ssNMR PARIS[108,109] ^{13}C–^{13}C spin diffusion measurements were performed on (b) KcsA and (c) LVWY reverse-labeled KcsA-Kv1.3[69] to probe for tightly bound lipids, copurified from *E. coli*. The mixing time was 30 ms. Lipid headgroup cross-peaks are shown in red. Protein cross-peaks characteristic for the channels' conductive state are assigned.[69]

Structural Studies: Solid-State NMR. The CGMD simulations indicate weaker nonannular lipid binding to KcsA-Kv1.3 as a direct consequence of salt-bridge D64–R89. Notably, also the crystal structure of bacterial channel KvAP,[110] solved in detergent micelles, suggests a salt-bridge between residues D185 and K210, which would be the equivalent to interaction D64–R89. We used our recently suggested strategy[80] to validate MD simulations by tailored ssNMR experiments to probe whether this salt-bridge is conserved in KcsA-Kv1.3 in the presence of lipid bilayers. We performed 2D 13C–13C rotational resonance[107] experiments on KcsA-Kv1.3 reconstituted in asolectin

liposomes, for which ssNMR assignments of the residues D64 and R89 have been reported previously.[69] As shown in Figure 4a, these experiments unequivocally confirmed the presence of key interaction D64–R89 in line with our computational findings.

Furthermore, we used ssNMR 2D PARIS[108,109] ^{13}C–^{13}C experiments to better characterize the properties of nonannular lipid binding to KcsA and KcsA-Kv1.3, which were both reconstituted in asolectin liposomes. For KcsA, we observed cross-peaks between 60 and 80 ppm (Figure 4b), which is the fingerprint region of lipid headgroups, consistent with specifically bound POPG (Figure 4b).[111] Note that all serine and threonine residues, which are the only amino acids that show intraresidual correlations in this region, have been previously assigned.[69,73] Since the asolectin lipids were not 13C-labeled, the lipid cross-peaks are indicative for the presence of tightly bound lipids, copurified from the E. coli inner membrane.

Furthermore, these ^{13}C–^{13}C lipid cross-peaks imply lipid binding times in the microsecond range or longer but exclude shorter lifetimes and are thus in agreement with the CGMD simulations. Remarkably, while we could detect correlations of copurified lipids in the KcsA spectrum, these correlations were either entirely missing or much weaker for KcsA-Kv1.3 (Figure 4c). The results are consistent with the CGMD simulation data showing decreased nonannular lipid residence times for KcsA-Kv1.3 (Figure 3c,d). Note that even if copurified 13C-labeled lipids would dissociate from the channel after the sample purification process, their presence in the KcsA spectrum is still indicative for stronger nonannular lipid binding. It is important to point out that the differences in binding of copurified lipids between the channels in the ssNMR spectra very likely directly relate to the extracellular nonannular site because KcsA and KcsA-Kv1.3 share the same residues on the cytoplasmic side and differ only in a small number of residues on the extracellular side. Note that the detection of lipid headgroups by ssNMR is not in contradiction to crystallographic data, which could not resolve the headgroup of nonannular lipids,[33] because the NMR time scale allows observation of more mobile fragments. Partial disorder of the bound lipid headgroups may also impede their resolution in KcsA crystal structures. [33] In line with such a notion, ssNMR spectra on KcsA are consistent with at least two lipid-spin systems (Figure 4b).

Possible Implications for KcsA Activity. It has been reported in several studies that anionic lipids modulate KcsA's open probability.[33,98]

However, the question of how nonannular anionic lipids modulate KcsA remains unanswered. Here we propose a model which is further supported by atomistic simulations, which would reflect how anionic nonannular lipid binding influences KcsA activity. In addition to the lipid effect on the channel open probability, [33,98] the low open probability of KcsA under steady-state conditions has been attributed to a relatively swift transition from the opened to the inactivated state.[12,27] The transition to the inactivated state in KcsA, which shares analogy with C-type inactivation in Kv channels,[12,19] comes along with molecular rearrangements within the selectivity filter.[12,21] Both the nonannular binding site discussed here and the selectivity filter are located on the extracellular channel side. It has been demonstrated that the selectivity filter in KcsA is regulated by a hydrogen-bonding network, especially involving a triad formed by residues E71-D80-W67.[12,13,19,20] Remarkably, mutation E71A in KcsA, which disrupts interaction E71A-D80, also changes the B-factors of R64 in comparison to the wild-type channel, which could imply that the flipped D80 in the E71A mutant directly or indirectly interacts with R64.[12] Consistent with this idea is the observation that C-type inactivation is significantly slowed down in the KcsA mutant R64A. [12]

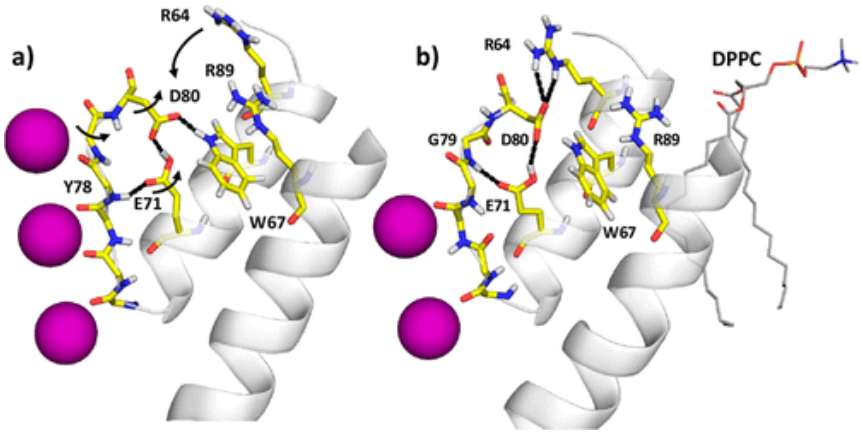

Figure 5. (a) Snapshot of an atomistic MD simulation of KcsA in zwitterionic lipids (DPPC) showing triad E71-D80-W67, which is pivotal to the inactivation process in KcsA. (b) Since DPPC headgroups do not tightly interact with R64 or R89 side chains, both side chains turn toward the protein interior, disturbing the triad, which is an important component of KcsA gating.

We used atomistic MD simulations to examine potential effects of R64 and R89 on the triad E71-D80-W67. Indeed, in zwitterionic lipids,

neither R64 nor R89 markedly interacted with lipids headgroups but turned toward the protein interior, interacting with the carboxyl group of D80, weakening or even disrupting the triad E71-D80-W67 (Figures 5a,b). In the simulations, the reorientation of the carboxyl group of D80 furthermore influenced the conformation of E71, which led to a distortion of the extracellular entrance of the filter, in resemblance of the inactivated state.[112]

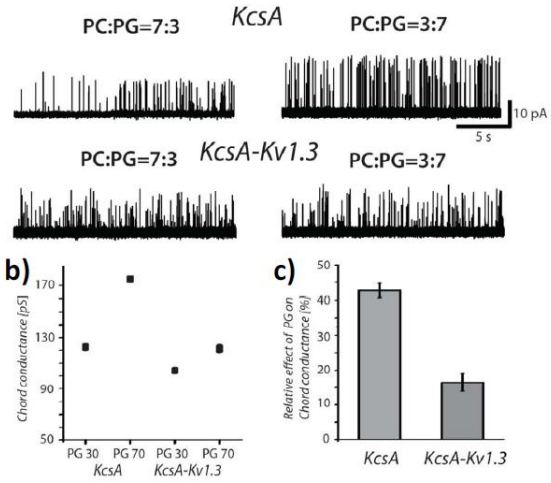

Figure 6. a) Representative current traces of KcsA and KcsA-Kv1.3 recorded in symmetrical 150 mM KCl at +100 mV in different molar fractions of DOPG. b) Absolute and c) relative values of chord conductance of KcsA and KcsA-Kv1.3 recorded in different molar fractions of DOPG.

Hence, we hypothesize that in the absence of anionic lipids, the side chains of R64 and R89 relocate and modulate the hydrogen-bonding network behind the selectivity filter, which could be important for KcsA channel activity. This view is further supported by electrophysiological measurements (Figure 6) that suggest a decrease in channel activity with decreasing molar fraction of anionic lipids in KcsA but not in the case KcsA-Kv1.3. Since the transition to the inactivated state of KcsA was proposed to show cooperative behavior,[113] it could also be imagined that marked cooperative specific lipid binding, which we observe in CGMD simulations, is reflected in channel activity.

Furthermore, our data on KcsA-Kv1.3 suggest that in certain Kv channels (Figure 1), the formation of an intersubunit salt-bridge between S5 and S6 helices diminishes the influence of specific anionic lipid binding to the pore domain on channel activity. Interestingly, an intersubunit salt-bridge in proximity to the selectivity filter reminiscent of D64–R89 in KcsA-Kv1.3 was shown to modulate inactivation in Kir1.1 inward rectifier.[114] The formation and dissolution of salt-bridge D64–R89 itself may hence be of general functional importance. SsNMR studies of KcsA-Kv1.3 revealed that while residue D64 could be clearly assigned in the conductive state, its resonances could not be assigned in the inactivated state,[17] presumably due to enhanced mobility or due to conformational rearrangement. We propose that dissolution of salt-bridge D64–R89 in the inactivated state of KcsA-Kv1.3 influences other residues behind the selectivity filter, in analogy to R64 and R89 of KcsA in the absence of negatively charged lipids.

Conclusions

We have compared specific lipid binding to potassium channels KcsA and chimeric KcsA-Kv1.3 on the structural and functional level. Taken as a whole, our data demonstrate the functional importance of nonannular anionic lipid binding to KcsA, with the channel's activity correlating markedly with strong, highly specific, and cooperative binding of anionic lipids to the channel's extracellular nonannular site (see also Figure 6). In addition, specific annular lipid binding may be a further origin of the influence of anionic lipids on channel activity. Together, our data provide a framework to derive a molecular mechanism of the functional influence of specific lipid binding to KcsA. Moreover, our study demonstrates a reduced functional influence of nonannular lipid binding to the pore domain of KcsA-Kv1.3 and points to a functional role of a salt-bridge between adjacent channel subunits, which may occur in many mammalian Kv channels.

In our contribution, we exclusively discuss specific lipid binding to the extracellular side of KcsA. Remarkably, in a recent contribution,[115] using the noninactivating KcsA mutant E71A, a functional role of the cytoplasmic N-terminal helix as a kind of lipid sensor was described, which points to an even more important impact of specific lipid binding on KcsA. We like to stress that an effect of nonannular lipid binding on the inactivation gate, which we infer from our data, is unlikely to be observable with KcsA mutant E71A, the inactivation gate of which is always open.[12] Note that besides the here discussed influence of direct

specific lipid binding to already membrane-inserted proteins, specific lipid–protein interactions, and thus the membrane composition, can critically affect membrane protein topogenesis and initial assembly.[116,117]

CGMD simulations overcome the typical length and time scale problem of atomistic simulations, which are usually limited to system sizes and simulation times <10 nm and a few hundreds of ns. Notably, the increase in system size and sampling time greatly enhances the potential to compare computational observations to powerful experimental techniques like confocal microscopy or ssNMR.[90,118] This has been exploited to shed light on intricate phenomena like lipid domain formation or membrane protein lateral distribution.[90,119] Such processes are notoriously difficult to study experimentally and are likely critically involved in forming membrane protein supramolecular structures and in membrane organization in general. Combining CGMD simulations and ssNMR experiments as shown here allows for the characterization of structural and dynamical features of nonannular lipid binding and of specific lipid–protein interactions in general in a membrane setting and at atomic scale.

Experimental Section

Molecular Dynamics Simulations. Coarse-grained (CG) simulations were carried out using the GROMACS simulations package version 4.5.3[81] and the MARTINI[102,103] force field and its extension to proteins, together with an integration step of 25 fs and the standard settings for nonbonded interactions in a NPT ensemble with period boundary conditions. Simulation times were multiplied by a factor 4 to account for the smoothness of the CG potentials. The system was semi-isotropically coupled to a pressure bath at 1 bar (τ_p = 3 ps) and coupled (τ_T = 0.3 ps) to a heat bath. A solvated mixed DPPC:DPPG (3:1 molar ratio) bilayer, consisting of 1536 DPPC lipids, 512 DPPG lipids, 25 088 water, and 512 sodium GC-beads, was self-assembled and equilibrated over 4.4 μs at 323 K, which resulted in a large membrane patch with dimensions of 25.2 × 25.2 nm^2. A frame of this system was extracted after 4.4 μs, and the closed-conductive KcsA-Kv1.3 channel inserted while keeping the PC:PG 3:1 ratio. This system was equilibrated over 20 μs while keeping the channel core comprising the filter (backbone and side chain beads) and the intracellular side (backbone beads only),

corresponding to residues 22–49, 67–82, and 91–115, rigid throughout all simulations. Position restraints on the backbone beads of the residues at the membrane/water interface (residues 50–66 and 83–90) of the extracellular side were gradually reduced during equilibration and very light position restraints of 10 kj/mol·nm^2 were applied during the final runs. KcsA was inserted in two different mixed bilayers extracted after 4.0 and 4.4 μs to minimize the influence of the initial lipid distribution. The KcsA-Kv1.3 CGMD model was converted from an atomic-resolution ssNMR structure, which will be discussed elsewhere and which was derived from extensive ssNMR measurements in lipid bilayers.[69,73] All common resolved ssNMR chemical shifts showed very little deviation, which confirmed the conservation of KcsA's fold in KcsA-Kv1.3, so that we could derive KcsA's starting structure by back-mutating KcsA-Kv1.3 to enhance the comparability of the simulations. Since we noted that a lipid shell of 3.5 nm around the channel remained in the liquid phase during all simulation,[120] even below the phase-transition temperatures of DPPC/PG, we carried out the final runs at 300 K to be closer to the temperatures used for ssNMR and electrophysiological experiments.

Atomistic simulations were performed with the GROMOS53a6 force field[87] and the Berger lipid parameters.[121] The initial coordinates for a hydrated 128 DPPC bilayer were taken from Dr. Tieleman's Web site (moose.bio.ucalgary.ca). This patch was expanded to 512 lipids, minimized, equilibrated over 10 ns and the closed-conductive KcsA channel (PDB code 3EFF), [71] truncated to residues 22–115, inserted.[122] The temperature was kept constant at 320 K. Ions (80 mM KCl) and water molecules as well as lipids and the protein were jointly coupled to the thermostat. The system was first equilibrated in a NVT ensemble, then for 10 ns in a NPT ensemble using semi-isotropic pressure coupling with gradually reduced force constants and finally freely evolved over 35 ns. See Supporting Information for further details.

Sample Preparation. Expression and purification of LVWY reverse-labeled KcsA-Kv1.3 and uniformly labeled KcsA have been described in ref [68]. For the ssNMR experiments, reconstitution was performed at a 100:1 lipid/protein molar ratio. For the single channel recordings, unlabeled KcsA and KcsA-Kv1.3 were reconstituted at 1000:1 lipid/protein mass ratio. Both KcsA and KcsA-Kv1.3 were in the closed-conductive state.

SsNMR Spectroscopy. The ssNMR experiments were measured in magnetic fields of 11.7 T. 2D PARIS ^{13}C–^{13}C spin diffusion experiments[108,109] (pulse length = $0.5\tau_{rot}$, 13 kHz recoupling amplitude) were carried out at 20 kHz *MAS* and 265 K with mixing times of 30 ms using PISSARRO decoupling.[123] The rotational resonance[107] (R^2) experiment was performed at 269 K and 15 kHz MAS, close to the chemical shift difference of 14.9 kHz between D64Cβ and R89Cζ. No decoupling was applied during 150 ms mixing time, to broaden the R^2 condition,[124] and SPINAL64 decoupling[86] was applied during acquisition periods.

Single Channel Measurements Single channel recordings of KcsA were performed on planar lipid bilayer setup (Compact, Ionovation GmbH). Lipid bilayers were formed by painting the lipids dissolved in n-decane over a 200 μm hole in a Teflon-septum that separated two chambers (*cis* and *trans*). Initially, the *trans* chamber contained 20 mM KCl, the *cis* chamber 250 mM KCl, both of which were buffered to pH 4.0 with 10 mM succinic acid. KcsA proteoliposomes (1–5 μL) were added to the *cis* chamber of the planar bilayer system with a micropipet. After channel insertion, recording conditions were established by perfusion to symmetrical conditions. The *cis* side contained 150 mM KCl and 10 mM HEPES at pH 7.0, and the *trans* side contained 150 mM KCl and 10 mM succinic acid at pH 4.0. All measurements were performed at room temperature. Data are sampled at 10 kHz and filtered at 1 kHz. Reported data are result of statistical analysis of 3–5 independent experiments.

Chapter 4

Quantitative Analysis of the Water Occupancy around the Selectivity Filter of a K^+ Channel in Different Gating Modes

Markus Weingarth,†Elwin A. W. van der Cruijsen,† Jared Ostmeyer,‡ Sylke Lievestro,† Benoît Roux,‡ and Marc Baldus†

† NMR Spectroscopy, Bijvoet Center for Biomolecular Research, Department of Chemistry, Faculty of Science, Utrecht University,
‡Department of Biochemistry and Molecular Biology, The University of Chicago

Journal of American Chemical Society 2014 Feb 5;136(5):2000-7

Abstract

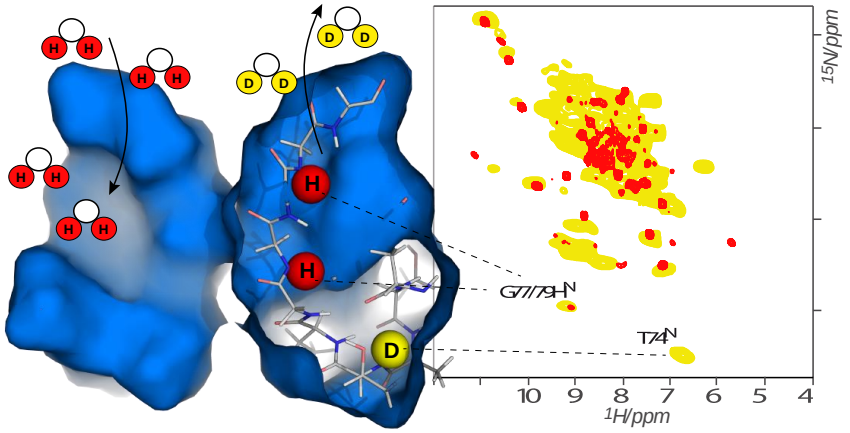

Recovery in K^+ channels, that is, the transition from the inactivated nonconductive selectivity filter conformation toward the conductive conformation, occurs on a time scale of the order of seconds, which is astonishingly long, given that the structural differences among the filter conformations are faint (<1 Å). Computational studies and electrophysiological measurements suggested that buried water molecules bound behind the selectivity filter are at the origin of the slowness of recovery in K^+ channels. Using a combination of solid-state NMR spectroscopy (ssNMR) and long molecular dynamics simulations, we sketch a high-resolution map of the spatial and temporal distribution of water behind the selectivity filter of a membrane-embedded K^+ channel in two different gating modes. Our study demonstrates that buried water molecules with long residence times are spread all along the rear of the inactivated filter, which explains the recovery kinetics. In contrast, the same region of the structure appears to be dewetted when the selectivity filter is in the conductive state. Using proton-detected ssNMR on fully protonated channels, we demonstrate the presence of a pathway that allows for the interchange of buried and bulk water, as required for a functional influence of buried water on recovery and slow inactivation. Furthermore, we provide direct experimental evidence for the presence of additional ordered water molecules that surround the filter and that are modulated by the channel's gating mode.

Introduction

Potassium (K^+) channels share a common pore architecture for catalyzing the diffusion of ions across membranes.[11,125] Ion passage is controlled by two coupled gates.[17,22,126,127] They are located at either end of the channel pore and called the activation and inactivation gates. The inactivation gate is also known as the selectivity filter. Activation gating is associated with relatively large hinge-bending and rotational motions of the inner helix bundle, dilating the pore by about one nanometer upon channel opening.[78] In contrast, inactivation gating is accompanied by angstrom-scale local structural changes within the selectivity filter.[12,13,18,128] Crystal structures of KcsA from Streptomyces lividans obtained at low (3 mM, PDB: 1K4D) and high (200 mM, PDB: 1K4C) K^+ concentration [K^+][9] are commonly considered as representative for the closed-inactivated and closed-conductive channel gating modes, respectively.[128,129] According to these conformations, rearrangements within the selectivity filter upon inactivation are confined to a partial flip of the V76–G77 peptide plane, pinching the filter shut. The small structural differences between the conductive and inactivated selectivity filter, however, stand in sharp contrast to the remarkably long time scale of seconds on which recovery from slow inactivation, that is, transition from the inactivated toward the conductive filter state, occurs. Recent molecular dynamics (MD) simulations[130] showed that this apparent discrepancy could be explained by the dynamics of buried water molecules bound in the back of the inactivated selectivity filter, which lock the filter in the inactivated state. MD simulations further predicted that conversion to a dewetted conductive state could only occur upon release of the inactivating water to the bulk, which was indirectly corroborated by the measurement of an accelerated recovery rate at high osmotic stress.

In a broader sense, such buried water molecules can be considered as an inherent part of the channel structure. Nevertheless, many unanswered questions remain regarding the mechanism by which the water modulates the free energy landscape associated with the conformational space of the selectivity filter, and how the distinct water occupancies are correlated with different filter conformations.[24] Previously, we have demonstrated that solid-state nuclear magnetic resonance (ssNMR) is a powerful technique to study the structural and dynamical properties of membrane-embedded KcsA variants before and after channel inactivation.[17,18,131] Here, we combined ssNMR studies with long MD simulations to provide a high-resolution spatial and temporal

arrangement of buried water in the rear of the conductive and the inactivated filter of membrane-embedded KcsA, which corroborates that buried water is at the molecular origin of the slowness of recovery. Moreover, we demonstrate the use of high-resolution ^{1}H detected ssNMR on a fully protonated membrane protein to dissect in atomic detail a pathway that allows the interchange of buried and bulk water, as it was suggested to be required for recovery and slow inactivation. Finally, we provide direct experimental evidence for the presence of other sources of ordered water that surround the filter and that are modulated by the states of the activation and inactivation gates.

Results and Discussion

Spatial Distribution of Ordered Water around the Selectivity Filter before and after Inactivation. In general, ssNMR experiments can report on water proximities by making use of the distinct ^{1}H chemical shift of the water resonance and the fact that polarization transfer schemes such as cross-polarization (CP) or longitudinal mixing report, in the initial rate regime, on local proton–proton proximities,[132] and chemical exchange with bulk water can be neglected.[77] For $^{1}H \rightarrow X$ transfer, we used short CP times that restrict polarization transfer to the nearest neighbor (i.e., bonded) X nucleus.[132] Thus, ^{15}N edited experiments probe proximities around NH protons, whereas ^{13}C edited experiments are sensitive to water located close to aliphatic carbons. Note that all amino protons of the selectivity filter that we use as magnetization receptors in the ^{15}N detected experiments point directly toward the back of the filter, while aliphatic protons may be oriented toward the pore and the lower channel cavity.

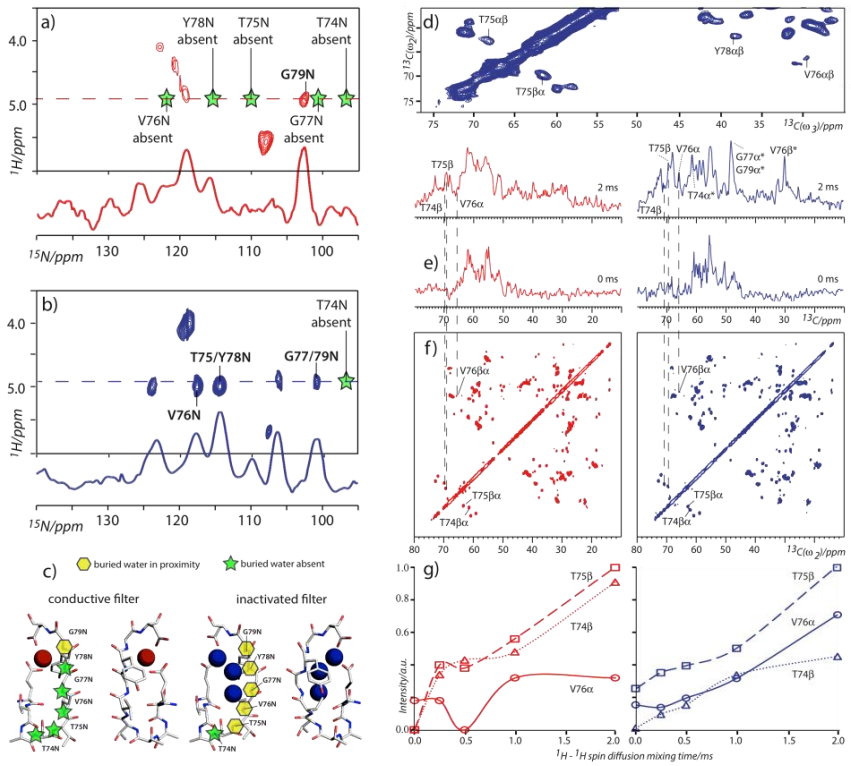

Figure 1. 2D 1H(1H)15N ssNMR spectra of membrane-embedded KcsA in (a) the closed-conductive and (b) the open-inactivated state, measured at 52 kHz MAS. Cross sections along ω_2 at the ^{1}H water resonance are shown for both channel states. (c) The spatial distribution and content of crystal water behind the conductive (left, PDB: 1K4C) and inactivated (right, PDB: 1K4D) selectivity filter are consistent with our ^{1}H(^{1}H)^{15}N ssNMR data. Yellow hexagons and green stars indicate 15N nuclei for which ssNMR experiments suggest the presence and the absence of buried, nearby water molecules, respectively. (d) ^{13}C–^{13}C plane at the 1H water resonance of a 3D ^{1}H(^{1}H)^{13}C^{13}C spectrum measured on open-inactivated KcsA. (e) Cross sections, extracted from a series of 2D ^{1}H(^{1}H)^{13}C measurements with varying ^{1}H spin diffusion time (2 and 0 ms from top to bottom), along ω_2 at the water resonances for both the conductive (red, left panel) and the inactivated (blue, right panel) state. Signals that are ambiguous due to spectral overlap are marked with asterisks. (f) T74, T75, and V76 resonances can be retraced in PARIS[108,133] ^{13}C–^{13}C spin diffusion spectra for conductive (red, left) and inactivated filter (blue, right) conformation. (g) Build-up curves at the 1H water resonance in the conductive (red, left) and inactivated (blue, right) conformations, extracted from a series of 2D ^{1}H(^{1}H)^{13}C experiments. Signal intensities were deduced from peak heights (T74Cβ in dotted lines and triangles, T75Cβ in dashed lines and squares, and

V76Cα in continuous lines and circles). For each panel, the plots were normalized with respect to the most intense cross peak.

First, we recorded 2D ssNMR $^{1}H(^{1}H)^{15}N$ spectra of membrane-embedded KcsA (see Experimental Section for a detailed description of the ssNMR setup) before and after channel inactivation. Using ^{13}C and ^{15}N resonance assignments obtained previously,[18,69,131] these data provided clear evidence for higher water occupancy behind the inactivated selectivity filter (with an open activation gate) in comparison to the conductive filter conformation (with a closed activation gate). In the closed-conductive state (Figure 1a, red), only the upper part of the filter (G79N) showed an intense correlation with the water resonance, while such correlations were weak or entirely absent for residues of the middle and lower parts of the filter (T78N–T74N). In the open-inactivated state (Figure 1b, blue), buried water is distributed along the entire rear of the filter (G79–T75), with the exception of the lowest part of the filter (T74N) that is right above a large water-filled cavity. The slightly different ^{1}H shifts of water in Figure 1b may indicate the presence of several water molecules behind the inactivated filter. Taken together, these ssNMR findings for the conductive and inactivated, membrane embedded channel state are hence in excellent agreement with the spread and content of buried water molecules in the low $[K^+]$ and high $[K^+]$ crystal structures,[9] respectively (Figure 1c).

To characterize the distribution of buried water around aliphatic protons, we carried out a 3D $^{1}H(^{1}H)^{13}C^{13}C$ experiment. For open-inactivated KcsA, this experiment (Figure 1d) revealed clear signals in the ^{13}C–^{13}C plane at the ^{1}H water resonance for residues Y78, V76 and T75, while T74 was absent. These findings are in line with our $^{1}H(^{1}H)^{15}N$ data (Figure 1b) and confirm that buried water is confined to the upper and the middle passages behind the inactivated filter. Interestingly, ^{13}C–^{13}C cross-peaks of T75, that is located close to the dewetted residue T74, were more intense than for V76. This is not inferable from the low $[K^+]$ crystal structure in which buried water is closer to V76 than to T75. The apparent closer proximity in the inactivated filter conformation of T75 to ordered water in comparison to V76 observed by our ssNMR data could be confirmed in a series of 2D $^{1}H(^{1}H)^{13}C$ experiments with varying ^{1}H–^{1}H mixing time (Figure 1e–g). These results suggest that cross-peak intensities correlate to differential exposure to ordered water and that they are not modulated by the ^{13}C–^{13}C PARIS spin diffusion step. The same set of ^{13}C detected experiments performed on a sample in the closed-conductive state showed an exposure to ordered water that increased toward the large

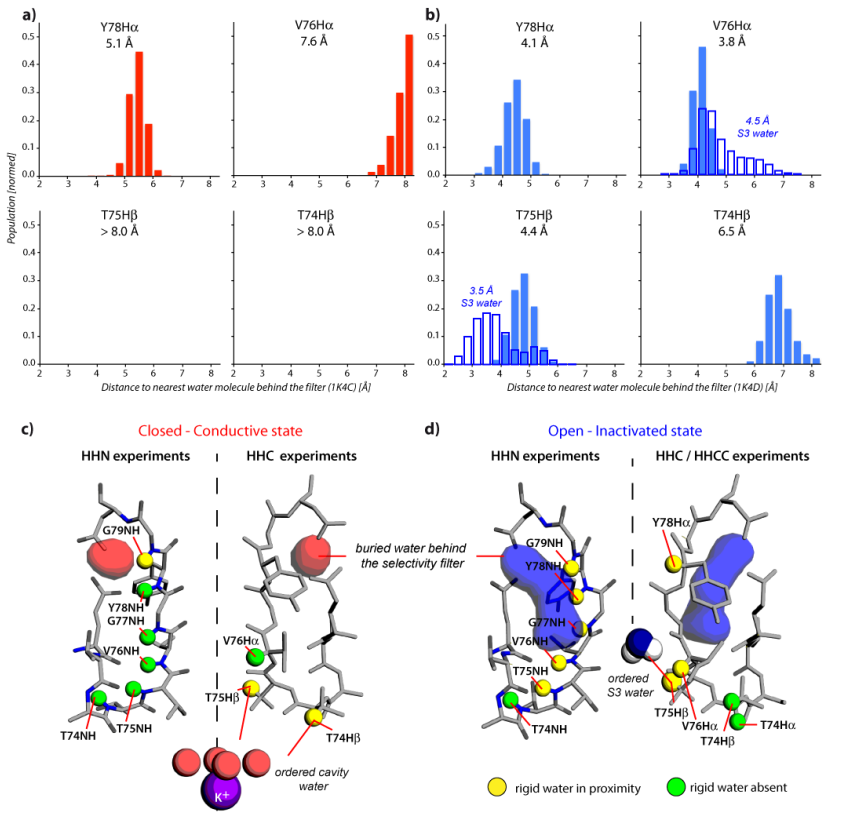

Figure 2. (a) The distribution of nearest distances to protons of water bound behind the selectivity filter (filled columns), averaged over a long MD simulation of closed-conductive KcsA (starting with crystal structure 1K4C), calculated for filter residues resolved in $^{1}H(^{1}H)^{13}C$ ssNMR experiments. The mean distances, estimated from MD simulations, are indicated. (b) Same as described in (a) for the closed-inactivated channel (starting with 1K4D). For residues V76 and T75, the nearest distances to protons of S3 water are superposed (open columns). Notably, during about 15% of the trajectory, S3 water is closer than 3.0 Å to T75Hβ, which would pronounce spin diffusion transfer that exhibits a r^{-6} dependence on the internuclear distance r. (c) Snapshot of a 1K4C simulation, representative for the distribution of buried water behind the conductive filter. The ordered K^+ hydration shell of cavity water that was resolved in crystal structure 1K4C is illustrated below the filter. (d) Snapshot of a 1K4D simulation, representative for the distribution of buried water behind the pinched filter and the water molecule at the S3 position of the filter pore. The protons used as magnetization receptors in $^{1}H(^{1}H)^{13}C/^{15}N$ ssNMR experiments are highlighted with spheres. Protons for which we observed in ssNMR experiments the proximity and the absence of buried water are color-coded in yellow and green, respectively.

water-filled cavity (T75 and T74). Notably, a few protons such as T74Hβ and T75Hβ of the selectivity filter that are monitored in our ^{13}C detected experiments point toward the selectivity filter pore and the large water-filled cavity (vide infra).

These results suggested that the ^{13}C detected experiments are, in addition to water behind the selectivity filter, sensitive to the presence of other ordered water molecules. We therefore calculated the nearest distances of water to the residues that we monitor in ^{13}C detected experiments over long MD simulations for both conductive and inactivated filter conformations (Figure 2a,b). For the conductive filter, the simulations clearly showed (Figure 2a) that water behind the filter is too distant (>8.0 Å) to transfer magnetization to T75 or T74, raising the question of what causes the high water access in ^{13}C detected experiments for these two residues. Ordered water within the conductive filter pore is unlikely, because water has to transverse the filter within nanoseconds to ensure fast ion flux. We hypothesize that the increased water access stems from ordered water in the closed large cavity forming a hydration complex to help K^+ to overcome the high dielectric barrier of the bilayer and to position K^+ optimally to the filter.[9,134] Our ssNMR data suggest that both T75 and T74 are in proximity of such ordered cavity water, presumably stabilizing it with their hydroxyl functions (Figure 2c). Because the inner helix is supposed to stabilize ordered cavity water and moves outward upon channel opening, dilating the cavity,[78] water order is presumably influenced by the mode of the activation gate and therefore attenuated in the open cavity. Indeed, in the open-inactivated state, residue T74 shows weak water access in ^{13}C detected experiments (Figure 1d,g). It is interesting to think about a functional role of the close proximity of the first or second ion-hydration layer to the entrance of the selectivity filter, bearing in mind that Na^+ and K^+ feature hydration shells in the cavity that are different in shape and order and also bind there with different affinities.[9,10]

The computational analysis also confirmed that water behind the inactivated filter is closer to V76Hα than to T75Hβ (Figure 2b), which means that buried water alone is unlikely to account for the high water access of T75Hβ. Remarkably, an ordered water molecule was also cocrystallized in the inactivated filter at the S3 position.[9] Such water, as shown by simulations, is very close to T75Hβ (Figure 2b,d), often closer than 3.0 Å, and would account for its high water access in the ^{13}C detected experiments. This water in the filter featured residence times

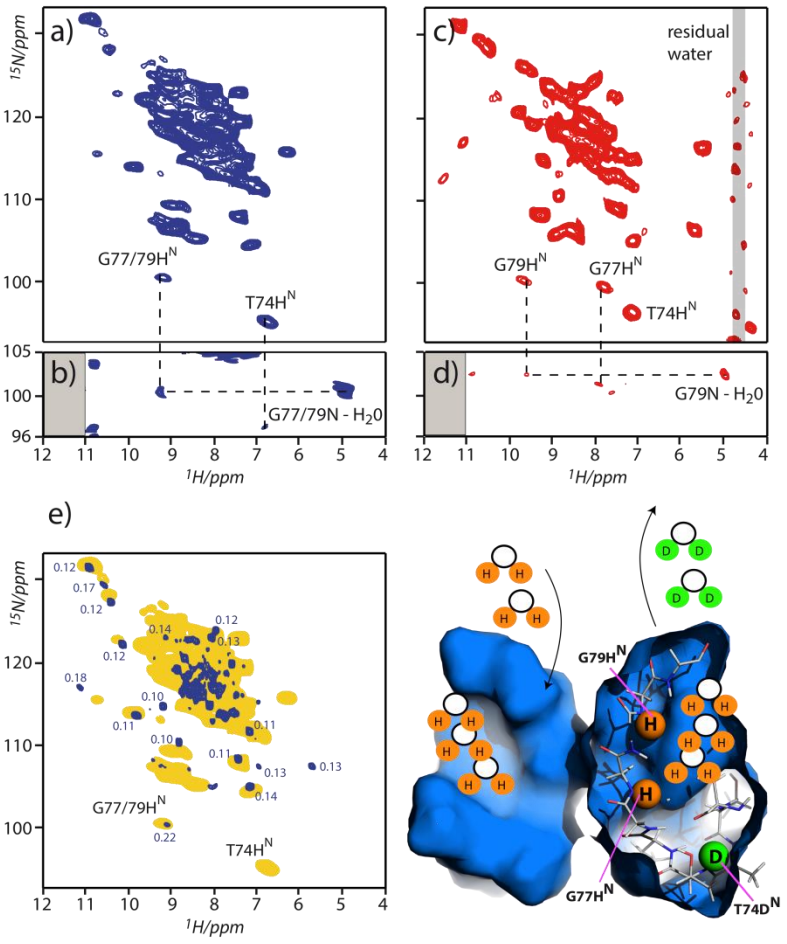

Figure 3. (a,c) 2D ^{15}N–^{1}H spectrum of fully protonated open-inactivated and closed-conductive KcsA, respectively, measured at 60 kHz MAS and 18.8 T static magnetic field (800 MHz ^{1}H frequency). (b,d) Cutouts of $^{1}H(^{1}H)^{15}N$ ssNMR spectra of open-inactivated and closed-conductive KcsA, respectively. The gray boxes indicate the limits of the spectral width, and the adjacent signal intensity is spurious. (e) (right) Comparison of 2D NH data on (^{1}H,^{13}C,^{15}N; in yellow) membrane-embedded KcsA in the open-inactivated state to an equivalent (^{2}H,^{13}C,^{15}N; in blue) sample after washing in acidic H_2O buffer. The blue numbers represent the ^{1}H line width at half-height (in ppm) of resolved cross-peaks and the G77/G79 signal extracted from the spectrum of the back-exchanged deuterated channel.

around the microsecond range in the simulations, which will be longer at the temperatures used in our ssNMR experiments (283 K).

Taken together, our ^{13}C and ^{15}N detected ssNMR data, in reference to simulations, provide a high-resolution map of the spatial distribution of ordered water around the selectivity filter. Buried water is spread all along the inactivated filter's rear with the exception of T74, and our data suggest ordered water at the S3 position in the inactivated filter (Figure 2d). In the conductive filter, only the upper, extracellular part (G79) is in direct contact to buried water, while the rest of the filter is devoid of it. Moreover, with a closed activation gate, T75 and T74 seem to be in close proximity to the ordered hydration shell of cavity ions (Figure 2c).

High-Resolution ^{1}H ssNMR To Probe Water Dynamics Behind the Selectivity Filter. As an alternative and more direct means to probe the presence of buried water molecules, we resorted to high-resolution ^{1}H ssNMR that can be obtained by using very fast MAS rates (see, e.g., refs [135,136]) and/or by perdeuteration.[137,138] In the latter case, ^{1}H ssNMR requires the reprotonation of protein sites via exchange with H_2O. For membrane proteins, this process is significantly slower for residues that are not solvent exposed and shielded by the lipid bilayer.[139] This property provided us with a unique opportunity to directly track residues that become protonated due to buried water on the time scale of channel recovery from C-type inactivation.

To ensure the identification of water-accessible and nonaccessible amino-protons ($^{1}H^{N}$), we first acquired ^{1}H detected 2D ^{15}N–^{1}H experiments at 60 kHz MAS with fully protonated open-inactivated and closed-conductive KcsA. As compared to previous work on microcrystalline proteins,[140,141] these experiments resulted in remarkably narrow $^{1}H^{N}$ line widths of 0.3–0.5 ppm for a membrane-embedded ion channel. Spectrally well-separated ^{15}N chemical shifts of filter residues T74, G77, and G79 allowed us to identify their $^{1}H^{N}$ both in indirectly and directly ^{1}H detected spectra (Figure 3a–d). To our knowledge, these assignments present the first ^{1}H site-specific analysis of a fully protonated membrane protein by ^{1}H detected biomolecular ssNMR. The resolution in our ^{15}N–^{1}H spectrum of fully protonated closed-conductive KcsA opened the possibility to monitor structural changes in reference to function in the canonical GYG motive of the K^{+} channel superfamily. Crystal structures[9] showed G77NH to flip upon inactivation, and G77H^{N} indeed exhibited a stark ssNMR resonance shift (+Δ1.8 ppm) to low-field in the inactivated filter

conformation (Figure 3a,c). As revealed by a computational analysis, the chemical shift change of $G77H^N$ may reflect the rotation of G77NH away from the filter's rear, where $G77H^N$ is less exposed to the shielding ring-current effect of Y78 (Figure 4). Moreover, the shift of $T74H^N$ toward high-field (−Δ0.5 ppm) upon opening of the activation gate is in line with a flip of the F103 ring-plane, facing T74, which was shown to be critically involved in the coupling of activation gate and selectivity filter.[22,142] Note that such investigations of proton chemical shifts are precluded when using perdeuterated samples, because $T74H^N$ and $G77H^N$ are not exposed to water in all filter states (Figure 1a,b).

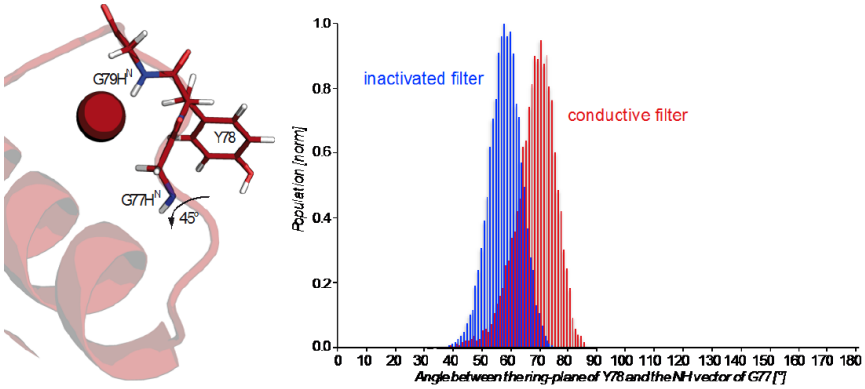

Figure 4. (right) Crystal structures (pdb-code 1K4C and 1K4D) showed G77NH to flip upon inactivation, and $G77H^N$ indeed exhibited a stark ssNMR resonance shift (+Δ1.8 ppm) to low-field in the inactivated filter conformation (see Figure 3a,b). (left) A computational analysis shows that $G77H^N$ moves away from the shielding effect of the Y78 ring-plane if the filter adopts the inactivated conformation. The angles were measured over the course of the Molecular Dynamics simulations between the vector normal to the plane of Y78 and the vector spanning from G77HN to the center of the ring of Y78.

Next, we sought to characterize the water dynamics behind the filter by ssNMR, which is essential to convey a functional importance to buried water. Simulations demonstrated the necessity of an interchange from buried to bulk water to initiate recovery and implied long residence times for buried water to be at the molecular origin of recovery. We intended to study water dynamics by exploiting the exchangeable character of amino protons. For this purpose, we acquired 2D ^{15}N–^{1}H experiments on a membrane-embedded perdeuterated (^{2}H,^{13}C,^{15}N) KcsA sample, which was washed in an acidic (pH 3.5) H_20 buffer solution. We compared our data to results obtained on the fully protonated

channel, which allowed straightforward identification of $^{1}H^{N}$ of G77/G79 as water-accessible and the $^{1}H^{N}$ of T74 as nonaccessible (Figure 3e). Importantly, protonation of G77 and G79 confirmed the presence of a pathway from bulk to buried water that is restricted to the upper part of the filter. An analysis of the ^{1}H line width showed that the G77/G79 $^{1}H^{N}$ signal exhibits a much larger (0.22 ppm) line width than other resolved cross-peaks (0.10–0.13 ppm), suggesting that both G77/G79 amino-deuterons exchanged to ^{1}H (Figure 3e). These results provide direct experimental evidence that bulk water can occupy the cavity behind the selectivity filter, as it was shown to be required for slow inactivation, and also suggest the possibility of the reverse process, release of inactivating water to the bulk, as required for recovery. Importantly, the $^{1}H^{N}$ assignments also hint at the nature of the water hydrogen-bonding network behind the inactivated selectivity filter.[134] While we observe (Figure 3e) that the $^{1}H^{N}$ of G77/G79 are water-exposed, and according to simulations[130] directly hydrogen bonded to buried water, we simultaneously observe sharp G77/G79 $^{15}N–^{1}H^{N}$ and $^{15}N–^{1}H^{H2O}$ correlations (Figure 3b). Hence, these experiments suggest that buried water resides behind the filter on the NMR time scale (and possibly beyond, which is in line with computational studies,[130] in which buried water remained bound behind the inactivated filter during a 17 us MD simulation).

Conclusions

Our study demonstrates the presence of several ordered water molecules surrounding the selectivity filter of membrane-embedded K^{+} channels and that these water molecules are directly correlated with the channel gating cycle. By combining ssNMR experiments and computational data, we could sketch a high-resolution map of the spatial and temporal distribution of buried water behind the filter that clearly shows a plus of water with extended residence times behind the inactivated filter and corroborates the notion that buried water governs recovery kinetics. Moreover, we demonstrated the presence of a pathway that allows for the interchange of buried water and bulk water, as required for recovery and slow inactivation, and we find spectroscopic evidence for conformational changes of the GYG signature sequence that accompany inactivation. We want to emphasize that many of these experimental results were only possible by ^{1}H detection in fully protonated membrane proteins, an approach that bears the capacity to monitor protons of all protein sites irrespective of their access to water. Such studies may have far-reaching advantages to investigate exchangeable protons of the inner

core of membrane and fibril proteins, which have been shown to be exceptionally stable.[139,143,144]

In general, our study illustrates the correlation between selectivity filter conformational space and the exposure to ordered water consistent with the notion of water acting as an inherent part of the gating mechanism that steers the sampling of selectivity filter conformational space. Such processes may be of general importance to the regulation of potassium channels, for instance, by heterogeneous channel opening kinetics, referred to as modal gating.[24,145] In this study, we discovered additional ordered water molecules that are located in and below the filter that could potentially act as regulatory elements of channel function. Moreover, ordered water molecules may enhance the coupling of the selectivity filter to the rest of the channel, acting as mediators that transmit conformational changes in the pore helix and turrets, which are both sensitive to the membrane environment, to the inactivation gate.[131,146]

We have demonstrated the great potential of solid-state NMR to investigate buried water molecules as an intrinsic part of ion channels in a native-like environment with the prospect of studies in native environments.[51] Such studies are of general relevance for membrane proteins, and sources of buried water as structural or functional modulators have been reported for transporters,[147] G protein coupled receptors,[148] and enzymes of the respiratory chain,[149] to name only a few examples. As it was shown by solution NMR,[150,151] such buried water molecules may be further exploited as potential probes of intrinsic protein dynamics and the underlying energy landscape.

Experimental Section

Solid-State NMR Spectroscopy. SSNMR experiments were performed using NMR spectrometers (Bruker Biospin) at magnetic fields of 16.4 and 18.8 T with 52 and 60 kHz magic angle spinning (MAS), respectively. The sample temperature was 283 K (52 kHz MAS) and 300 K (60 kHz MAS). We used 2D $^1H(^1H)^{15}N/^{13}C$ and 3D $^1H(^1H)^{13}C^{13}C$ experiments (Figure 5) to probe buried water molecules, transferring magnetization from rigid protons to protein heteronuclei ^{13}C or ^{15}N by a short cross-polarization step (200 us for ^{13}C, 600 us for ^{15}N). The slightly longer ^1H–^{15}N contact time was chosen to compensate for local backbone dynamics of the selectivity filter.[152] To facilitate transfer from buried water molecules to the protein, a short ^1H–^1H spin diffusion

step (1.2 ms in ^{15}N and 0–2 ms in ^{13}C detected experiments) was added prior to cross-polarization. Our experimental setup is close to those used to relate membrane protein bulk water-accessibility to membrane protein conformation,[77,153,154] with the difference that a T_2 filter to suppress rigid sample components was omitted to avoid relaxation of possibly buried and rigid water molecules. Our experimental setup is sensitive to water that is immobilized on the time scale of microseconds and beyond. Note that the application of very fast MAS in this study allows the observation of ordered water molecules without the necessity of ^{1}H homonuclear dipolar decoupling during the ^{1}H evolution time. ^{13}C–^{13}C spin diffusion mixing at 52 kHz MAS was carried out using PARIS[108,133] with the standard pulse length = $0.5\tau_{rot}$ (N = 0.5) and 30 kHz recoupling amplitude over 200 ms. Heteronuclear high[155] (pulse length $0.9\tau_{rot}$) and low power[156] PISSARRO decoupling was applied during all heteronuclear and proton acquisition periods, respectively. The MISSISSPI solvent suppression scheme[157] was used in ^{1}H detected experiments. ^{13}C and ^{15}N resonance assignments were taken from refs [69,131].

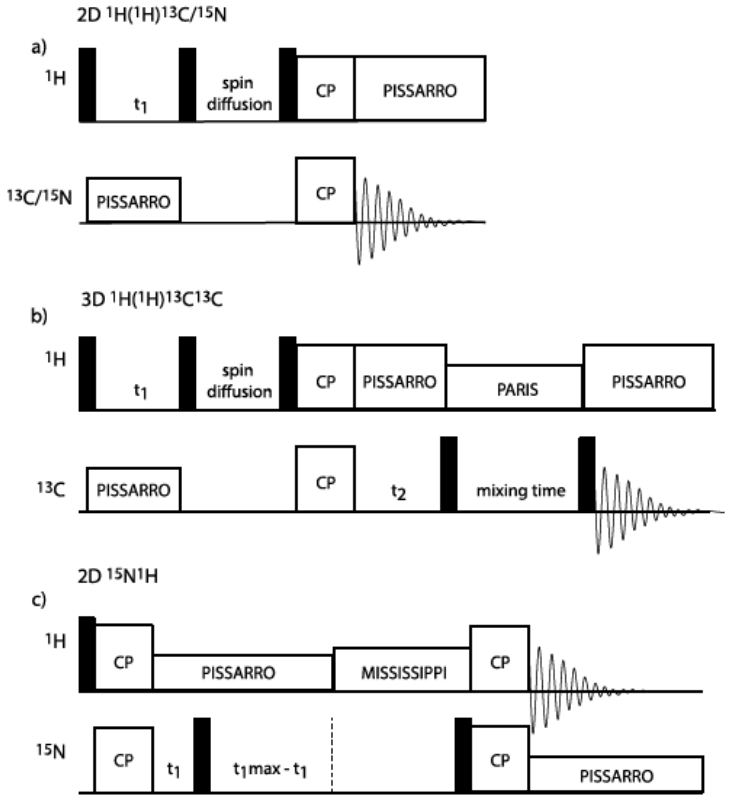

Figure 5. Schematic representation of a) 2D $^1H(^1H)^{15}N/^{13}C$, b) 3D $^1H(^1H)^{13}C^{13}C$ and c) ^1H-detected 2D $^{15}N^1H$ experiments. 90° pulses are indicated by filled rectangular boxes. The MISSISSIPI scheme $[\tau_{p(x)}\ \tau_{p(-x)}\ \tau_{p(y)}\ \tau_{p(-y)}]_L$ (with τ_p = 10 ms and L = 2) for solvent suppression was applied over a total of 80 ms. Low power (LP) PISSARRO decoupling was carried out using standard parameters (decoupling amplitude $\nu_{LP\text{-}decpoupling} \approx \frac{1}{4}\nu_{rot}$; pulse length $\tau_p \approx {}^{15}/_{16\nu_{LP-decoupling}}$).

Sample Preparation. Expression, purification, and reconstitution in asolectin of protonated uniformly ^{13}C, ^{15}N labeled KcsA followed earlier work (refs [68,131]). The perdeuterated KcsA sample was expressed for 12 h to an OD600 of 1.3 in a medium containing 100% D_20, uniformly ^2H, ^{13}C labeled glucose, and $^{15}NH_4Cl$. Uniformly ^2H,^{13}C,^{15}N labeled KcsA was washed two times for 1.5 h in 0 mM K^+/150 mM Na^+/10 mM H_20 citrate buffer. Purification steps where done in neutral H_20 buffers. As in refs [18,131], samples at pH 3.5 were prepared by washing

proteoliposomes with 100 mM citrate buffer, yielding the same ionic strength as the phosphate buffer used for pH 7.5 samples. All reconstitution was performed at a 100/1 lipid/protein molar ratio.

Molecular Dynamics Simulations. Initial coordinates for the Molecular Dynamics simulations of the both the conductive and the pinched selectivity filters were taken from the crystal structures 1K4C and 1K4D, respectively.[9] Crystallographic water molecules for each of the four subunits of the channel were included at the start of the simulations. With the exception of Glu71, which was protonated, all residues were assigned their standard protonation state at pH 7.0. The channels were embedded in a bilayer of POPC lipids and solvated in 1.0 M KCl using the web service CHARMM-GUI (total number of atoms, 45 898). All-atom simulations were run at a temperature of 310 K under constant NVT conditions using the CHARMM PARAM27 force field. Simulations of the conductive filter were run for 510 ns, while simulations of the pinched selectivity filter were run for 17.7 μs. All simulations were carried out on the special purpose computer Anton on loan to the Pittsburgh Supercomputer Center (PSC).[158]

Chapter 5

Open-conductive conformation of KcsA potassium channel: functional and structural aspects

Alexander V. Prokofyev,[†,+,*] Elwin A. W. van der Cruijsen,[†,*] Olaf Pongs[+] and Marc Baldus[†]

[†]Bijvoet Center for Biomolecular Research, Faculty of Science, Utrecht University

[+]Saarland University, Faculty of Medicine, Department of Physiology

* - These authors contributed equally to this work

Manuscript in preparation

Abstract

Ion conduction across the cellular membrane requires the simultaneous opening of activation and inactivation gates of the K^+ channel pore. The bacterial KcsA channel has served as a powerful system to dissect the structural and dynamical changes that are related to K^+ gating. Yet, the direct observation of channel opening, i.e., of the open-conductive conformation so far remained challenging due to the high extent of C-type inactivation. Using electrophysiological and solid-state NMR experiments, we here show that negatively charged lipids reduce C-type inactivation and shift the conformational equilibrium at acidic conditions towards a more open-conductive state. Perturbation by adding membrane solvents or protein mutation confirms that the lipid-protein interface mediates this process. The increase in overall steady state open probability is accompanied by a reduction in inner-gate opening underscoring the delicate conformational coupling of inactivation and activation gate in membranes.

Introduction

The last fifteen years have seen remarkable progress in our understanding of K^+ channel structure. Since first crystal structure of the bacterial KcsA potassium channel was solved [11], many attempts have been made to characterize the KcsA gating mechanism by number of structural methods.[12,17–23] Using EPR spectroscopy, it was shown that upon activation the inner KcsA helices rotate in a counterclockwise direction away from the permeation pathway, thus opening the conduction pathway.[23,159] Electrophysiological recordings at the macroscopic level demonstrated large transient currents upon activation of KcsA by lowering the pH from 7.5 to 4.0.[12] The transient currents were characterized by a relatively fast activation time course (τ~10-20 ms) followed by a slow exponential decay with a single time constant of approximately 1.5 s. It has been proposed that this slow decay after activation is related to a C-type inactivation process.[12] By using solid-state NMR (ssNMR), it has been shown that the KcsA activation gate and the selectivity filter are structurally coupled during gating.[17,18] SsNMR studies provided a detailed description of the K^+ channel pore in a lipid environment for two distinct conformations of channel states, respectively: closed-conductive and open-inactivated (collapsed) [17,18]. More recently, we identified the pore loop as an additional functional unit involved in channel gating and lipid sensing.[131,146] However, the

direct structural characterization of the open-conductive conformation of KcsA in a lipid environment so far has remained challenging due to the very short life time of this channel state during KcsA steady state gating.[12] Instead, structural information about the open-conductive state of KcsA has been obtained by mutations which stabilize the selectivity filter in the conductive state.[12,19] Likewise, mutations at the activation gate of KcsA have been shown to greatly increase the open probability of the activation gate.[78,128] However, the selectivity filter adopts a collapsed conformation in this case even though the activation gate is only partially open. [128] The determination of the structure of the open-conductive state of a K^+ channel is, however, crucial for understanding of the molecular mechanism of K^+ channel gating. Using a combination of electrophysiological experiments and solid-state NMR spectroscopy we show in the following that the open-conductive conformation of KcsA can be stabilized in cardiolipin (CL)-rich lipid bilayer environment.

Results and Discussion

Lipid-dependent steady-state gating of KcsA. At steady state conditions KcsA exhibits a low open probability (P_O) which is associated with C-type inactivation of the channel.[12,160–162]. It has been shown previously that anionic phospholipids may stabilize open state of KcsA at steady state conditions presumably via interaction with extracellular non-annular lipid binding site[27,99]. Hence, we tested different anionic phospholipid conditions to maximize the stabilization of the open-conductive conformation without mutation of the protein.

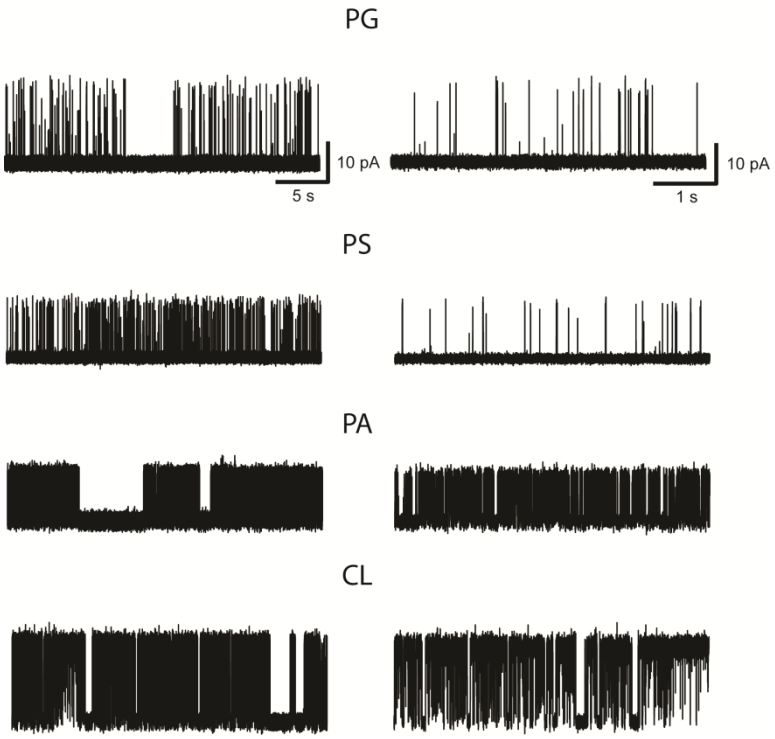

Figure 1. Representative current traces of KcsA recorded at different anionic phospholipid environments. The specific anionic phospholipid is indicated above the current traces. On the left part of the figure long 30 s traces are presented and on the right part of the figure 5 s traces are shown. All experiments were performed at +100 mV in symmetrical 150 mM KCl solution at pH = 7.0 on the *cis* side and pH 4.0 on the *trans* side. Lipid bilayers were composed of 70 % anionic phospholipid and 30 % neutral DOPC.

We recorded single channel currents of KcsA incorporated in four different types of anionic phospholipids 1,2-di-(9Z-octadecenoyl)-sn-glycero-3-phospho-(1'-rac-glycerol) (DOPG), 1,2-di-(9Z-octadecenoyl)-sn-glycero-3-phospho-L-serine (DOPS), 1,2-dioleoyl-sn-glycero-3-phosphate (DOPA) and Cardiolipin (heart, Bovine) (CL) at steady state conditions using planar lipid bilayer electrophysiology. The data indicated that anionic phospholipids (at a 7:3 ratio with neutral 1,2-di-(9Z-octadecenoyl)-sn-glycero-3-phosphocholine (DOPC)) significantly modulated the KcsA single channel properties (Fig. 1). The P_O was high in a lipid environment with more negatively charged headgroups DOPA and CL and comparably low in a lipidic environment with less negatively charged head groups, such as in DOPG and DOPS,

respectively (Fig. 2). We observed a maximal P_O in the presence of CL (P_O = 0.37 ± 0.09), which has the highest headgroup charge[163] of the anionic phospholipids tested (Fig. 2).

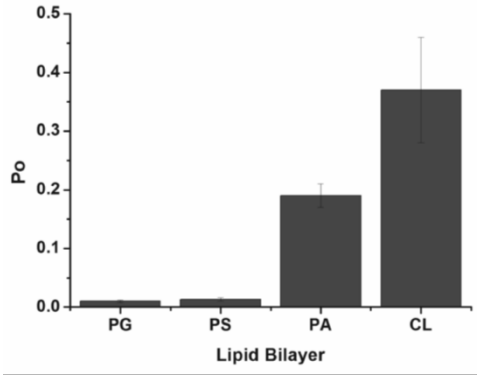

Figure 2. Open probability of KcsA in different anionic phospholipids. All experiments were performed in symmetrical 150 mM KCl solution at pH = 7.0 on the *cis* side and pH 4.0 on the *trans* side. Lipid bilayers were composed of 70 % anionic lipid and 30 % neutral DOPC. Open probability (P_O) values were calculated for entire recordings of the single channel currents conducted by KcsA, including long closed periods, and thus represent the overall P_O of KcsA potassium channels in the particular phospholipid membrane. KcsA open probability (P_O) values are given in the text as mean ± s.e.m.

Analysis of the dwell time histograms revealed that both open and closed durations are composed of multiple kinetic components, which is in good agreement with previous studies. [164,165] Under all experimentally tested phospholipid conditions, dwell-time histograms for closed durations were best fit with three exponentials corresponding to three non-conductive states of the KcsA channel (data not shown). Closed times representing mainly inactivated states at steady state conditions [164] were sensitive to changes in anionic phospholipid environment. The total mean closed time (τ_{mean}) was about 8 fold shorter in the presence of DOPA and CL in comparison to DOPG and DOPS. This effect of DOPA and CL was due to reduction of the most prevalent second closed state (τ_2,) which was predominant in the presence of DOPG and DOPS. In the presence of DOPA and CL, the second closed state was greatly reduced and the first short-lived closed state (τ_1) became the predominant one (data not shown). Taken together, the analysis of closed time distributions indicated a significant effect of the anionic phospholipids on KcsA channel C-type inactivation, which is decreasing by phospholipids with more negatively-charged headgroup such as DOPA and CL. In parallel, we observed increase in P_O in the presence of more negatively charged DOPA and CL.

The three exponential fit of dwell time histograms for open durations revealed that KcsA mean open time (τ_{mean}) in the presence of DOPA and CL was higher than in presence of DOPG and DOPS. Two factors have

contributed to this effect. First, the duration and impact of the second open state were higher in the presence of DOPA and CL, in comparison to DOPG and DOPS (τ_2). Second, in the presence of DOPA and CL, the third long-lived open state of KcsA was observed in the dwell time distributions, while in the DOPG and DOPS, the third long-lived open state was not detectable (τ_3).
Our findings suggest that the effect of anionic phospholipids on KcsA closed and opened durations depends on phospholipid headgroup charge. More negatively charged headgroups reduce the mean closed (inactivated) time of the channel and, thereby, increase its mean open time, which then results in an increase in channel P_O (Fig. 1, 2). The maximal mean open time of KcsA was observed in CL which is the most negatively charged phospholipid among the tested phospholipids.

CL stabilizes the open-conductive conformation of KcsA potassium channel. Our electrophysiological experiments suggested that CL that has the strongest effect on KcsA gating at steady state activated conditions, possibly stabilizing KcsA in an open-conductive conformation. In order to address this question, we performed two-dimensional (^{13}C,^{13}C) and (^{15}N,^{13}C) correlations experiments on KcsA in similar phospholipid environments used in our electrophysiological experiments, i.e., using the three anionic phospholipids DOPG, DOPA and CL.

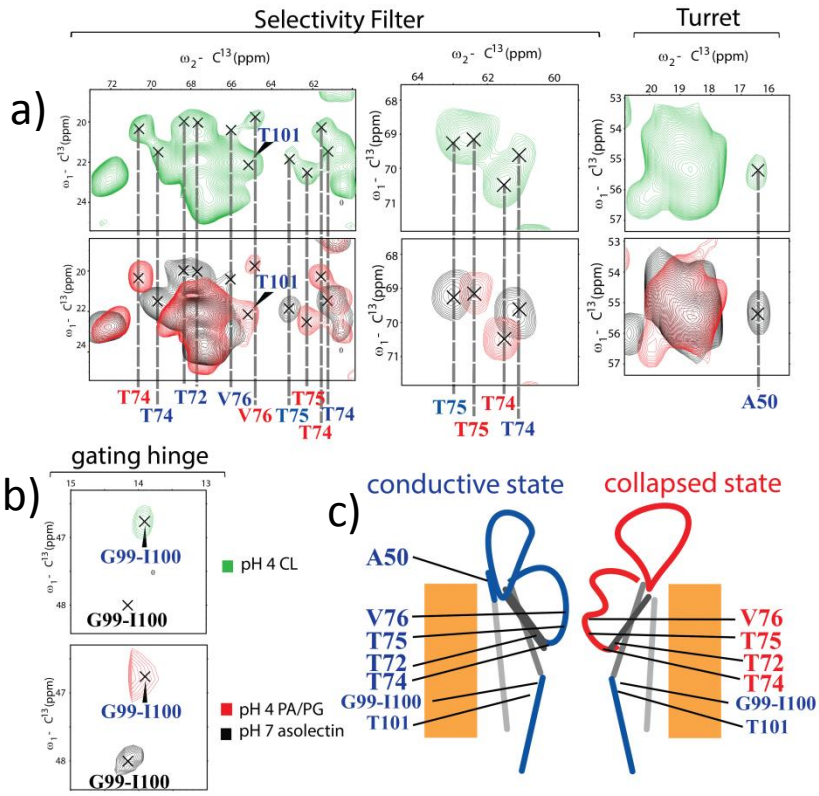

Figure 3. Open-collapsed (inactivated) and open-conductive conformations of KcsA probed by ssNMR in different anionic phospholipid environments. Cutouts are shown of ^{13}C-^{13}C correlation spectra recorded in the presence of 150 mM KCl at pH 4.0 in different anionic phospholipid environments. KcsA was reconstituted into proteoliposomes composed of DOPC/DOPG, DOPC/DOPA or DOPC/CL) at 3/7 molar ratio. –Data recorded for CL pH 4.0 are given in green. –ssNMR spectra recorded for DOPA/DOPG (pH 4.0) and for asolectin at pH 7.0 are indicated in red and black, respectively. Correlations for residues around the inactivation gate (a, left), turret (a, right) and the gating hinge (b) are displayed. Residues indicated in the spectra correspond to collapsed (red) and conductive (blue) SF conformations (see cartoon c). Experimental data were recorded at magnetic fields corresponding to 500-700 MHz ^{1}H-frequency and at an effective sample temperature of 273 K.

^{13}C-^{13}C correlation spectra recorded with short mixing time on KcsA enabled us to identify ^{13}C chemical shifts of key residues T72, T74, T75 and V76 within the KcsA selectivity filter and T101 located at the activation gate (Figure 3). In DOPG and DOPA the conformation of these residues corresponded to a collapsed (inactivated) conformation of

the KcsA selectivity filter (Fig. 3a, lower panel). In the case of CL bilayers, spectra, we observed two sets of ^{13}C-^{13}C intra-residue correlations at T72CG2-CA/CB, T74CA-CB, T74CG2-CB, T75CA-CB and T75CG2-CA compatible with the presence of both collapsed (inactivated) and conductive conformations of the selectivity filter (Fig. 3a left, upper row). The existence of both populations was also confirmed in 2D NCACX experiments (data not shown). Furthermore, our ^{13}C-^{13}C intra-residue correlation spectra clearly showed that in the presence of CL lipids KcsA can still adopt an extended TM1 α-helix (as diagnosed by Ala50 in the spectrum, Fig. 3a, right), which is involved in KcsA-lipid interactions [131]. Note that the spectra using longer ^{13}C,^{13}C mixing times exhibited sequential G99-I100 correlations for all lipid preparations that were compatible with an open activation gate (Fig. 3b).

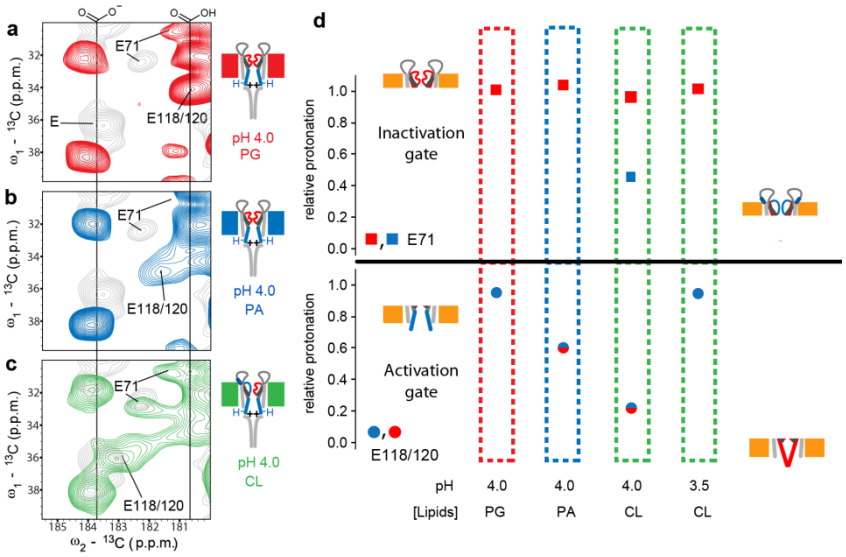

Figure 4. Protonation of glutamate side-chain carboxyls depends on pH and lipid composition. (a–c) Regions from (^{13}C,^{13}C) correlation spectra showing glutamate Cγ-Cδ crosspeaks in different lipid compositions. Individual cartoons with (a) red PG, (b) blue PA and (c) green CL phospholipids indicate channel states as defined in Figure 3c. Negative charges and protons illustrate the protonation states of Glu118 and Glu120 at the helix bundle crossing. Positive charges are added to indicate electrostatics at the helix bundle crossing. (d) Relative protonation of E71 (squares) and E118/120 (circles) computed for different lipid compositions. For each condition, integrals of crosspeaks corresponding to the respective protonated and deprotonated glutamate Cγ-Cδ crosspeaks were normalized to their sum. Relative protonation is, therefore, represented by the fractions of protonated Cγ-Cδ signal. Drawings indicate

gating states. Protonation of E118/120 correlates with activation-gate opening, whereas inactivation-gate closure involves an increased protonation of E71.

Next we investigated the relative protonation level of glutamate residues located at both channel gates as a function of phospholipid type and pH. As we have shown before [17], the isotropic chemical shift of glutamate δ carbon atoms that is correlated with the side-chain protonation state[166] provides a sensitive means to probe residue-specific protonation in membrane-embedded KcsA variants. For the inactivation gate, protonation levels seen for E71 corroborated our previous analysis on the chimeric KcsA-Kv1.3 channel that differs from the WT KcsA in 11 amino acids in the turret region[17]. In both cases, the collapsed state of the SF involves protonation of E71. In the presence of a second conductive population at CL (pH 4), we observed additional correlations consistent with a reduction in E71 protonation (Figure 4d, top row) in qualitative agreement with our earlier work indicative of a deprotonation in the case of a conductive SF.
Furthermore, lipid induced changes became apparent at the activation gate (Figure 4d, bottom panel). In PG lipid bilayers, the protonation of glutamate residues close to the activation gate were similar to the protonation levels seen for KcsA-Kv1.3. In more negatively charged PA and CL lipids, we observed a reduction in protonation level as diagonised by the ssNMR signal intensity at protonated and non-protonated chemical shifts conditions (see Figure 4, caption). These results suggested that the extent of activation gate opening is reduced for PA and CL phospholipids
Crystal structures of the constitutively open KcsA mutants have suggested that the KcsA activation gate can display various degrees of activation gate opening[128]. In line with recent EPR data[167,168], our results suggest that the transition from neutral to acidic pH is accompanied by a gradual closing of the inactivation gate and an increasing opening of the activation gate. At pH 4 and CL, two channel states with a partially open activation gate and open and closed inactivation gates become visible in our ssNMR data. The relative populations of both states can be estimated by comparing signal intensities for open-conductive and open-inactivated state leading to a relative distribution of conductive and closed inactivation gate of 40 : 60. These values are in remarkable agreement to Po of 37 % (Fig 2) measured for KcsA in the CL lipid bilayer.

Under more acidic conditions, pH 3.5, we observe the activation gate of KcsA reconstituted in CL to be fully open. At the same time, we

observed a reduced intensity for correlations indicative of the conductive SF conformation (see Figure 3) and E71 reprotonates corresponding to an collapse filter (see Figure 4).

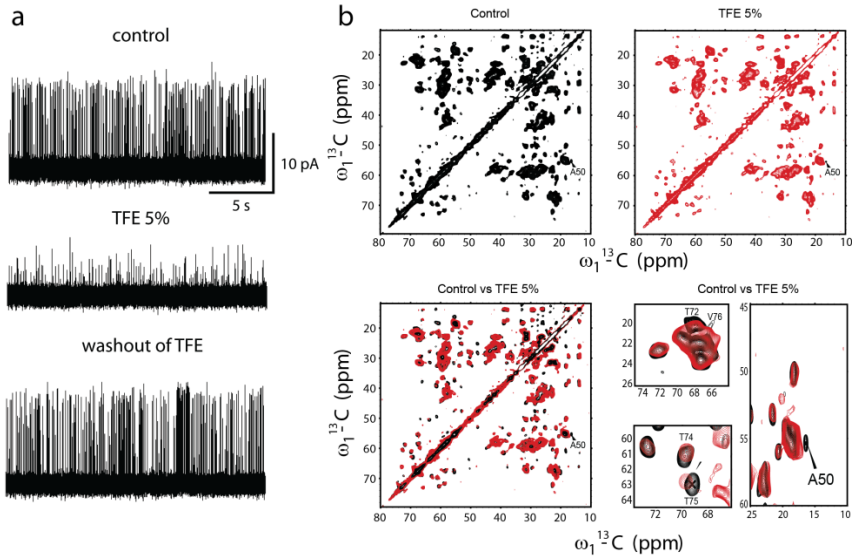

Figure 5. Influence of TFE on KcsA structure and function. (a) - Influence of TFE on KcsA single channel properties. Experiments were performed at +100 mV in symmetrical 150 mM KCl solution at pH = 7.0 on the *cis* side and pH 4.0 on the *trans* side. Lipid bilayers were composed of DOPC and DOPG at 7/3 molar ratio. TFE was applied from *cis* side. (b) - Influence of TFE on the KcsA structure in membranes probed by ssNMR. Control - 50 mM K^+ , asolectin, pH 7; TFE 5% - 150 mM K^+, DOPC/DOPG=3/7 (molar), pH 7. C-C 2D PDSD, 30 ms mixing time, 12 kHz MAS, 273 K, 500 MHz ^{1}H frequency.

Modification of KcsA-lipid interaction. Next we conducted a series of experiments to dissect the atomic interactions that may explain the influence of the lipid type on channel gating. Firstly we utilized TFE as lipid protein dissociation agent at concentrations which keep the channel structure largely intact. In our electrophysiological experiments performed in planar lipid bilayers, the KcsA open probability (P_O) and single channel conductance were reduced upon application of 5% TFE (Fig. 5a) at the extracellular part of the channel. After removal of TFE from the solution by the perfusion KcsA single channel properties were recovered (Fig. 5a). SsNMR experiments conducted on KcsA reconstituted into proteoliposomes at addition of 5 % TFE confirmed that the channel structure is largely intact (Fig. 5b). A more detailed examination revealed that residues located close to membrane lipid

headgroups at the extracellular end of TM1, e.g. Ala 50 however changed conformation (Fig. 5b).

These experiments suggest that the lipid-protein interface around the turret region is critically involved in stabilizing the channel structure. Indeed, a point mutation at residue R52 (KcsA-R52A) drastically reduced Po KcsA at high CL lipid bilayer (Fig. 6). These results are in good agreement with our previous work where we showed the role R52 in KcsA lipid interaction. [131]

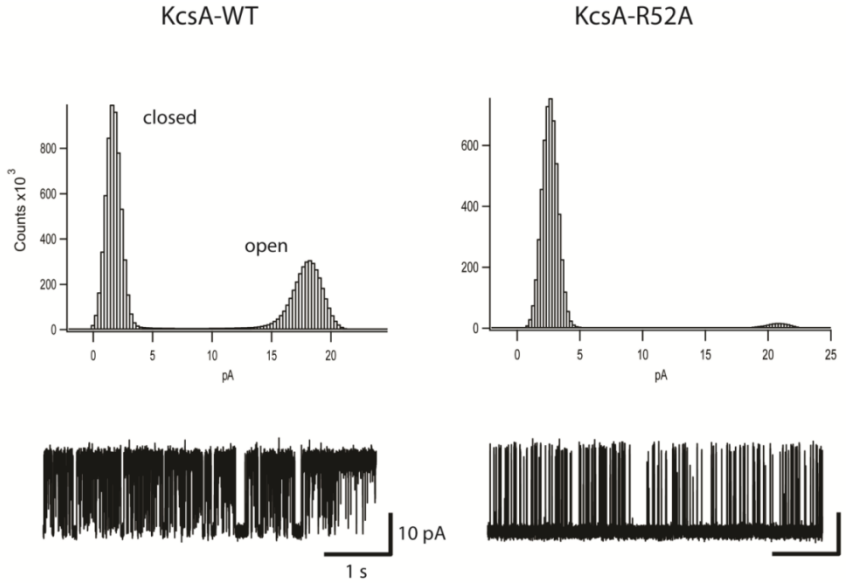

Figure 6. Representative current traces and all-point histograms of KcsA-WT and KcsA-R52A recorded in planar lipid bilayer with high content of CL. The experiments were performed at +100 mV in symmetrical 150 mM KCl solution at pH = 7.0 in cis side and pH 4.0 in trans side. Lipid bilayer was composed from DOPC and CL at 3/7 molar ratio.

Conclusions

Using electrophysiological and solid-state NMR experiments, we have shown that negatively charged lipids reduce C-type inactivation and shift the conformational equilibrium at acidic conditions towards a more open-conductive state. According to our electrophysiological experiments, cardiolipin is most effective among the lipid investigated in stabilizing the open conformation (Tau open : 11 ms, Tau closed : 16 ms). Interestingly, these time scales are one to two orders of magnitude shorter that structural transitions deduced from NMR studies on KcsA

variants in (DDM) micelles[127,169]. Thus, the presence of the lipid bilayer strongly influences the kinetic of the channel and care must be exercised when comparing conformational exchange rates obtained in micellar membrane protein preparations to the case of the lipid bilayer.

Our ssNMR analysis confirmed our electrophysiological findings that CL enhances the populations of open channel conformations at pH 4. Perturbations by adding membrane solvents or protein mutation confirm that the lipid-protein interface mediates this process. In detail we monitored protein segments that are critical for the transition from the closed-conductive to the open-inactivate state, i.e., activation and inactivation gate [17,18] as well as the turret region that is a sensitive reporter for the functional state of the inactivation gate[131]. In our analysis we studied backbone conformations via chemical-shift variations and investigated the relative protonation level of glutamate residues that are located in close vicinity to both gates.

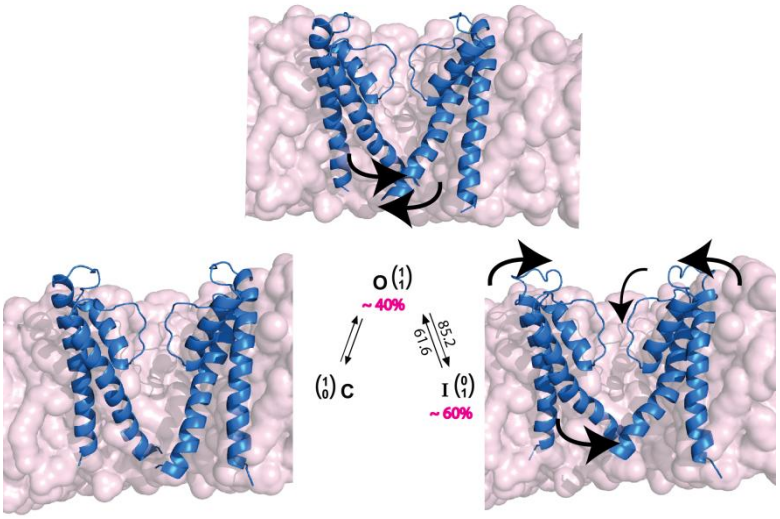

Figure 7. Structural models of gating states of KcsA potassium channel in CL lipid bilayer calculated with Crystallography & NMR System (CNS). Populations of open-collapsed and open-conductive conformations of KcsA were calculated using signal to noise analysis applied for ssNMR spectra recorded for KcsA in CL proteoliposomes. Transition rate constants between open-collapsed and open-conductive states were calculated from electrophysiological experiments conducted on KcsA in CL lipid bilayer (*see table 1*). Transition rate constants are expressed in s^{-1}.

Taken together, our studies suggest a structural and kinetic model that explains both our electrophysiological and ssNMR data (Fig. 7). Here, the transitions rates between the 2 principal gating states are described by conformational changes both in pore region (including inactivation gate and turret) and activation gate that share essential features with previous crystallographic and spectroscopic work. In detail however, the degree of opening and closing of both gates is determined by the combined influence of protein sequence, lipid environment and small molecules such as water molecules (see chapter 4) or potassium. Together, they control the delicate conformational coupling of inactivation and activation gate in membranes in each state of the potassium channel gating cycle.

Methods

Sample preparation. KcsA was expressed in M15 *E.coli* cells and purified using Ni^{2+}-affinity chromatography. For ssNMR experiments, KcsA was uniformly (^{13}C,^{15}N) labeled. An unlabeled KcsA was used for the single channel measurements. After purification, KcsA was reconstituted into proteoliposomes composed of 3 to 7 molar ratios of DOPC:DOPG, DOPC:DOPS, DOPC:DOPA, and DOPC:CL. Lipids were solubilized in reconstitution buffer (150 mM KCl, 10 mM HEPES, pH 7.4) and KcsA was added to the phospholipid mixture to give a protein/lipid mass ratio of 1:1000 for single channel measurements and a protein/lipid molar ratio of 1:100 for samples used in ssNMR experiments. Proteoliposomes were formed upon detergent removal by addition of Bio-Beads (Merck, Germany). KcsA proteoliposomes for the planar lipid bilayer experiments were split into 250 µl aliquots, flash frozen via liquid N_2 and stored at -80 ºC until usage. Proteoliposomes for ssNMR experiments were centrifuged at 100,000 g at 4 ºC and resuspended in sample buffer (150 mM KCl, 10 mM succinic acid, 0.01 % sodium azide, pH 4.0) and centrifuged again. Pelleted proteoliposomes were packed in 3.2 mm rotor and kept at 4 ºC until usage.

Planar lipid bilayer electrophysiology. Single channel recordings of KcsA were performed on planar lipid bilayer setup (*Compact, Ionovation GmbH*). Lipid bilayers were formed by painting the lipids dissolved in n-decan over a 200 µm hole that separated two chambers (*cis* and *trans*). Initially, the *trans* chamber contained 20 mM KCl, the *cis* chamber 250 mM KCl, both of which were buffered to pH 4 with 10 mM succinic acid. KcsA proteoliposomes (1-5 µL) were added to the

cis chamber of the planar bilayer system with a micropipette. After channel insertion, recording conditions were established by perfusion to symmetrical conditions. The *cis* side contained 150 mM KCl and 10 mM HEPES, pH 7.0, and the *trans* side contained 150 mM KCl and 10 mM succinic acid, pH 4.0. All measurements were performed at room temperature. Data are sampled at 10 kHz and filtered at 1 kHz. Reported data are a result of statistical analysis of at least 6 independent experiments. The kinetic analysis was done using the QuB software for single channel analysis (*www.qub.buffalo.edu*). Single channel currents were first idealized into noise free open and close transitions using a half-amplitude threshold algorithm. Closed and open intervals were compiled into dwell time histograms with logarithmic abscissa and square root ordinate [170] and were fitted by sums of exponentials according following equations:

$$f(t) = \sum_{i=1}^{n} a_i \lambda_i e^{-\lambda_i t} \qquad \sum_{i=1}^{n} a_i = 1$$

where and $\boldsymbol{\lambda_i}$ is the reciprocal of the time constant of the i^{th} component; $\boldsymbol{n}$ - number of exponential components; $\boldsymbol{a_i}$ is the fractional area occupied by the i^{th} component; $\boldsymbol{t}$ is decay constant

Solid-state NMR spectroscopy. SsNMR experiments were conducted at 500-700 MHz ^{1}H resonance frequency on NMR spectrometers (Bruker Biospin, Germany) equipped with 3.2 mm triple resonance (^{1}H, ^{13}C, ^{15}N) MAS probe heads. All experiments were carried out at an effective sample temperature of 273 K. MAS frequencies were set to 12, 15 and 11.4 kHz for ^{13}C-^{13}C PDSD experiments with 30 ms mixing time, ^{13}C-^{13}C PDSD with 150 ms mixing time and NCACX experiments, respectively. NCACX spectra were acquired by using ^{13}C-^{13}C magnetization transfer via 30 ms PARIS ^{13}C-^{13}C mixing step.[133] Data acquisition and analysis were performed with Topspin 3.1 (Bruker Biospin, USA).

Chapter 6

NMR-based Structural Biology enhanced by Dynamic Nuclear Polarization at high magnetic field

Eline J. Koers[*‡], Elwin A. W. van der Cruijsen[*‡], Melanie Rosay[§], Markus Weingarth[*], Alexander Prokofyev[*,†], Claire Sauvée[+], Olivier Ouari[+], Olaf Pongs[†], Paul Tordo[+], Werner E. Maas[§], Marc Baldus[*¶]

*Bijvoet Center for Biomolecular Research, Utrecht University
§Bruker BioSpin Corporation,
†Saarland University, Faculty of Medicine, Department of Physiology
+Aix-Marseille Université, CNRS

Under review

Abstract

Dynamic Nuclear Polarization (DNP) has become a powerful method to enhance spectroscopic sensitivity in the context of Magnetic Resonance Imaging (MRI) and Nuclear Magnetic Resonance (NMR) spectroscopy. We show that the combination of high field DNP (800 MHz/527 GHz) with Magic Angle Spinning (MAS) solid-state NMR can significantly enhance spectral resolution and allows exploitation of the paramagnetic relaxation properties of DNP polarizing agents as direct structural probes. Applied to a membrane-embedded K^+ channel, this approach allowed us to refine the membrane-embedded channel structure and revealed conformational substates that are present during two different stages of the channel gating cycle. High-field DNP thus offers atomic insight into the role of molecular plasticity during the course of biomolecular function in a complex cellular environment.

Introduction

Dynamic nuclear polarization (DNP, Ref.[41]), a process in which nuclear spins are polarized via microwave irradiation of a nearby electron spin, is finding widespread applications in NMR spectroscopy[171,172] and Magnetic Resonance Imaging (MRI)[173,174]. In solid-state NMR (ssNMR), the combined application of low-temperature (LT)-DNP, Magic Angle Spinning (MAS, Ref[34]) and the use of exogenous paramagnetic polarizing agents has been employed as a signal enhancement method with increasing applications in material[43] and life sciences[44]. For example, LT-DNP under MAS has been used to study membrane-associated peptides[45,46] as well as intermediate[47] and ligand-bound membrane protein states[48–50]. In addition, DNP-MAS has been successfully applied on cellular preparations[51–53] and can be used to examine large macromolecular complexes[54]. On the other hand, paramagnetic agents are widely employed to enhance contrast and resolution in MRI applications[175]. The same principles have made paramagnetic relaxation effects (PREs) invaluable tools to refine molecular structures in biomolecular applications of solution[176,177] and, more recently, solid-state NMR[178,179]. In the latter case, elegant approaches have also been proposed to reduce spectroscopic repetition rates[180] and it is well known that the modulation of longitudinal relaxation rates by PREs favorably influences spectroscopic aspects of low temperature (LT)-DNP studies.

While progress has been made in building DNP systems at high fields[181,182], most commercially available DNP NMR spectrometers have been operating at a 1H resonance frequency of 400 MHz (and 263 GHz DNP) where spectroscopic studies, at least in part, can be hampered by the comparatively low spectral resolution. Here, we investigate the use of MAS DNP instrumentation operating at 800 MHz/527 GHz for biomolecular solid-state NMR. Since ssNMR has become a powerful method for applications in membrane- and cell embedded molecular systems, we utilized in our studies uniformly (^{13}C,^{15}N) and ($^{2}H^{13}C^{15}N$) labeled variants of the membrane embedded potassium channel KcsA, for which crystallographic information[9,183] as well as ssNMR data are available[18,131,184]. As in the general class of K+ channels, KcsA comprises two coupled gates that are located at either end of the channel pore and that are called the activation and inactivation (a.k.a. selectivity filter, SF) gate. Channel inactivation leads to a closing of the inactivation gate and an opening of the activation gate[17,77,128]. Starting with the closed conductive channel state that has been well characterized by X-ray and ssNMR, we examined the influence of transversal PREs and conformational heterogeneity upon LT-DNP spectra obtained at 800 MHz/527 GHz at the residue-specific level. Our NMR studies were assisted by single channel measurements and MD calculations. Furthermore we compared spectral resolution and DNP enhancements to results obtained at 400 MHz, providing insight into site-specific origin for ssNMR line broadening and signal enhancement under LT-DNP conditions. For many ion channel residues, we observed an increase in spectral resolution. These findings provided the basis to employ high-field DNP to examine how variations in ion channel structure correlate to the channel state before and after inactivation.

Materials and Methods

Sample preparation. We prepared proteoliposomal samples containing uniformly (^{13}C,^{15}N) labelled KcsA in the closed conductive and open inactivated state as described before[18,131]. As in ref[185], ($^{2}H^{13}C^{15}N$) labeled KcsA was expressed and back exchanged and reconstituted in asolectin. For DNP-based ssNMR experiments, we washed liposomal KcsA samples with 50 µL DNP solution containing TOTAPOL (5 mM as well as 10 mM) or AMUPol (25 mM) in 1:2:2 (v/v/v) glycerol-d8, D2O, and H2O. Samples were subsequently centrifuged at 125,000 g for approximately 30 min followed by removal of the supernatant. This procedure was done twice. The remaining pellet was then transferred

from the Eppendorf tube to a 3.2 mm sapphire rotor by means of a funnel and centrifugation for 5-10 seconds in a bench top centrifuge.

Solid-state NMR and DNP experiments. ssNMR and DNP experiments were conducted using 3.2 mm triple-resonance (1H,13C,15N) magic-angle-spinning (MAS) probe heads at static magnetic fields ranging from 9.4 to 18.8 T corresponding to proton/electron resonance frequencies of 400 MHz/ 263 GHz[186], 700 MHz or 800 MHz/ 527 GHz (Bruker BioSpin).
Data were recorded at 100 K (LT) and at 273 K (referred as ambient temperature, AT) employing MAS rates between 8 and 15 kHz. Pulse schemes reflected standard homonuclear proton-driven spin diffusion (PDSD) and double-quantum filtered ($^{13}C,^{13}C$) using SPC5 recoupling[187]. NCA experiments typically utilized SPECIFIC-CP transfer[39] (see SI for further details on the experimental parameters).

Molecular dynamics simulations. Atomistic MD simulations were carried out using the GROMACS simulations package version 4.5.3 with the GROMOS53a6 forcefield[87]. The starting structure was derived from crystal structure 3EFF, truncated to residues 22 to 115. The channel was embedded in a POPG bilayer in an aqueous solution of 150 mM KCl. All simulations were carried out under constant pressure. The chemical shift analysis presented in Fig. 3 is based on a 10 ns simulation, while chemical shifts where predicted every 200 ps using SPARTA+[89].

Single Channel Measurements. Single channel recordings of KcsA were performed on a planar lipid bilayer setup (Compact, Ionovation GmbH). Lipid bilayers were formed by painting the lipids dissolved in n-decane over a 200 μm hole in a Teflon-septum that separated two chambers (cis and trans). KcsA proteoliposomes (1−5 μL) were added to the cis chamber. Single channel currents were recorded in symmetrical 150 mM KCl solution. The cis side was buffered to pH 7.0 by 10 mM HEPES and trans side was buffered to pH 4.0 by 10 mM succinic acid. All measurements were performed at room temperature. Data were sampled at 10 kHz and filtered at 1 kHz.

Results and Discussion

Paramagnetic relaxation effects. In order to probe paramagnetic relaxation effects in our DNP samples, we firstly studied membrane-

embedded U-(^{13}C,^{15}N) KcsA at AT before (Figure 1a, black) and after addition of 5 mM TOTAPOL and 20% glycerol (Figure 1a, green). Note that this situation (employing water-soluble radicals) is different from using covalently attached radicals (see, e.g., Ref. [188]). The addition of the biradical left large parts of the spectra unaffected (i.e. no reduction of signal intensity and chemical shift changes) with the exception of, for example, backbone resonances of Pro 63, Thr 61 or Thr 85 or side-chain cross peaks of Val 84 (Figure 1a).

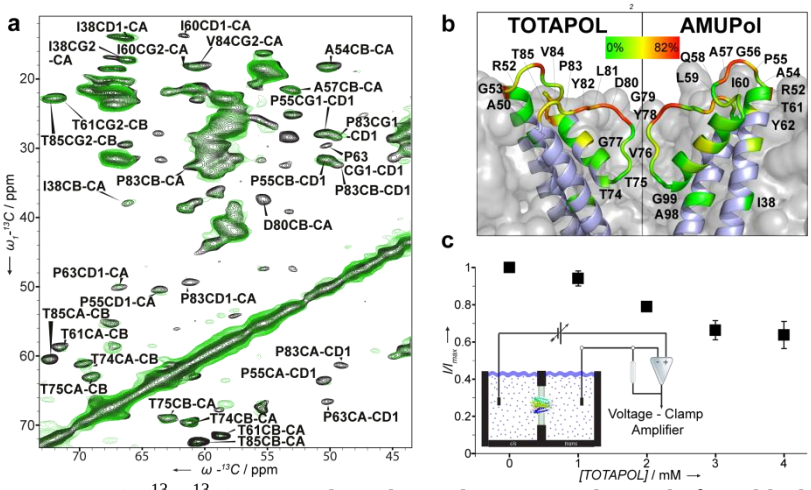

Figure 1. a) (^{13}C,^{13}C) PDSD data obtained at AT conditions before (black) or after addition of 5 mM TOTAPOL (green). In b), the residue-specific signal attenuation due to the addition of 5 mM TOTAPOL and 25 mM AMUPol is shown. The scale bar represents signal scaling after addition of biradical ranging from 0 (green, not attenuated) to 82% (red, attenuated). c) Single channel current of KcsA in planar lipid bilayers at increasing levels of TOTAPOL

PRE-induced signal modulations were exclusively found in the solvent-exposed regions (Supporting Table I) as can be deduced from the attenuation plotted on a three-dimensional membrane embedded model of KcsA in the closed conductive state (Figure 1b, left). Within the selectivity filter (SF, residues 74-79) that represents the inactivation gate[18], we observed a strong decrease in PREs when moving from the water-exposed entry (Gly 79) towards the center of the channel (Thr 74). For many solvent-exposed residues signal intensities were reduced by more than a factor 5 (Figure 1b, left, red). Variations of solvent PREs[189] on the protein-solvent interface could be explained by similar mechanisms as found for the radical TEMPOL in earlier solution state

NMR experiments[190–192]. Hence, our results suggest that PREs at AT are restricted to a few Angstrom below the solvent exposed channel parts caused by radicals residing in the solvent or close to the solvent-exposed protein surface and not in the membrane. Additional experiments (data not shown) suggested that the addition of glycerol does not lead to additional line broadening.

Since strong PREs were found at the extracellular channel pore entrance, we further investigated the possibility of TOTAPOL binding to KcsA. Electrophysiological experiments (Fig. 1c) suggest that concentrations as low as 4 mM TOTAPOL affect single channel properties of KcsA by reducing amplitudes of the single channel current by as much as 40% at which point a plateau is reached, excluding the possibility of channel blockage by the radical. Instead, these results suggest, together with the lack of chemical shift changes (Fig. 1a), a partial occlusion of the channel entry with increasing concentrations of the biradical without perturbing the structure of the channel itself. We note that weak transient binding cannot be excluded.

Next we conducted experiments using 25 mM AMUPol which revealed a similar overall relaxation profile (Figure 1b, right), albeit with slightly weaker effects at the channel entry (supporting table 2 and Figure S1). These results suggest that PREs at AT are slightly larger for KcsA samples prepared with 5 mM TOTAPOL than in samples containing 25 mM AMUPol. Taking into account the five times lower TOTAPOL concentration, this observation likely reflects the influence of different molecular sizes of the two biradicals considered. Due to the additional hydrophilic tail of AMUPol and the size of the molecule, the radical center of AMUPol would be, on average, further distant to the protein - lipid surface than in the case of the more hydrophobic TOTAPOL.

Intrinsic line width at low temperature. Our previous analysis identifies PREs as an important source of T2 relaxation that provides direct insight into the solvent-exposed molecular region (Figure 1b). In addition, molecular motion should give rise to structural disorder at lower temperatures. Such effects have, for example, been exploited in the context of studying peptide and protein folding by ssNMR[193,194]. More recently, the dynamics of globular proteins[48] and the impact of solvent dynamics for LT ssNMR experiments have been investigated[195]. In the following, we hence considered contributions of both PREs and structural disorder for LT-DNP data obtained at 800 MHz/527 GHz under variable biradical concentration and compared our results to experiments at 400 MHz DNP conditions.

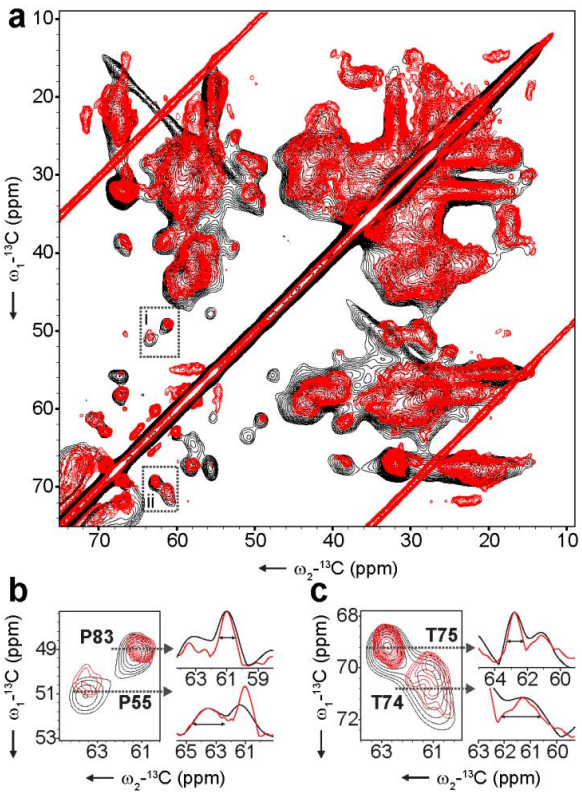

Figure 2. 400 MHz and 800 MHz. DNP 2D PDSD spectra recorded at 400 MHz (black) and 800 MHz (red) are overlayed. Proline CD1-CA (b) and Threonine CB-CA (c) regions are shown on the right, together with 1D projections of the CA peaks in the direct dimension. Note, 400 MHz DNP 2D PDSD spectrum contains a folded in sideband

Fig. 2 compares results of a standard 2D $^{13}C,^{13}C$ PDSD experiment obtained on U[$^{13}C,^{15}N$] KcsA in asolectin bilayers at 400 MHz (black) and 800 MHz (red) under DNP conditions using TOTAPOL as polarizing agent. At the latter field strength, we also compared data for a TOTAPOL concentration of 5 mM (Figure 3, black) and 10 mM (Fig. 3, orange) and focused on residues around the selectivity filter. In order to obtain complementary insight into the role of residue-specific channel motion we conducted molecular dynamics (MD) simulations and computed the chemical-shift distribution (Figure 3, histograms) from our MD trajectories as shown before[193,196]. We observed a remarkable correlation between line widths determined experimentally and predicted from MD runs for the residues Gly 77, Thr 74 and Thr 75 (Figure 3, see also supporting table 3). Note that this analysis suggests

that structural disorder in the selectivity filter is restricted to Thr 74 that exhibits a significantly larger line width than Thr 75 and Gly 77 (vide infra) and only mildly improves in resolution when moving from 400 to 800 MHz (Figure 2c).
The other two residues investigated, i.e., Thr 85 and Gly 79, exhibit greater line width than predicted by the MD simulation data (Figure 3). These residues where among the most attenuated ones at AT (Figure 1) suggesting that broadening is mainly due to paramagnetic relaxation. This view is further supported by investigating the effect of increasing the concentration of TOTAPOL from 5 to 10 mM. In this case, broadening for Thr 85 and G79 further strongly increases while PREs for Thr 74, Thr 75 and Gly 77 remained limited (Figure 3). Notably, residues that seem to be dominated by PREs (Pro 55, Pro 83) still exhibit an improvement in spectral resolution at higher field (Figure 2b).

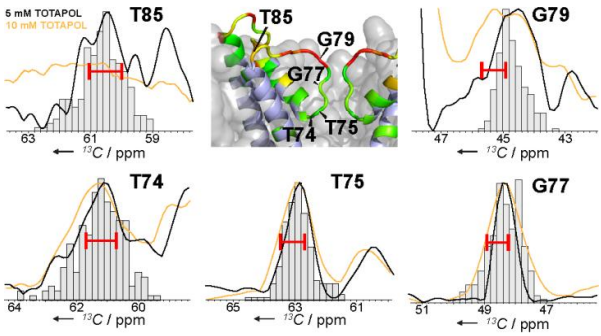

Figure 3. Projections of resolved peaks stemming from selectivity filter residues. 1D projections using 5 mM TOTAPOL (black) and 10 mM TOTAPOL (orange) are overlayed with the chemical shift distribution predicted by MD (see experimental details). For reference, the line width measured at 700 MHz AT, without addition of TOTAPOL is given by red bars. Results from G79, G77, T74 and T75 were taken from an NCA spectrum and T85 was determined from a (^{13}C,^{13}C) PDSD spectrum. The inset structure is a zoom-in from Fig. 1b (solvent PREs at AT). Line shape fitting parameters can be found in Supporting Table 3.

Taken together our analysis confirms that line broadening effects at low temperatures can be explained by two phenomena: conformational heterogeneity and paramagnetic relaxation effects.

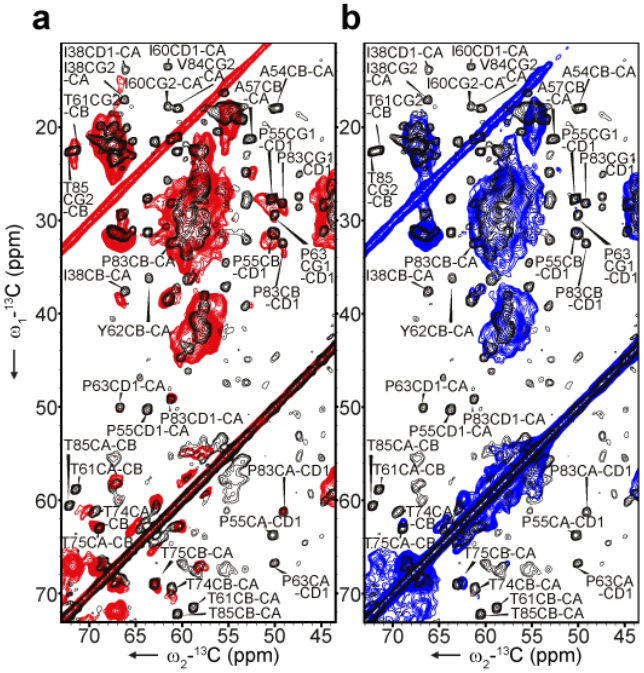

Figure 4. Overlay of ^{13}C-^{13}C PDSD at 700 MHz, 273 K without radicals (black) and 800 MHz LT, 5 mM TOTAPOL with (a, red) and without microwaves (b, blue).

Comparison to high field data at AT. To further verify our conclusions regarding the intrinsic line width under 800 MHz DNP conditions, we compared our LT-DNP data (Figures 4 and 5, red) to results obtained at AT conditions in the absence of the two biradicals of interest (Figure 4 and 5, black). The latter data were obtained at higher field strength (700 MHz). Using previously assigned large fractions of KcsA variants[131,184], we analyzed 2D PDSD experiments at LT (Figure 4) as well LT NCA data under DNP conditions using 5 mM TOTAPOL (Figure 5a) and 25 mM AMUPol (Figure 5b). In both sets of experiments we observed PRE modulated signal intensities for residues located at the channel-water interface. For example, Thr 61 and Thr 85 exhibited weaker signal intensities than Thr 74 and Thr 75. Note that these findings were made irrespective of the biradical type. We note that additional correlations in the region 70 to 65 ppm stem from co-purified lipids which are mobile under AT conditions[83].

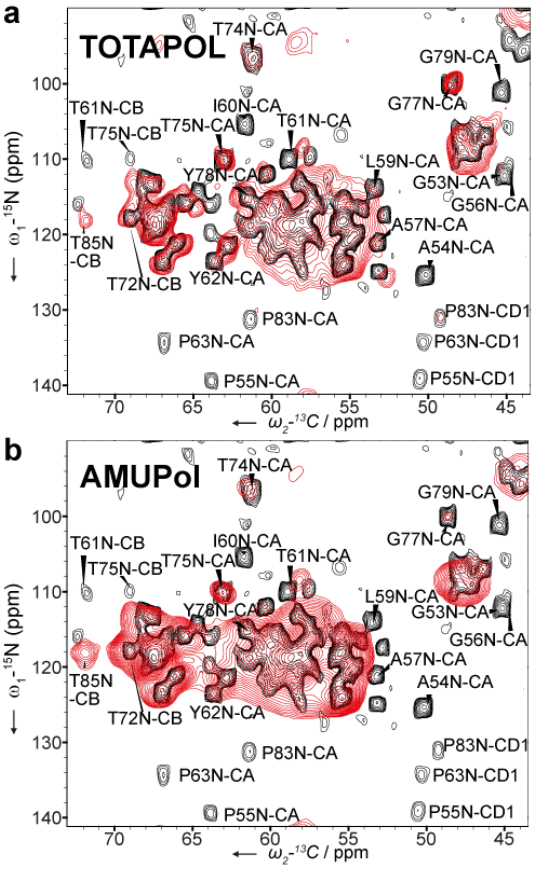

Figure 5. Comparison of KcsA data obtained at AT and LT-DNP conditions. The results of 2D NCA experiments obtained at 700 MHz at AT conditions and without biradical (black) are compared to data acquired under DNP conditions (red) at 800 MHz/527 GHz using 5 mM TOTAPOL (a) or 25 mM AMUPol (b).

On the other hand, the apparent line width of many residues seen at LT-DNP in the presence (Figure 4a) or absence (Figure 4b, blue) of microwave irradiation compared favorably to data obtained at high temperatures. For example, LT-DNP correlations seen for Thr 74 or Pro 83 are virtually identical to data seen at AT 700 MHz conditions. In the case of Gly 79, we previously had detected increased channel dynamics[152]. The observed weak intensity at LT conditions can hence be explained by a combination of increased dynamics (vide infra) and PREs.

Overall and residue specific enhancements. Firstly, we determined global enhancement factors at 800 MHz/527 GHz conditions in one-dimensional ^{13}C CP experiments for both pronotated and deuterated variants of membrane-embedded KcsA. We observed factors of 2.8 and up to 8.3 for uniformly labeled [^{1}H,^{13}C,^{15}N] KcsA with 5 mM TOTAPOL and 25 mM AMUPol, respectively. Similar values were obtained for one-dimensional ^{15}N CP experiments. In the case of AMUPOL, enhancement factors had dropped to 5 when remeasured after 5 months storage at 193 K (Figure 6d, green colored bars). Compared to equivalent experiments conducted at 400 MHz, the 5 mM TOTAPOL sample hence showed an approximately four-fold decrease in DNP enhancement at 800 MHz/527 GHz. When comparing LT-DNP ssNMR data (Figure 5a,b) to AT ssNMR experiments (Figure 5a,b) on [^{1}H,^{13}C,^{15}N] KcsA, the addition of 25 mM AMUPol resulted in a sizable increase in signal to noise per hour by a factor of 6.9 (SI Fig. S2). Deuteration and ^{1}H back exchange for [^{2}H,^{13}C,^{15}N] KcsA further increased DNP enhancements from 8.3 to 13.2 (Figure 6d) which is in line with earlier work[197,198].

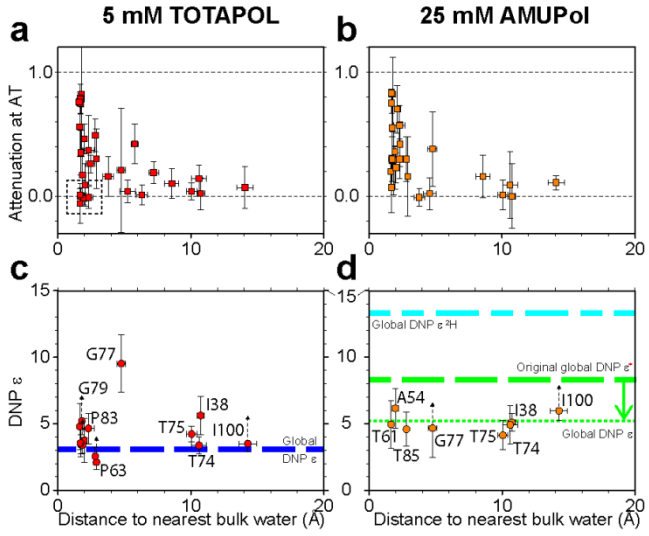

Figure 6. Residue specific solvent PRE attenuation at AT (a,b) and DNP residue specific and global enhancements (c,d) as a function of the distance to the nearest bulk water. Dashed arrows are shown for error bars lacking upper boundaries. The boxed area in (a) contains residues Tyr 45, Ala 50, Glu 51, Arg 52, Trp 87 and Tyr 78. All, but Tyr 78 are part of the protein-lipid-water interface.

Clearly, the enhancements seen at 800 MHz are lower than for data obtained at 400 MHz conditions. However, DNP enhancement factors reported in the literature[45,46,49,50,199–201] for membrane proteins at 400 MHz and 100 K vary considerably in range from 8-32. These observations point to an important influence of the details of the sample preparation upon the LT-DNP performance.

The favorable spectral resolution at 800 MHz and the observed signal modulation due to PREs and motional effects prompted us to determine residue-specific DNP enhancements at 800 MHz/ 527GHz. In Figure 6, this analysis is presented for our [^{1}H,^{13}C,^{15}N] KcsA samples. To visualize the effect of the distance of the AMUPol or TOTAPOL radical to the nearest position possible to the channel, we plotted PREs obtained at AT and residue-specific DNP enhancements against the distance to the nearest bulk water taken from the MD simulations (Fig 6a-d). As expected from the Solomon-Bloembergen equations[202,203], residues located closer to the surface exhibited stronger signal attenuation. Especially at the lower biradical concentration, residue-specific variations are however, substantial and most likely relate to local shielding effects by lipid-protein interactions for residues such as Tyr 45, Ala 50-Arg 52 or Trp 87 (dashed box in Fig. 6a) which are all located at the protein-lipid interface (see. Fig. 1b, left). Moreover, a uniform biradical distribution may only be established a concentrations higher than 5 mM TOTAPOL.

Both effects may also explain the larger fluctuations in residue-specific DNP enhancements (Figure 6c,d) with maximum enhancements seen for Gly 77, Ile 38, Thr 75 and Pro 83 in the 5 mM TOTAPOL sample. The most dramatic difference is found for Gly 77. Both in the 5 mM TOTAPOL sample and the ^{2}H^{13}C^{15}N 25 mM AMUPol sample (Figure 7) this residue exhibits the highest residue specific enhancement relative to the global values seen in 1D data (Fig 6c, table S4). We note that for the deuterated case, spectra without microwave irradiation suffered from limited signal to noise and an analysis such as shown in Figure 6 was restricted to a smaller number of protein residues around the channel pore segment (see supporting table 4). In this protein region, variations in DNP enhancements are small compared to the PREs seen at AT which would be consistent with the dominant influence of spin diffusion[204].

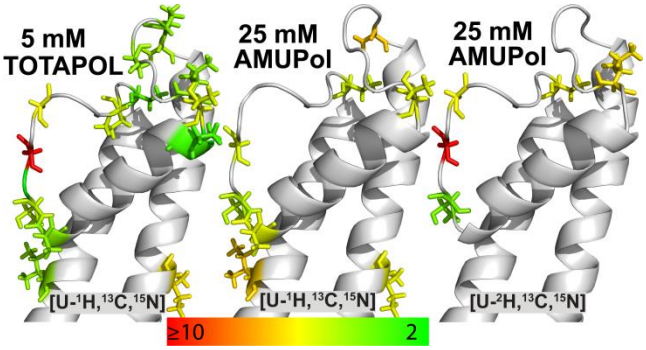

Figure 7. Residue-specific LT-DNP enhancements in a close up region around the selectivity filter with (left) TOTAPOL, (middel) AMUPol and (right) AMUPol with proton back-exchanged [U-2H,13C,15N]. Scale bar refers to relative DNP enhancements ranging from 2 (green) to ≥10 (red).

Strong variations were only observed for Gly 77 that is not only located at the center of the selectivity filter and thereby distant from both the solvent or cavity water but is also surrounded by nearby potassium ions in crystal structures[128] (vide infra).

Residue-specific disorder before and after channel inactivation. Channel inactivation in KcsA is controlled by structural changes at the selectivity filter that represents the inactivation gate and a large hinged motion around the inner helix bundle (the activation gate). In addition, KcsA single-channel recordings show kinetically complex behaviors that are commonly referred to as modal gating. A structural understanding of such local fluctuations is still limited[24]. With our 800 MHz DNP setup, we studied the channel in the closed-conductive (Fig. 3-6) and Fig. 8a-c, zoom in) and open-inactivated (Fig. 8d-g, zoom in) conformation to be able to compare conformation of the selectivity filter in both states. In the closed-conductive state, we analyzed 2D CC (Fig. 8c) and NC spectra (Fig. 8b) both at AT (black) and LT-DNP (red) conditions.

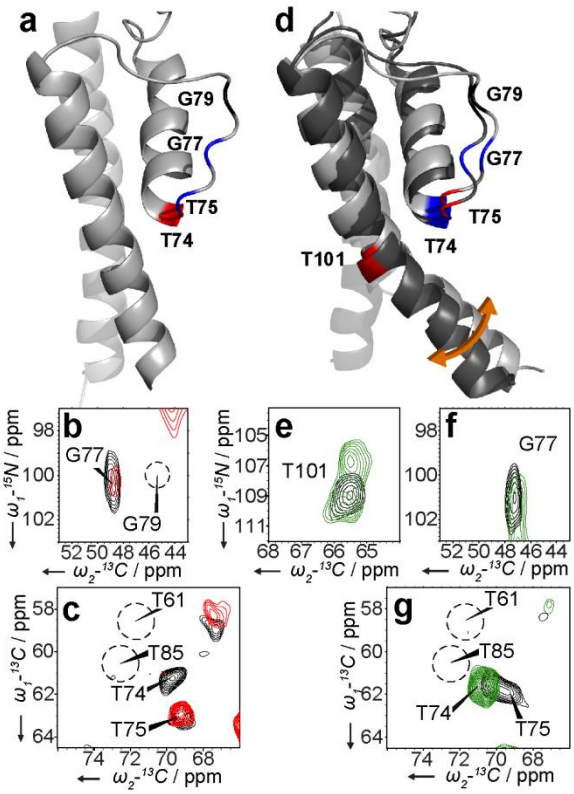

Figure 8. Comparison of AT (black) and LT-DNP (red/green) ssNMR before (a-c) and after inactivation (d-g). a) and d) structures are taken from ref [131] and [128]. Channel residues that are apparent in the LT spectra are given in blue on the KcsA structure. Residues that disappear or exhibit strong line broadening at LT are indicated in red. In d, two channel conformations (referring to an activation gate opening of 23 and 32 Angstrom, respectively), that are most compatible with the ssNMR data are overlayed. b) and c) represent zoom-ins from Fig 5. and Fig. 4a respectively.

We observed that the peak of residue Thr 74 at the lower part of the selectivity filter (indicated in red in Fig. 8a) is broadened by a higher degree of structural heterogeneity (see also Fig. 3) compared to residues such as Thr 75 and Gly 77 that are located towards the center of the selectivity filter (Fig. 8a, blue). Our results obtained on the closed-conductive state of KcsA hence suggested that residue-specific channel dynamics lead to local disorder under LT-DNP conditions.
We compared then our findings of Fig. 8a-c to the channel conformation after inactivation that can be induced by lowering pH and by reducing K+ concentrations below 20 mM[17,131] (Fig. 8e-g). Spectra recorded at

AT conditions are shown in black and LT-DNP in green. In line with our earlier studies on the closely related KcsA-Kv1.3 channel[17,18], we observed chemical shift changes in the selectivity filter. Compared to the AT data (black, Fig. 8e-g), we now however detected signal attenuation for Thr 75 at LT-DNP conditions (Fig. 8g, green) that was clearly visible before inactivation (Fig. 8c), i.e., in the closed conductive state. Interestingly, Thr 74 now is readily apparent in the open inactivated state. In contrast to the change in dynamics at the lower part of the SF, the upper part of the SF showed no change in dynamics. We can conclude by the clear appearance of residue Gly 77 before (Fig. 8b) and after inactivation (fig. 8f) that in both states this residue showed no disorder. Notably, that the same residue exhibited the strongest DNP enhancements (Fig. 6 and 7). We note that SF residues towards the extracellular side could not be examined due to PREs, e.g. residue Gly 79 of the SF remained attenuated (Fig. 8b and Fig 1b).

In the open-inactivated state under LT-DNP conditions, we also observed peak doubling at Thr 101 (Figure 8e, green) which is situated at the gating hinge of the activation gate. This residue exhibits a well characterized ssNMR chemical shift change[17,18] as a result of opening of the activation gate (Fig. 8d). Note that these observations were insensitive to changes to stronger acidic pH in our proteoliposomal preparations (Supporting Figure 4c). To understand the nature of the peak doubling observed at Thr 101, we investigated whether changes in activation gate opening as seen in KcsA mutant crystals would lead to chemical-shift variations in our ssNMR spectra. Crystal structures of constitutively open KcsA mutants had revealed various degrees of activation gate opening ranging from 23 to 32 Angstrom[128]. Indeed, when comparing ^{13}Ca, and ^{15}N chemical shift predictions for open mutants forms between 23 Angstrom and 32 Angstrom, the size and trend in chemical shift variations were in remarkable agreement with our experimental results (SI Fig. S3). Assuming that the ssNMR signal intensity reports on the relative population of these opening events, our ssNMR data would be most compatible with the dominant contribution of two channel conformations: one species that only exhibits a limited opening (23 Angstrom) and a second population that displays are fully open activation gate (32 Angstrom) in our ssNMR spectra. These results would be consistent with structural fluctuations of the activation gate even under strongly acidic pH conditions where the activation gate is fully open[164].

Conclusions

Dynamic Nuclear Polarization has become a powerful method to enhance spectroscopic sensitivities in the context of NMR and MRI. On the other hand, the availability of standard high-field NMR instruments has greatly enhanced the possibility to study complex (bio)molecular systems where spectral resolution is critical. We have shown that high field DNP significantly enhances the prospects to conduct in-depth structural investigations of complex molecules such as membrane proteins in different functional states.

We have demonstrated that these conditions can not only enhance spectral resolution but also offer the possibility to utilize the intrinsic paramagnetic properties of the polarizing agents as direct structural probes during the spectroscopic analysis. In the case of the membrane embedded KcsA channel, our results help to pinpoint the water accessible pore of the channel in membranes. The most solvent-exposed surface shell exhibits strong PREs, at least under the conditions used in our experiments. We suspect that similar processes are also present in the context of material science applications.

The comparison of DNP data to results obtained at ambient temperatures furthermore allowed us to obtain insight into the role of ion channel plasticity before and after inactivation. This flexibility could be closely related to modal gating that represents an effective regulatory mechanism by which ion channels control the extent and time course of ionic fluxes. Our experiments identified specific selectivity filter residues that exhibit conformational flexibility before (Thr 74) and after inactivation (Thr 75, Thr 101). These observations underline that both gates are coupled[17,22] and support emerging views[24,185] that small structural fluctuations of the filter backbone can have drastic effects on gating changes. Compared to earlier DNP studies that were mostly conducted at 400 MHz, we find reduced overall signal enhancements at 800 MHz DNP conditions. This reduction is higher than reported in theorectial discussions in the literature[205] but it is in line with recent studies of AMUPol at lower magnetic fields[206]. As discussed before, the actual signal enhancements may also depend on the details of the sample conditions. For further studies on this subject, the membrane-embedded KcsA channel for which ssNMR resonance assignments as well as structural data are available[131,184] may represent a valuable experimental reference. For example, Gly 77 that is located at the center of the selectivity filter did not show conformational flexibility in the two functional states considered and exhibited the largest residue-specific DNP enhancements.

In parallel, further optimizations of the instrumental details including the use of lower temperatures[182] or of pulsed DNP setups[207] may greatly improve DNP enhancements at high magnetic field. Moreover, our results using AMUPol indicate that modifications of the polarizing agent (see, e.g., Ref.[208]) or of the proton density of the target molecule itself[198,209–211] additionally enhance the potential of DNP-supported structural biology. Note that in such studies reference data obtained using conventional NMR setups that we here used to examine the high-field DNP performance and the details of the PRE mechanism would not be required. These considerations provide additional opportunities for in-depth studies of the conformational landscape that describes the workings of complex (bio)molecules using high field DNP technology.

Supporting Information

Table S1. Residue-specific analysis of signal attenuations in membrane-embedded U(13C,15N) KcsA in the presence of 5 mM TOTAPOL

Residue	Attenuation (%)	St. dev	Residue	Attenuation (%)	St. dev
A28	4	9	E71	16	16
I38	2	13	T72	10	12
Y45	0	7	T74	14	11
A50	-2	5	T75	4	7
E51	1	5	V76	19	9
R52	-6	16	G77	21	N/A
G53	78	6	Y78	-1	9
A54	46	12	G79	82	N/A
P55	35	18	D80	78	12
G56	79	5	L81	61	21
A57	17	22	Y82	76	3
Q58	33	N/A	P83	37	28
I60	35	21	V84	40	22
T61	56	24	T85	49	13
Y62	67	24	W87	9	17
P63	30	24	A98	7	17
A65	0	38	G99	15	N/A
L66	1	8	V115	7	15
W67	49	24	G116	26	7
W68	42	16			

* Firstly, the signal-to-noise of resolved cross peaks in PDSD spectra recorded before I(0) and after addition of 5 mM TOTAPOL and 20% glycerol-d8 I(t) (see Figure 1a, main text) was determined using Sparky (T. D. Goddard and D. G. Kneller, SPARKY 3, University of California, San Francisco). The attenuation was subsequently computed as (I(0)-I(t))/I(0) after normalization of the S/N ratios. Whenever more than one correlation could be identified per protein residue, the average was calculated and used to determine the standard deviation.

Table S2. Residue-specific analysis of PRE-induced signal attenuations in membrane-embedded U(13C,15N) KcsA in the presence of 25 mM AMUPol

Residue	Attenuation (%)	St. dev	Residue	Attenuation (%)	St. dev
A29	11	29	W68	1	41
I38	0	26	E71	-1	7
Y45	30	18	T72	16	17
A50	36	4	T74	9	27
E51	0	N/A	T75	1	12
R52	7	20	V76	18	25
G53	75	N/A	G77	38	N/A
A54	23	17.3	Y78	30	16
P55	55	29	G79	82	N/A
G56	80	N/A	D80	83	3
A57	75	8	L81	40	37
Q58	30	32	Y82	17	34
I60	29	28	P83	57	16
T61	20	13	V84	70	19
Y62	3	67	T85	30	18
P63	16	32	W87	23	12
A65	2	13	A98	11	5.7
L66	13	27	G99	0	N/A
W67	42	18	G116	3	N/A

* Firstly, the signal-to-noise of resolved cross peaks in PDSD spectra recorded before I(0) and after addition of 25 mM AMUPol and 20% glycerol-d8 I(t) (see Figure 1a, main text) was determined using Sparky (T. D. Goddard and D. G. Kneller, SPARKY 3, University of California, San Francisco). The attenuation was subsequently computed as (I(0)-I(t))/I(0) after normalization of the S/N ratios. Whenever more than one correlation could be identified per protein residue, the average was calculated and used to determine the standard deviation.

Table S3: Residue Ca FWHH and its standard deviation for data obtained on KcsA 5 mM TOTAPOL or 10 mM TOTAPOL measured at 800 MHz, LT conditions, KcsA measured at 700 MHz AT conditions and the chemical shift distribution calculated from the MD trajectory.

	5 mM TOTAPOL, 800 MHz, LT			10 mM TOTAPOL, 800 MHz, LT		
	FWHH (ppm)	sd (ppm)	% Gaussian	FWHH (ppm)	sd (ppm)	% Gaussian
T74	1.90	0.10	0	2.00	0.08	0
T75	0.89	0.03	1.2	1.35	0.03	1.2
G77	0.75	0.02	1.2	1.42	0.03	1.2
T85	2.63	0.15	0	11.6	1.1	0
G79	1.66	0.11	1.2	2.24	0.15	0

	no TOTAPOL, 700 MHz, AT			MD trajectory	
	FWHH (ppm)	sd (ppm)	% Gaussian	FWHH (ppm)	sd (ppm)
T74	0.80	0.02	1	1.62	0.05
T75	0.65	0.02	1	0.863	0.018
G77	0.581	0.016	1	1.26	0.03
T85	0.68	0.03	1.5	1.49	0.04
G79	0.640	0.017	1	0.888	0.019

Data obtained in 2:2:1 D_2O/H_2O/glycerol-d8 were fitted with a mixed Gaussian and Lorentzian line shape using Topspin 3.0. Peaks are extracted from an NCA or proton driven spin diffusion (T85 only) experiments. The line widths and its standard deviation deduced from the MD trajectory and predicted with SPARTA+ are fitted with a Gaussian curve. Bins of 0.1 ppm were used. The fitting was done with SigmaPlot 12.3.

Table S4. Residue-specific enhancements measured for protonated/deuterated KcsA for different biradicals.

		5 mM TOTAPOL		25 mM AMUPOL		$^{2}H^{13}C^{15}N$ KcsA 25 mM AMUPol	
Residue	Correlation	DNP ε	standard error	DNP ε	standard error	DNP ε	standard error
I38	CA CB	5.6	1.4	5.1	0.7	-	-
A54	CA CB	3.8	1.6	6.2	1.5	-	-
P55	CA CD	3.4	0.7	-	-	-	-
A57	CA CB	3.5	1.0	-	-	-	-
I60	CA N	3.4	0.6*	-	-	5.7	0.6*
T61	CA N	4.8	1.7	4.9	1.8	-	-
P63	CA N / CA CD	2.1	0.5*	-	-	-	-
T74	CA N	3.4	0.6	4.9	1.4	-	-
T75	CA N / CA CB	4.2	0.6	4.1	1.1	3.0	0.5*
G77	CA N	9.5	2.2	4.7	2.2*	17.0	1.1*
G79	CA N	5.2	0.6*	-	-	5.2	0.5*
P83	CA CD	4.6	1.1	-	-	-	-
T85	CB N	2.6	0.6	4.6	1.3	5.2	0.5*
I100	CA CB	3.5	0.6*	6.0	0.8*	-	-

Standard error of the DNP enhancement ($s_{DNP\varepsilon}$) is calculated in the following way: $s_{DNP\varepsilon} = \sqrt{\left(\frac{N_{ON}}{I_{ON}}\right)^2 + \left(\frac{\sigma_{N,ON}}{N_{ON}}\right)^2 + \left(\frac{N_{off}}{I_{off}}\right)^2 + \left(\frac{\sigma_{N,off}}{N_{off}}\right)^2}$ in which I is the cross peak signal intensity, N is the noise and σ_N is the standard deviation of the noise. In case multiple cross peaks (n) of a particular cross peak were resolved, the standard errors of the individual cross peaks were added in the following way: $s_{DNP\varepsilon} = \frac{1}{n}\sqrt{s_{DNP\varepsilon,1}^2 + s_{DNP\varepsilon,2}^2 \ldots + s_{DNP\varepsilon,n}^2}$

*upper standard error could not be determined due to lack of S/N in the spectrum recorded without microwaves.

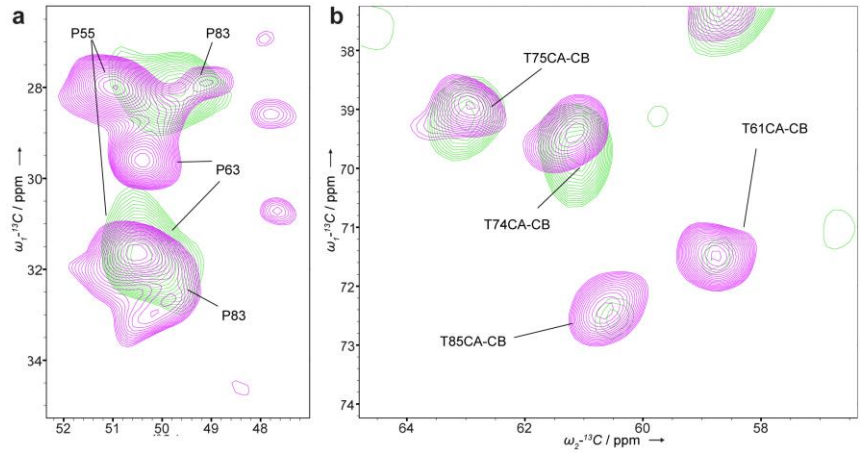

Figure S1. Spectral cutouts of (a) proline and (b) threonine regions of 2D PDSD data at 400 MHz AT conditions shows less attenuation of signals in the presence of 25 mM AMUPol (pink) in comparison to samples containing 5 mM TOTAPOL (green).

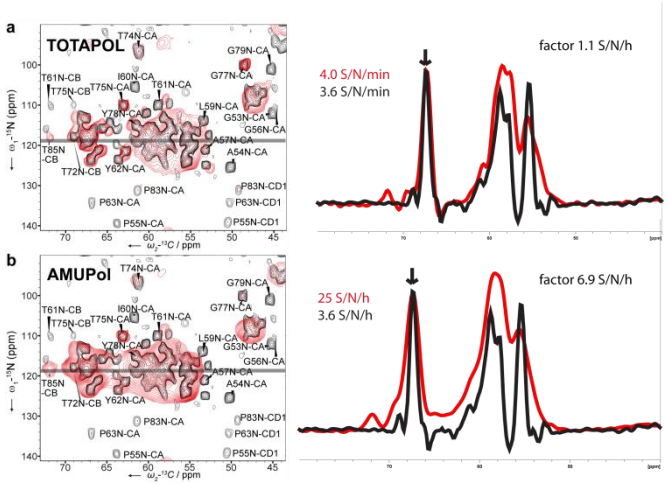

Figure S2. LT-DNP ssNMR sensitivity per unit of time of a 2D NCA spectrum (red) compared with AT ssNMR NCA spectrum without biradical (black). Signal to noise ratio per hour are calculated from the slices (c,d) taken from the 2D spectrum (a,b). The same 2D spectra are depicted in figure 5. Recording time, number of increments and t1 evolution are taken into account. Without normalization the numbers of S/N/h are as follows; 74, 51, 138 S/N in 21, 7.3, 8.4 hours for the NCA at AT witout biradical, NCA at LT with TOTAPOL and NCA at LT with AMUPOL, respectively. The resulting signal-to-noise ratios are normalized for the difference in number of scans and for the difference in magnetic field strength, see details ssNMR experiments & Processing figure 5.

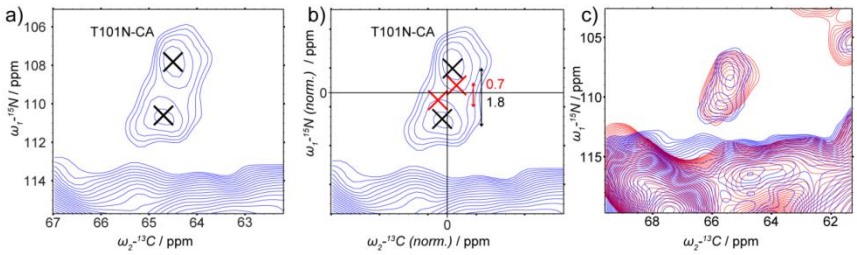

Figure S3. NCA spectra of U(13C,15N) KcsA under LT-DNP conditions reveal substates of the activation gate. (a) Peak doubling observed at residue Thr 101. (b) experimental result from (a) compared to relative chemical shift changes predicted on the basis of 23 Å and 32 Å opening of activation gate (red, using PDBs 3F7V and 3F5W (Ref.[128]) and a prediction procedure as in Ref.[131]. The predictions were taken from SPARTA+[212], which have a standard deviation of 2.45, 0.94 ppm for δ15N, δ13Cα, respectively, between predicted and experimental chemical shift. (c) ssNMR data obtained at pH4 (blue) and pH 3.7 (red).

Details of ssNMR experiments & Processing

Figure 1a:

PDSD experiments shown in Figure 1a relate to the following experimental parameters:

Field strength, Figure color, biradical (incl. glycerol and D2O)	CP time [µs]	PDSD mixing time [ms]	Temperature [K]	MAS [kHz]	Measurement time / number of scans
400 MHz, black, no biradical mixture	800	30	273	8	9 h ns = 64
400 MHz, green, TOTAPOL	300	30	273	8	28 h ns = 192

In both cases, 1H decoupling using SPINAL64[86] was employed at 83 kHz.

For the data set, 256 t1 points and a spectral window of 20000 Hz were used. Spectra were processed using sine bell function 4 with 4k and 2k

zero filling in t2 and t1, respectively. Linear prediction with 8 coefficients was applied to t1.

Figure 2:

Proton-driven spin diffusion (PDSD) experiments shown in Figure 2 were acquired using CP times of 300 µs and PDSD mixing times of 30 ms. The sample temperature was approximately 100 K, using an MAS rate of 8 kHz and 83 kHz SPINAL64[86] decoupling. The 800 MHz 2D data set in Figure 3 was acquired using 593 t1 points using a spectral window in t1 of 46292 Hz recorded with 48 scans in 24 hour. For the 400 MHz experiments, the data set comprised 256 t1 points and a spectral window of 20000 Hz recorded with 16 scans in 4 hours. Spectra were processed using sine bell function 4 with 4k and 2k zero filling in t2 and t1, respectively. Linear prediction with 8 coefficients was applied in t1.

Figure 4:

Field strength, Figure 4x, color, biradical (incl. glycerol and D2O)	CP time [µs]	PDSD mixing time [ms]	Temp. [K]	MAS [kHz]	Measurement time / number of scans
700 MHz, a/b, black, -	600	30	273	10.921	17 h ns = 80
800 MHz, b, blue, TOTAPOL	300	30	100	8	24 h ns = 48
800 MHz, a, red, TOTAPOL	300	30	100	8	24 h ns = 48

The 800 MHz 2D data sets in Figure 4 were acquired using 593 t1 points using a spectral window in t1 of 46292 Hz. The 700 MHz spectrum was recorded with 385 t1 points and a spectral window of 35714 Hz. Spectra were processed using sine bell function 4 with 4k and 2k zero filling in t2 and t1, respectively. Linear prediction with 8 coefficients was applied to t1.

Figure 5:

NCA spectra shown in Figure 5 were recorded using SPECIFIC-CP[39] 15N-13C transfers. Further experimental parameters were:

Spectrum, Figure 6x, biradical (incl. with glycerol and D2O)	HN, CP time [μs]	SPECIFIC CP mixing time [ms]	Temp. [K]	MAS [kHz]	Measurement time / number of scans
700 MHz, a/b , -	600	3.2	273	15	21 h ns = 1104
800 MHz, a, TOTAPOL	600	4	100	8	8.5 h ns = 256
800 MHz, b, AMUPol	500	3.5	100	8	10 h ns = 448

In all cases, 1H decoupling using SPINAL64[86] was employed at 83 kHz.

The 800 MHz 2D data sets in Figure 5 were acquired using 40 t1 points using a spectral window in t1 of 5000 Hz. The 700 data set was recorded with 34 t1 points and a spectral window in t1 of 4273 Hz. Spectra were processed using sine bell function 4 with 2k or 1k zero filling in t2 and t1, respectively. Linear prediction with 4 coefficients and 40 points was applied in t1. For the 700 MHz spectrum, 8 LP coefficients and 34 points were used.

Figure 8:

The spectra in Fig. 8b,c were obtained using a sample washed with 25 mM AMUPol in 1:2:2 (v/v/v) glycerol-d8/D2O/H2O (NCA, Glycine region) or 5 mM TOTAPOL in 1:2:2 (v/v/v) glycerol-d8/D2O/H2O (PDSD CC, Threonine region). The buffer contained 50 mM NaPi pH=7, 50 mM NaCl, 50 mM KCl. Experimental parameters and processing of spectra were as described for Fig. 6 and 5.

All spectra in Fig. 8e-g were obtained from a sample washed with 10 mM TOTAPOL in 1:2:2 (v/v/v) glycerol-d8/D2O/H2O. The buffer contained 20 mM citrate pH=4, 10 mM NaCl. Experimental parameters and processing of spectra are as described above for Fig. 6 and 5. The

NCA were recorded in 44 hours with 896 scans and the PDSD CC were recorded in 16 hours with 256 scans.

Chapter 7

Biomolecular DNP- supported NMR spectroscopy using site-directed spin labeling

Elwin A.W. van der Cruijsen,[#], Eline J. Koers[*#], Raymond E. Hulse[+], Eduardo Perozo[+], Marc Baldus[*]*

*Bijvoet Center for Biomolecular Research, Utrecht University
+Department of Biochemistry and Molecular Biology, Center for Integrative Science, University of Chicago
# contributed equally

Under review

Abstract

The site-specific addition of chemical probes that can be detected in high sensitivity has greatly enhanced the use of fluorescence and light microscopy in applications ranging from optogenetics to catalysis. In NMR spectroscopy, dynamic nuclear polarization (DNP) has become a widely usable method to significantly enhance overall spectroscopic sensitivity. Here we show that DNP can be established by creating local spin clusters via site-directed spin labeling. Applied to a membrane-embedded potassium channel, we show that this approach can significantly enhance NMR sensitivity and causes signal modulation in a site specific way. DNP by site-directed spin labeling may hence become an attractive route in applications ranging from complex (bio)materials to cellular preparations.

Introduction

Molecular probes that combine the benefits of enhanced spectroscopic sensitivity with site-specific localization have significantly expanded the chemical repertoire to track molecular structure and function in applications ranging from cell biology[213,214] to material science.[215] In the field of magnetic resonance, dynamic polarization (DNP) has been show to greatly enhance spectroscopic sensitivity in solid[216] and solution-state[172] NMR. Usually, such studies involve the addition of soluble paramagnetic compounds to enhance NMR signals via DNP at low temperatures (LTs).

In the following, we demonstrate that sizable DNP enhancements can be achieved by directly labeling DNP-active molecular units to the target molecule of interest. Previous efforts in this direction examined endogeneous radicals (flavomonucleotide [209]) or involved attachment of a biradical (TOTAPOL[217]) C-terminally to a decapeptide.[218] Here, we aim at a general route to study (membrane) proteins using localized DNP. For this purpose, we employed site-directed spin labeling using the well-established MTSL(S-(2,2,5,5-tetramethyl-2,5-dihydro-1H-pyrrol-3-yl)methylmethanesulfonothioate) approach that provides the basis for structural studies in EPR.[219,220] In NMR, the addition of site-specific spin labels leads to paramagnetic relaxation effects (PREs) and pseudocontact shifts that are known to affect spectral resolution and report on molecular 3D structure.[176]

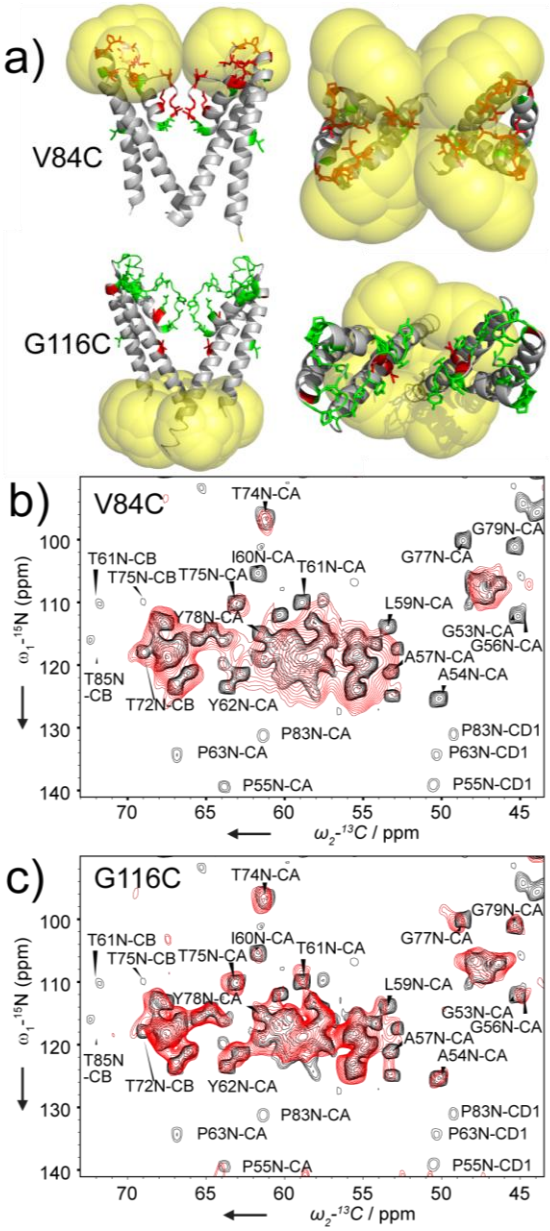

Figure 1. a) Rotamers plotted on a dimer structure of KcsA assuming a 2 site and 4 site MTSL labelling (yellow spheres) for V84C (top) and G116C (bottom) in side- and topview. Residues exhibiting no (green) or sizable (red) PREs are indicated. (b,c) Comparison of NCA spectra of WT KcsA (black) to NMR results obtained on paramagnetically labelled (b) V84C and (c) G116C in red at 273 K sample temperature.

In our studies, we investigated the membrane-embedded bacterial potassium KcsA, which has been well characterized by EPR[14] and solid-state NMR.[131] Since KcsA is a homotetramer with no natural cysteines, we examined in detail the effect of a single cysteine mutation at two different channel locations. We focused on the mutations V84C and G116C that are well characterized by EPR.[14,159] Residue 84 is part of the turret between the selectivity filter (SF) and the transmembrane-helix 2 (TM2), while G116 is located between the lipid bilayer and the activation gate (Figure 1a).

Results and Discussion

Using published ssNMR assignments[131,184] we firstly verified by ssNMR experiments at 273 K that paramagnetic tagging at increasing concentrations was site specific (Figure 1b,c and SI Figure 1). Indeed, NCA spectra recorded for both preparations confirmed PREs (figure 1a) in a distance range of roughly 10 Å around the mutation site in line with theoretical expectations[176]. Especially in the turret region where ssNMR assignments are complete, labelling at position V84C largely quenches signals (red in Figure 1a) providing valueable PRE restraints about the 3D fold of the channel. On the other hand, spin labelling at position 116 preserved turret and filter residue signals (Figure 1c) and we observed only small changes for residues that establish a link to the lipid bilayer and form a coupled network during channel inactivation.[131]

So far, the highest DNP enhancements have been obtained using the Cross Effect (CE) that depends on the electron-electron dipole coupling strength.[205,221] Taking into account the tetrameric channel arrangement and known MTSL rotamer properties, we modelled[167,222] the electron-electron distance distribution for both considered positions (Figure 2a,c). We obtained a broad distribution of inter-electron distances with an average e^- - e^- distance of 25.6 Å (Pos 84) and 20.8 Å (Pos 116) in a closed-conductive model of KcsA. The corresponding distances in DNP biradicals such as TOTAPOL or AMUPol[206] are shorter but well within the overall distribution shown in Figure 2a and c. To investigate the effect of increasing levels of paramagnetic tagging upon spectral resolution and DNP enhancement, we conducted 2D LT-DNP experiments at 400 MHz and 800 MHz conditions (see SI).

We varied the ratio of MTSL and MTS, the diamagnetic N-acetylated spin label analogue of MTSL in the range of 25%, 50%, 75 and 100% and compared our results to the high-temperature data.

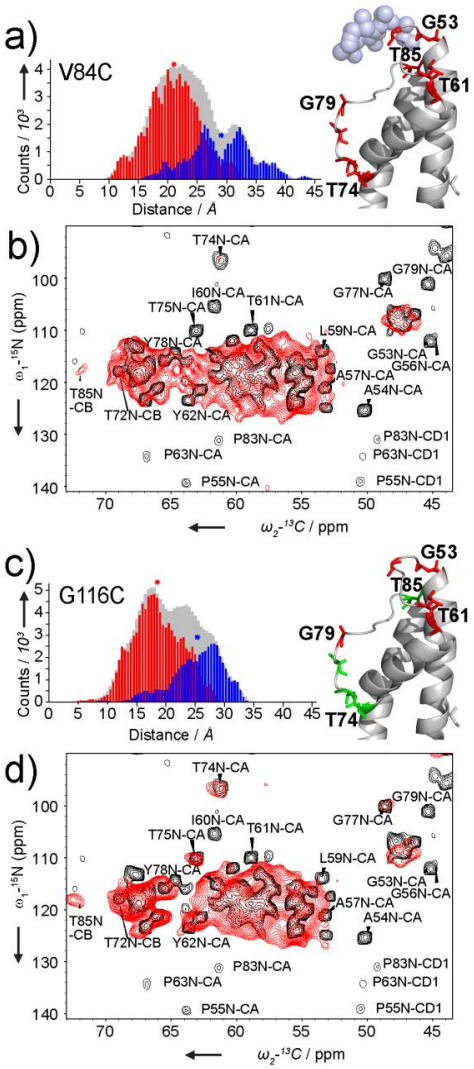

Figure 2. Predicted distances between MTSL radical rotamers of a) V84C and c) G116C for adjacent (red) and diagonal (blue) e^- positions and combinations thereof in grey. Dots depict the average distance. Radicals attached to G116C show the shortest average distance, which is reflected in a higher DNP enhancement. 800 MHz LT-DNP 2D NCAs of V84C (b) and G116C (d). Note that in b all SF signals are missing whereas in d Thr75 and Thr74 are visible at LT-DNP conditions. When plotted on the structure of the SF, these results confirm the presence of PRE's (a, red residues) close to the radical (a, blue spheres). In spectrum d, signal attenuation at the turret can be well explained by, as plotted on the structure (c), structural disorder (c, red) that does not affect T74 and T75 (green, c).

In the case of the V84C mutant, the LT-DNP signals of residues in the SF and turret region (Fig. 2a, red residues) were strongly attenuated (Fig. 2b). In contrast, in the G116C sample only signals stemming from the upper part of the SF and the turret region were missing (Figure 2c,d, see also SI Fig. 4). These results clearly demonstrate that at LT-DNP

conditions, PREs (that increase compared to the AT case due to the longer electron T_1 relaxation time[223]) can readily be used as structural probes (Figure 2a). Any signal attenuation distant from the tag (Fig. 2c) can be well explained by structural disorder at LT conditions, as confirmed by additional ssNMR experiments on KcsA at higher temperatures (ref.[152] and manuscript in preparation).

When varying the radical concentration from 25 to 100 % (Figure 3), we observed a clear correlation between the overall signal enhancement and experimental DNP build-up times $1/T_{DNP}$. Absolute enhancements shown in Figure 3 were obtained from set of KcsA samples that were simultaneously solubilized, labeled and reconstituted as described in Ref.[14] Additional experiments suggest that these values may in part be influenced by variations in preparation procedure, for example leading to unspecific binding of MTSL to membranes. In line with our recent studies using soluble biradicals we observed a four-fold decrease when comparing DNP enhancements at 400 MHz and 800 MHz.

Based on the shorter average interspin distance of G116C, we expected a higher DNP enhancement for the G116C mutant than the V84C mutant. Indeed, we observed a 2.5 times higher signal enhancements for G116C compared to the same MTSL loading for V84C (see Figure SI 2) confirming the presence of CE-DNP. In fact, the DNP enhancements using 100 % tagging at G116C (ε = 14.5 at 400 MHz/ 263 GHz) improve sensitivity by a factor 12 compared to conventional (AT) ssNMR (see, SI Figure 5) and were higher than seen in preparations using WT KcsA and TOTAPOL in solution.

Assuming 100% labeling efficiency, we estimated a global radical concentration of 19 mM for the 100% MTSL tagged sample. A comparable 10 mM TOTAPOL concentration in solution yielded a DNP enhancement of 13 at 400 MHz for WT KcsA. Minimizing the H2O-content in our proteoliposomal preparations did not reduce the enhancement (SI Figure 3), indicating the proton-driven spin diffusion via the solvent is not important for the observed polarization enhancement. Also, initial experiments using diluted KcsA samples suggest that the observed enhancements are largely determined by intramolecular electron-electron interactions.

Figure 3 suggests that higher DNP enhancements should be possible, for example by deuteration of the target protein.[209] Also, the use of nitroxide radicals with a longer T_{1e}/T_{2e},[206,224] including AMUPol[206] or the optimization of the radical geometry might further increase the use of DNP by site-directed spin labeling. On the other hand, DNP enhancements may report on overall structural changes, such as in the case of KcsA, where structural changes related to inactivation can lead to weaker electron-electron dipolar couplings.[14]

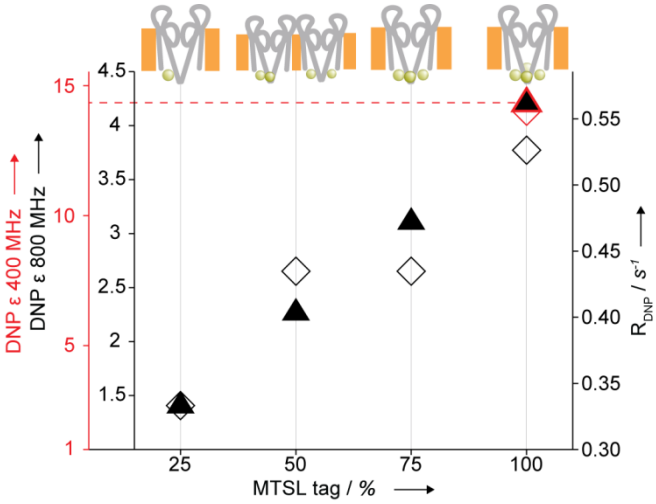

Figure 3. DNP enhancements seen in 1D NCA experiments (▲, 800 MHz) and the inverse polarization DNP build-up time R_{DNP} (◇ ,800MHz) at LT for KcsA G116C. Cartoons (top) depict the dominant MTSL labeling arrangements expected for the various amounts of labeling. DNP enhancements at 400MHz are indicated by red dashed line and R_{DNP} by ◇.

In summary, we have demonstrated that significant DNP enhancements can be achieved by creating local electron clusters. Unlike local NMR enhancements methods such as photo-CIDNP,[225] these enhancements are visible outside a core shell where PREs are active and can lead to spectral simplification in LT-DNP ssNMR data sets. Outside this shell, we did not observe sizable variations in DNP enhancements (Table S1). These findings are in excellent agreement with earlier work on complex biomolecules suggesting that DNP enhancements induced by local

electron clusters are dictated by spin diffusion processes and can be constant over at least tens of nanometers. [204,226]
NMR studies using DNP by site specific labelling should hence be readily possible for other oligomeric proteins such as regularly observed in the case of membrane proteins or present during the process of folding and aggregation. Future applications could utilize other chemical routes, for example involving unnatural amino acids [227] or the addition of functionalized nanoparticles recently shown in the case of MRI.[228] DNP using chemical tagging may also provide an attractive route in cases where solubility is of critical influence or when a water soluble radical leads to undesirable PREs at the solvent-protein interface. Finally, DNP using spin labeled components offers a means to introduce molecular specificity into DNP studies, for example by placing the DNP agents on specific molecular components such as ligands, lipids or nucleotides. Such strategies may enhance the DNP-based investigation of large biomolecules such as ribosomes[54] or cellular preparations[200] for which the general use of DNP has already been demonstrated.

Experimental Section

Proteolipsomal samples containing uniformly [^{13}C,^{15}N] labelled KcsA G116C and V84C were prepared and tagged with MTSL and MTS as described before.[14,159] For DNP-based ssNMR experiments, we washed liposomal KcsA samples 2x with 50 μL DNP solution containing 1:2:2 (v/v/v) glycerol-d8, D2O, and H2O. ssNMR (AT at 273 K) and LT-DNP (100 K) experiments were conducted using 3.2 mm triple-resonance (^{1}H,^{13}C,^{15}N) magic-angle-spinning (MAS) probe heads at static magnetic fields of 9.4 to 18.8 T corresponding to proton/electron resonance frequencies between 400 MHz/ 263 GHz, 700 and 800 MHz/ 527 GHz (Bruker BioSpin). For further information, see supporting information.

Supporting Information

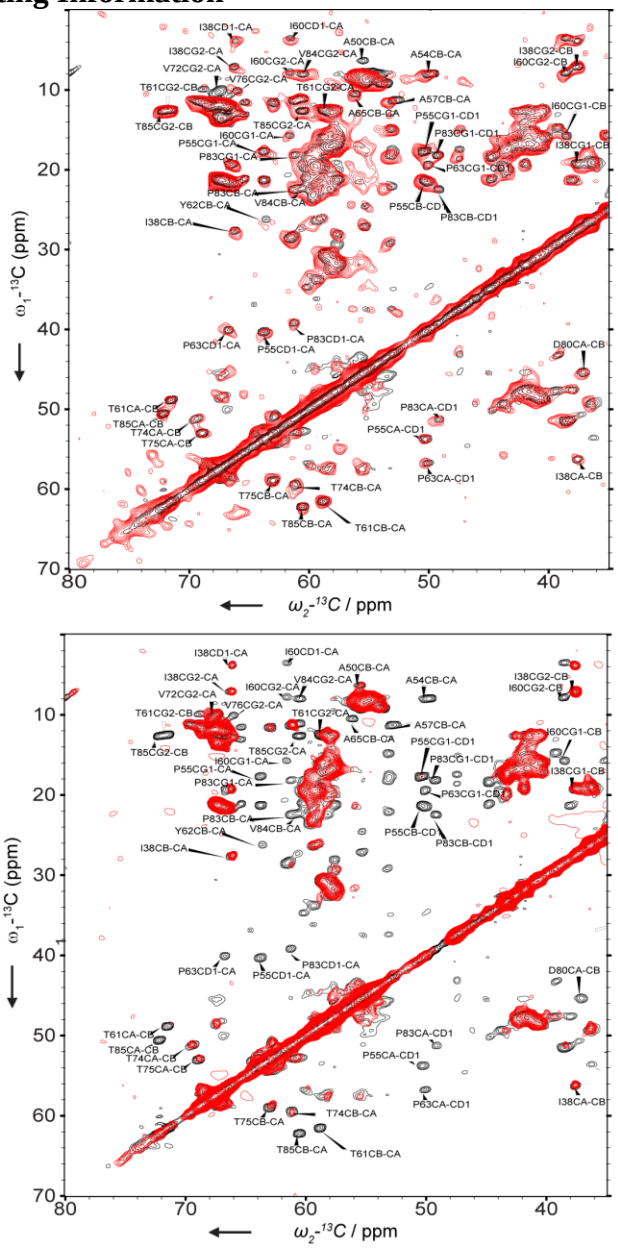

Figure S1: Spectral comparison of 75% MTS spin labeled [$^{13}C^{15}N$] KcsA G116C (red, top) and 75% MTS spin labeled V84C (red, bottom) with non-labeled WT [$^{13}C^{15}N$] KcsA (black).

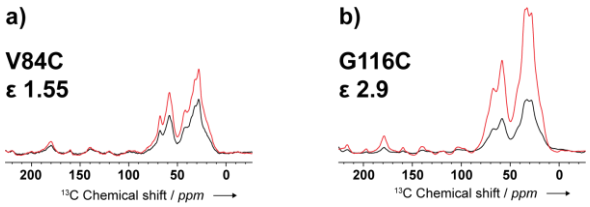

Figure S2. 1D ^{1}H-^{13}C CP/MAS spectra of 75% MTSL KcsA G116C (a) and V84C (b) measured with (red) and without (black) microwaves at 800 MHz /527 GHz.

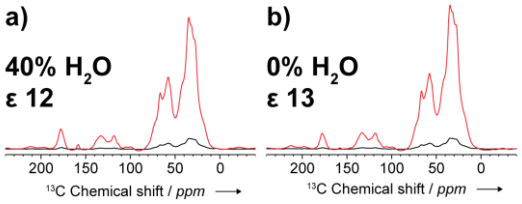

Figure S3. 1D ^{1}H-^{13}C CP/MAS spectra of 100% MTSL G116C with 40% H_2O (a) and 0% H_20 (b) measured with (red) and without (black) microwaves at 400 MHz /263 GHz. 0% H_2O shows the transfer of magnetization from the electrons to the proteins in the membrane without spin diffusion via the solvent.

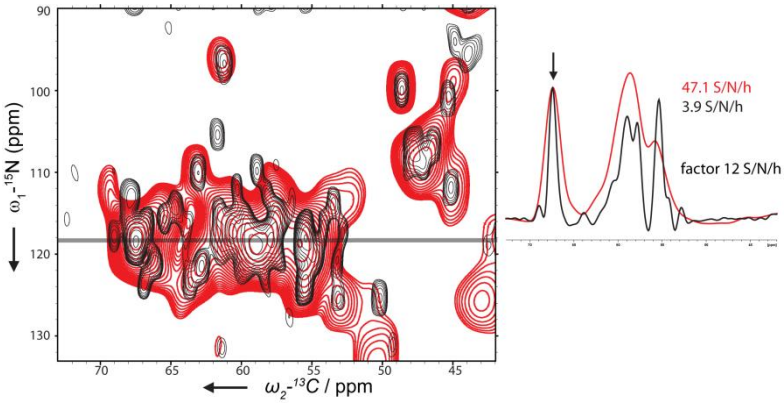

Figure S5. Comparison of the LT-DNP 2D NCAs of 100% MTSL G116C with microwaves on at 400 MHz (red) and 800 MHz (blue) with conventional ssNMR NCA recorded at the 700 MHz. The Signal to noise are corrected for the difference in number of scans and magnetic field strength.

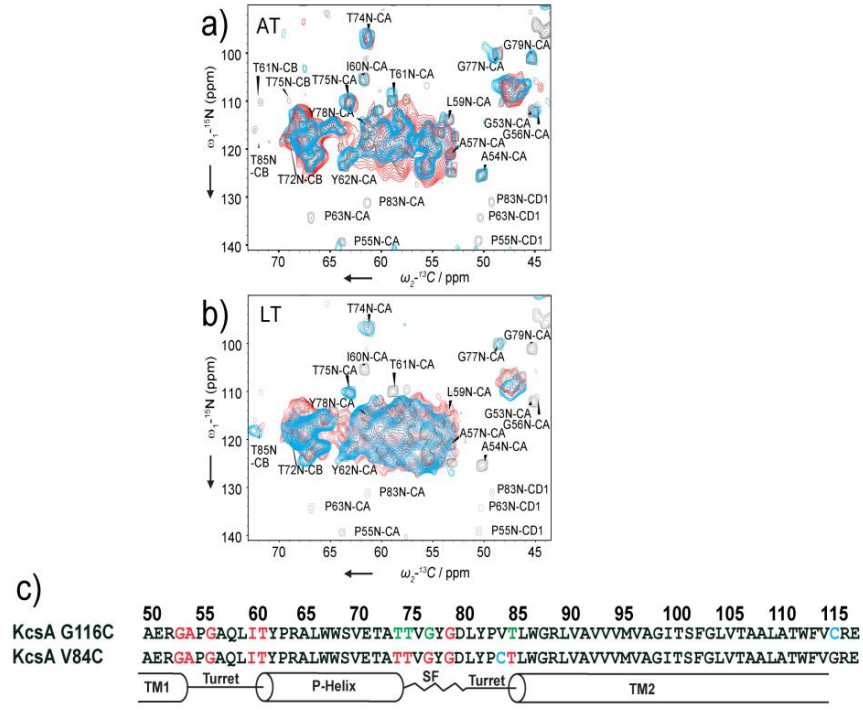

Figure S4. Comparison of 2D NCAs of 75% MTSL V84C (red) and G116C (blue) at AT (a) and LT (b) underlining that the position of the tag influences the overall correlation pattern. (c) Sequence shown with the secondary structural elements, where residues highlighted in red, with an S/N lower than 4, are affected by PRE or are broadened by molecular heterogeneity. The MTS labeled residue is highlighted in blue and green residues are observable in the spectrum.

Table S1. Residue-specific enhancements measured for KcsA with different MTSL loading at 800 MHz/527 GHz.

Residue	G116C			V84C
	100% MTSL DNP ε	75% MTSL DNP ε	50% MTSL DNP ε	75% MTSL DNP ε
T74	2.8	3.3	2	N/A
T75	2.9	2	2.3	3
G77	3.1	2.3	2.3	N/A
G79	2.2	N/A	N/A	N/A

Rotamer Analysis

The program MMM was used to perform the rotamer analysis and to predict electron-electron distances for the PDB file 1JVM.[167,222,229] A symmetry frame was set to residue 79 of KcsA to ensure proper measurements. The results of the rotamer analysis were analyzed and displayed in Matlab.

ssNMR experiments & Processing Details

Figure 1

NCA spectra shown in Figure 1 were recorded using SPECIFIC-CP[39] ^{15}N-^{13}C transfers. Further experimental parameters were:

Spectrum, Figure 1x, loading	HN, CP time [µs]	SPECIFIC CP mixing time [ms]	Temperature [K]	MAS [kHz]
700 MHz, b/c , -	600	3.2	273	15
700 MHz, b, V84C 75% MTSL	600	3.2	273	10.9
500 MHz, c, G116C 75% MTSL	700	3.0	273	8

In all cases, ^{1}H decoupling using SPINAL64[86] was employed at 83 kHz.

The V84C 2D data set in figure 1 was acquired using 30 t_1 points using a spectral window in t_1 of 5000 Hz. The 500 MHz 2D data set was

recorded with 23 t_1 points and a spectral window in t_1 of 2793 Hz. The 700 MHz reference data set was recorded with 34 t_1 points and a spectral window in t_1 of 4273 Hz. Spectra were processed using sine bell function 4 with 4k and 2k zero filling in t_2 and t_1, respectively, with 4 coefficients Linear prediction.

Figure 2

NCA spectra shown in Figure 2 were recorded using SPECIFIC-CP[4] ^{15}N-^{13}C transfers. Further experimental parameters were:

Spectrum, Figure 1x, loading	HN, CP time [µs]	SPECIFIC CP mixing time [ms]	Temperature [K]	MAS [kHz]
700 MHz, b/d , -	600	3.2	273	15
800 MHz, b, V84C 75% MTSL	500	3.5	100	8
800 MHz, d, G116C 75% MTSL	500	3.5	100	8

In all cases, ^1H decoupling using SPINAL64[86] was employed at 83 kHz.

The 800 MHz 2D data sets in figure 2 were acquired using 30 t_1 points using a spectral window in t_1 of 5000 Hz. The 700 MHz data set was recorded with 34 t_1 points and a spectral window in t_1 of 4273 Hz. Spectra were processed using sine bell function 4 with 2k and 1k zero filling in t_2 and t_1, respectively. Linear prediction with 4 coefficients and 30 points was applied in t_1. For the 700 MHz spectrum, 8 LP coefficients and 34 points were used.

Figure S1

PDSD experiments shown in Figure S1 relate to the following experimental parameters:

Field strength, Figure S1x, color	CP time [µs]	PDSD mixing time [ms]	Temperature [K]	MAS [kHz]
700 MHz, top/bottom , -	600	30	273	10.9
700 MHz, bottom, V84C 75% MTSL	600	30	273	10.9
500 MHz, top, G116C 75% MTSL	600	30	273	8

In both cases, ^{1}H decoupling using SPINAL64[86] was employed at 83 kHz.

For the 2D 700 MHz data set, 385 t_1 points and a spectral window of 35114 Hz were used. For the 2D 500 MHz data set, 315 t_1 points and a spectral window of 25000 Hz were used. Spectra were processed using sine bell function 4 with 4k and 2k zero filling in t_2 and t_1, respectively. No Linear prediction was applied to t_1.

Figures S2 & S3

The spectra in Figure S2 were recorded with 8 (a) or 16 (b) scans at the 800 MHz/ 527 GHz setup. The CP contact time for all experiments was 100 μs. The spectra were processed with 150 Hz line broadening. The spectra in Figure S3 were recorded with 8 scans at the 400 MHz/ 263 GHz setup. The CP contact time for all experiments was 100 us. The spectra were processed with 150 Hz line broadening.

Materials and sample preparation

For DNP-based ssNMR experiments, the liposomal MTS spin labeled KcsA pellets were washed with 25 μL of a solution containing 1:2:2 (v/v/v) glycerol-d8, D_2O, and H_2O. After adding the solution, the sample was vortexed and centrifuged at 100,000 g for 30 minutes. The washing procedure is done twice.

Solid-state NMR and DNP

ssNMR and DNP experiments were conducted using 3.2 mm triple-resonance [^{1}H,^{13}C,^{15}N] magic-angle-spinning (MAS) probe heads at static magnetic fields of 9.4 to 18.8 T corresponding to proton/electron resonance frequencies between 400 MHz/ 263 GHz, 700 and 800 MHz/ 527 GHz (Bruker BioSpin). The novel 527 GHz DNP spectrometer utilizes a second-harmonic gyrotron microwave source with 9.7 T cryogen-free gyrotron magnet, corrugated waveguide to NMR/DNP probe, an 800 WB NMR magnet with sweep coil and an Avance III NMR console.

Chapter 8

Summary and Outlook / Samenvatting en perspectieven

Summary and Outlook

Solid-state Nuclear Magnetic Resonance (ssNMR) has made remarkable progress in the structural characterization of membrane proteins systems at atomic resolution. Such studies can be further aided by the use of molecular dynamic simulations. Moreover, ssNMR data can be directly compared to functional studies as ssNMR can be applied to native-like preparations, cell extracts and whole cells. In practice, these experiments can still be challenging due to limitations in signal to noise. To overcome such issues, Dynamic Nuclear Polarization (DNP) has become a powerful method to enhance spectroscopic sensitivity by transferring polarization from electrons to nuclei.
This thesis shows how the combination of (DNP enhanced) spectroscopic, computational, and functional studies can be used to answer unresolved structure-function questions in the context of the potassium channel KcsA.

In Chapter 2 we used these three techniques in order to show that the interaction between the K^+ channel turret region and the lipid bilayer exerts an important influence on the selective passage of potassium ions via the K^+ channel pore. The turret region connecting the outer transmembrane helix (transmembrane helix 1) and the pore helix behind the selectivity filter contributes to K^+ channel inactivation and exhibits a remarkable structural plasticity that correlates to K^+ channel inactivation. The transmembrane helix 1 unwinds and rewinds when the K^+ channel enters the inactivated state and the closed state, respectively. In addition, we provided insight into structural changes around the K^+ ion coordination sites as well as the conformational changes within the turret region and the pore helix. Further spectroscopic and computational results showed that the same channel domain is critically involved in establishing functional contacts between pore domain and the cellular membrane.

In Chapter 3, specific lipid binding to the pore domain of KcsA and chimeric KcsA-Kv1.3 was investigated on the structural and functional level by a combination of MD, NMR, and functional studies. We

showed that, while KcsA activity is critically modulated by the specific and cooperative binding of anionic nonannular lipids close to the channel's selectivity filter, the influence of nonannular lipid binding on KcsA-Kv1.3 is much reduced. The diminished impact of specific lipid binding on KcsA-Kv1.3 results from a point-mutation at the corresponding nonannular lipid binding site leading to a salt-bridge between adjacent KcsA-Kv1.3 subunits, which is conserved in many voltage-gated potassium channels and prevents strong nonannular lipid binding to the pore domain. Our findings elucidate how protein–lipid and protein–protein interactions modulate K^+ channel activity.

Using a combination of proton-detected ssNMR and long molecular dynamics simulations in chapter 4, we sketched a high-resolution map of the spatial and temporal distribution of water behind the selectivity filter of KcsA in two different gating states. This study demonstrates that buried water molecules with long residence times are spread all along the rear of the inactivated filter in this state. In contrast, the same region of the structure appears to be dewetted when the selectivity filter is in the conductive state. The transition between these states occurs on a time scale of the order of seconds. The slow recovery kinetics can be explained by these buried water molecules. We demonstrate the presence of a pathway that allows for the interchange of buried and bulk water, as required for a functional influence of buried water on recovery and slow inactivation.

In Chapter 5, we for the first time could directly examine an open-conductive conformation of KcsA by tuning the lipid environment. By use of electrophysiological experiments, we showed that a certain lipid environment stabilizes KcsA in the open-conductive conformation and makes it possible to structurally characterize this state by ssNMR spectroscopy. A particular conformation of the activation and inactivation gates of K^+ channel pore is required for ion conduction pathway. So far it was not possible to obtain structural information of the open-conductive conformation of KcsA K^+ channel due to the high extend of the C-type inactivation. We showed that more negatively charged phosphatidic acid (PA) and cardiolipin (CL) stabilize the open state of KcsA and reduce C-type inactivation of the channel, leading to

an increase of overall steady state open probability (P_O) of KcsA. For CL-rich lipid bilayers, we observed a 40% P_O, which was the most negatively charged lipid in our study. SSNMR experiments revealed that an open-conductive conformation of KcsA can be detected in CL lipid bilayers. Conformational modulation upon use of more negative lipid bilayers was observed at extracelluar and intracelluar ends of the transmembranes-helixes. Besides stabilizing the turret region connecting the outer transmembrane helix, at the intra cellular side the activation gate was partially open.

In chapter 6, we investigated the use of MAS DNP instrumentation operating at 800 MHz/527 GHz as a powerful method to enhance spectroscopic sensitivity for biomolecular ssNMR. We utilized membrane embedded KcsA in presence of the biradical AMUPol or TOTAPOL. In combination with molecular dynamics calculations and single channel measurements, the influence of transversal paramagnetic relaxation effect (PRE)s and conformational heterogeneity upon low temperatures (LT) -DNP spectra obtained at the residue-specific level was examined. Furthermore, we demonstrate an increasing spectral resolution for many ion channel residues in comparison with DNP ssNMR at 400 MHz/263 GHz.
This approach allowed us to refine the channel structure and revealed conformational sub-states that are present during two different stages of the channel gating cycle. In detail, our experiments identified specific selectivity filter residues that exhibit conformational flexibility before (Thr 74) and after inactivation (Thr 75, Thr 101).

Chapter 7 demonstrated that DNP can be established by creating local spin clusters via site-directed spin labeling of KcsA. We showed that this approach can significantly enhance NMR sensitivity and causes signal modulation in a site specific way. DNP by site-directed spin labeling may hence become an attractive route in applications ranging from complex (bio)materials to cellular preparations. By spin-labeling KcsA at a cysteine point-mutation with radical routinely used in the field of electron paramagnetic resonance (EPR), we examined the structural information from PRE and enhance significantly by the DNP effect.

Future ssNMR experiments on KcsA are likely to further extend our knowledge of the structural and dynamical aspects of ion channel function. At the same time, the KcsA system will remain a valuable tool to test and further develop (DNP) ssNMR and other biophysical methods. In the following, I will discuss four aspects in these directions.
Firstly, additional studies are needed to explain why KcsA single-channel recordings show kinetically complex behaviors that are commonly referred to as modal gating. A structural understanding of such local fluctuations is still limited. From chapter 4 we have obtained a first insight into the origin of such kinetics. It seems likely that a complete understanding will only result from a comprehensive measurement of channel dynamics, for example of the selectivity filter, in cellular membranes and in different channel states, in particular the open conductive state. As shown in chapter 5, conditions to stabilize this state without protein mutation have been found. Already, we are conducting research to compare ssNMR dynamical measurements of the wild type (WT) KcsA with point-mutations at the back of the selectivity filter mimicking the different modal gating events.
A second important aspect refers to the phenomenon of cluster formation of KcsA in *E.coli* lipid bilayers. Indeed, clustering and coupled gating were reported for a number of ion channels, including KcsA. It seems likely that ssNMR and molecular dynamics simulations can be used to study the supramolecular structures of such clusters at the atomic level.
A third field of ongoing research is the site-directed spin labeling KcsA with a biradical instead of, as described in chapter 7, a monoradical. Requiring only one natural or mutational cysteine site, this strategy could be more attractive for a broader range of DNP applications. In addition, DNP labeling using biradicals enhances the flexibility to exploit PRE's and DNP effect at a protein site of choice.
Finally, there will be continued interest in recording of ssNMR experiments and the interpretation of directly detected proton spectra, as started in chapter 4. Such experiments could provide direct structural information such as the residue-specific protonation level generating further insight into the molecular mechanism of channel gating via the proton chemical shifts. Since protons are more sensitive to chemical environment, e.g. fluctuations in aromatic ring positions, in comparison

to carbon or nitrogen nuclei, such advancements are likely to enhance the number structural probes that can be used in ssNMR, for example in the context of structure calculations as shown in chapter 2. For the general assignment of proton chemical shifts, the development of additional proton-detected ssNMR experiments may be useful.

Samenvatting en perspectieven

Vaste-stof kernspinresonantie (solid-state Nuclear Magnetic Resonance, ssNMR) heeft veel vooruitgang geboekt in de structurele karakterisering van membraaneiwitten op atomaire resolutie. Zulke studies kunnen ondersteund worden door moleculaire dynamica (MD) simulaties. Verder kunnen ssNMR data direct vergeleken worden met functionele studies, aangezien ssNMR toegepast kan worden op semi-natieve preparaties, cel-extracten en hele cellen. In de praktijk kunnen ssNMR experimenten echter gelimiteerd worden door een beperkte signaal-ruis verhouding. Een krachtige methode om dit probleem op te lossen is Dynamische Nucleaire Polarisatie (DNP), dat spectroscopische gevoeligheid verbetert door polarisatie van elektronen op kernen over te brengen.

Dit proefschrift toont aan hoe de combinatie van (met DNP versterkte) spectroscopische, computergestuurde en functionele studies gebruikt kan worden om openstaande vragen over de relatie tussen de structuur en functie van het kaliumkanaal KcsA te beantwoorden.

In hoofdstuk 2 gebruikten we deze drie technieken om aan te tonen dat de interactie tussen de extracellulaire loop van het K^+-kanaal en de lipide bilaag een belangrijke invloed uitoefent op de selectieve doorgang van kaliumionen door de porie van het K^+-kanaal. De extracellulaire loop die de buitenste transmembraanhelix (transmembraanhelix 1) en de porie-helix achter het selectiviteitsfilter verbindt, draagt bij aan inactivatie van het K^+-kanaal en vertoont een opmerkelijke structurele plasticiteit die correleert met inactivatie. Transmembraanhelix 1 rolt af en op als het K^+-kanaal respectievelijk de geïnactiveerde en de gesloten staat bereikt. Verder boden we inzicht in structuurveranderingen rondom de plaatsen van K^+-coördinatie, evenals conformationele veranderingen binnen de extracellulaire loop en de porie-helix. Verdere spectroscopische resultaten en computerberekeningen toonden aan dat hetzelfde domein van het kanaal belangrijk is voor de vorming van functionele contacten tussen het porie-domein en het celmembraan.

In hoofdstuk 3 werden specifieke binding van lipiden aan het porie-domein van KcsA en het chimere KcsA-Kv1.3 onderzocht op

structureel en functioneel niveau met behulp van een combinatie van MD, NMR en functionele studies. We lieten zien dat de activiteit van KcsA duidelijk gemoduleerd wordt door specifieke en coöperatieve binding van anionische, direct gebonden lipiden dicht bij het selectiviteitsfilter, terwijl deze invloed veel minder sterk is bij KcsA-Kv1.3. Het verminderde effect van specifieke binding van lipiden op KcsA-Kv1.3 is het resultaat van een puntmutatie op de overeenkomstige bindingsplaats die een zoutbrug veroorzaakt tussen naburige KcsA-Kv1.3 monomeren. Deze mutatie is geconserveerd in veel spanningsgeactiveerde kaliumkanalen en verhindert sterke specifieke lipide-binding aan het porie-domein. Onze bevindingen verklaren hoe eiwit-lipide en eiwit-eiwit interacties de activiteit van K^+-kanalen beïnvloeden.

Met behulp van proton-gedetecteerde ssNMR en lange MD simulaties, schetsten we in hoofdstuk 4 een hoge-resolutie kaart van de spatiale en temporale verspreiding van water achter het selectiviteitsfilter van KcsA in twee verschillende kanaaltoestanden. Dit onderzoek demonstreert dat diep weggeborgen watermoleculen met lange verblijftijden over de gehele achterkant van het geïnactiveerde filter verspreid zijn in deze toestand. Hetzelfde deel van de structuur lijkt echter droog te zijn als het selectiviteitsfilter zich in de geleidende toestand bevindt. De overgang tussen deze toestanden vindt plaats op een tijdsschaal in de orde van seconden. De langzame kinetiek van het herstel kan uitgelegd worden door deze weggeborgen watermoleculen. We demonstreren dat er een mechanisme bestaat waardoor het weggeborgen water met het bulk water kan uitwisselen, wat noodzakelijk is voor een functionele invloed van het weggeborgen water op herstel en langzame inactivatie.

In hoofdstuk 5 konden we voor het eerst direct een open-geleidende conformatie van KcsA bestuderen door de lipide-omgeving aan te passen. Met elektrofysiologische experimenten lieten we zien dat een bepaalde lipide-omgeving KcsA stabiliseert in de open-geleidende conformatie en structurele karakterisering met ssNMR spectroscopie mogelijk maakt. Een bepaalde conformatie van de activatie- en inactivatie-poorten van het K^+-kanaal is noodzakelijk voor de geleiding van ionen. Tot dusver was het niet mogelijk om structurele informatie te

verkrijgen voor de open-geleidende conformatie van het KcsA K^+-kanaal door de hoge mate van C-type inactivatie. We toonden aan dat meer negatief geladen fosfatidylzuur (phosphatidic acid, PA) en cardiolipine (CL) de open toestand van KcsA stabiliseren en C-type inactivatie verminderen, wat leidt tot een verhoging van de totale kans op opening van KcsA (P_O) in steady-state. Voor bilagen verreikt in CL, het meest negatief geladen lipide in onze experimenten, observeerden we een P_O van 40%. ssNMR experimenten toonden aan dat een open-geleidende conformatie van KcsA gedetecteerd kan worden in CL bilagen. Een effect op de conformatie door het gebruik van negatief geladen lipide bilagen was zichtbaar aan beide kanten van de transmembraanhelices. Niet alleen werd de extracellulaire loop gestabiliseerd die de transmembraanhelices verbindt aan de extracellulaire kant, maar ook was de activatie-poort aan de intracellulaire zijde alleen deels geopend.

In hoofdstuk 6 onderzochten we het gebruik van magic angle spinning (MAS)-DNP instrumentatie bij 800 MHz/ 527 GHz om spectroscopische gevoeligheid in biomoleculaire ssNMR sterk te vergroten. We maakten gebruik van membraan-geïntegreerd KcsA in aanwezigheid van de biradicalen AMUPol of TOTAPOL. In combinatie met MD berekeningen en single-channel metingen onderzochten we de invloed van transversale paramagnetische relaxatie-effecten (PREs) en van conformationele heterogeniteit bij lage temperatuur op de DNP spectra op residu-specifiek niveau. Verder demonstreerden we een verbeterde spectrale resolutie voor vele residuen van het ionenkanaal vergeleken bij DNP ssNMR bij 400 MHz/263 GHz.

Deze aanpak maakte het mogelijk om de structuur van het kanaal te verfijnen en onthulde conformationele sub-toestanden die voorkomen gedurende de twee toestanden in de cyclus van het kanaal. In meer detail identificeerden we bepaalde residuen in het selectiviteitsfilter die conformationele flexibiliteit vertonen vóór (Thr 74) en na (Thr 75, Thr 101) inactivatie.

Hoofdstuk 7 toonde aan dat het optreden van DNP bereikt kan worden door lokale spinclusters te creëren via zijketen-specifieke spin labeling

van KcsA. We lieten zien dat deze strategie de NMR gevoeligheid sterk kan verbeteren en de signalen specifiek moduleert afhankelijk van de locatie. DNP door zijketen-specifieke spin labeling zou daarmee een nuttige methode kunnen worden voor diverse toepassingen, van complexe (bio)materialen tot cellulaire preparaties. Door KcsA specifiek aan een cysteïne-puntmutatie te spin-labelen met een radicaal dat routinematig wordt gebruikt in het veld van elektronen paramagnetische resonantie (EPR), onderzochten we de structurele informatie die door PRE verschaft wordt en verkregen we een aanzienlijk vergroot DNP effect.

Toekomstige ssNMR experimenten aan KcsA zullen onze kennis over de structurele en dynamische aspecten van de functie van ionenkanalen hoogstwaarschijnlijk vergroten. Tegelijkertijd blijft het KcsA systeem waardevol om (DNP) ssNMR en andere biofysische methoden te testen en verder te ontwikkelen. In dit kader bespreek ik hieronder vier verschillende aspecten.

Om te beginnen is verder onderzoek nodig om uit te leggen waarom single-channel metingen aan KcsA kinetisch complex gedrag vertonen, dat “modale passage” genoemd wordt. Structureel begrip van zulke lokale fluctuaties is nog steeds beperkt. In hoofdstuk 4 verkregen we voor het eerst inzicht over de herkomst van deze kinetiek. Waarschijnlijk kan een compleet begrip alleen komen van alomvattende metingen van de dynamica van het kanaal, bijvoorbeeld van het selectiviteitsfilter, in cellulaire membranen en in de verschillende toestanden van het kanaal, met name de open-geleidende. Zoals we in hoofdstuk 5 lieten zien, hebben we condities gevonden om deze toestand te stabiliseren zonder dat mutaties nodig zijn. Momenteel zijn we bezig ssNMR metingen aan de dynamica van wild-type KcsA te vergelijken met die van puntmutanten achter het selectiviteitsfilter die de modale passage kunnen nabootsen.

Een tweede belangrijk aspect is het fenomeen van clusterformatie door KcsA in *E. coli* lipide bilagen. Clusterformatie en gekoppelde ionenpassage zijn al ontdekt in een aantal ionenkanalen, waaronder KcsA. Waarschijnlijk kunnen ssNMR en MD simulaties gebruikt

worden om de supramoleculaire structuur van zulke clusters op atomair niveau te beschrijven.

Een derde lopende studie is de zijketen-specifieke spin labeling van KcsA met een biradicaal in plaats van een monoradicaal zoals beschreven in hoofdstuk 7. Omdat er slechts één natuurlijke of gemuteerde cysteïne voor nodig is, zou deze strategie breder toepasbaar kunnen zijn in DNP. Verder biedt DNP met labeling van biradicalen meer flexibiliteit om PRE's en DNP effecten te onderzoeken op de positie in het eiwit naar keuze.

Tot slot zal het opnemen en analyseren van proton-gedetecteerde ssNMR experimenten voortgezet worden, waarmee in hoofdstuk 4 een begin werd gemaakt. Zulke experimenten zouden direct structurele informatie kunnen leveren zoals het residu-specifieke niveau van protonatie, waarmee verder inzicht verkregen kan worden in het moleculaire mechanisme van de kanaalfunctie via de chemical shifts van de protonen. Omdat protonen gevoeliger zijn voor de chemische omgeving, zoals fluctuaties van naburige aromatische ringen, dan koolstof- of stikstofkernen, kunnen ze waardevolle aanvullende informatie bieden in ssNMR, bijvoorbeeld in structuurberekeningen zoals beschreven in hoofdstuk 2. Voor de toekenning van de chemical shifts van protonen zal de ontwikkeling van verdere proton-gedetecteerde ssNMR experimenten nuttig zijn.

References

1. Membrane proteins. *Nat. Educ.* (2010). at <http://www.nature.com/scitable>
2. Hille, B. *Ion Channels of Excitable Membranes*. *Sinauer Assoc. inc.* (Sinauer Associates, inc. Publishers, 2001).
3. Kew, J. & Davies, C. *Ion channels : from structure to function*. (New York: Oxford University Press, 2009).
4. Pongs, O. Voltage-gated potassium channels: from hyperexcitability to excitement. *FEBS Lett.* **452,** 31–35 (1999).
5. Molina, M. L. *et al.* Clustering and coupled gating modulate the activity in KcsA, a potassium channel model. *J. Biol. Chem.* **281,** 18837–48 (2006).
6. Hegermann, J., Overbeck, J. & Schrempf, H. In vivo monitoring of the potassium channel KcsA in Streptomyces lividans hyphae using immuno-electron microscopy and energy-filtering transmission electron microscopy. *Microbiology* **152,** 2831–41 (2006).
7. Heginbotham, L., Lu, Z., Abramson, T. & MacKinnon, R. Mutations in the K+ channel signature sequence. *Biophys. J.* **66,** 1061–7 (1994).
8. Schrempf, H. *et al.* A prokaryotic potassium ion channel with two predicted transmembrane segments from Streptomyces lividans. *EMBO J.* **14,** 5170–8 (1995).
9. Zhou, Y., Morais-Cabral, J. H., Kaufman, A. & MacKinnon, R. Chemistry of ion coordination and hydration revealed by a K+ channel-Fab complex at 2.0 A resolution. *Nature* **414,** 43–48 (2001).
10. Zhou, Y. & MacKinnon, R. Ion binding affinity in the cavity of the KcsA potassium channel. *Biochemistry* **43,** 4978–82 (2004).
11. Doyle, D. A. *et al.* The structure of the potassium channel: molecular basis of K+ conduction and selectivity. *Science* **280,** 69–77 (1998).
12. Cordero-Morales, J. F. *et al.* Molecular determinants of gating at the potassium-channel selectivity filter. *Nat. Struct. Mol. Biol.* **13,** 311–318 (2006).
13. Cordero-Morales, J. F., Cuello, L. G. & Perozo, E. Voltage-dependent gating at the KcsA selectivity filter. *Nat. Struct. Mol. Biol.* **13,** 319–22 (2006).
14. Perozo, E., Cortes, D. M. & Cuello, L. G. Three-dimensional architecture and gating mechanism of a K+ channel studied by EPR spectroscopy. *Nat. Struct. Biol.* **5,** 459–69 (1998).
15. Blunck, R., Cordero-Morales, J. F., Cuello, L. G., Perozo, E. & Bezanilla, F. Detection of the opening of the bundle crossing in KcsA with fluorescence lifetime spectroscopy reveals the existence of two gates for ion conduction. *J. Gen. Physiol.* **128,** 569–81 (2006).
16. Gross, A., Columbus, L., Hideg, K., Altenbach, C. & Hubbell, W. L. Structure of the KcsA potassium channel from Streptomyces lividans: a site-directed spin labeling study of the second transmembrane segment. *Biochemistry* **38,** 10324–35 (1999).
17. Ader, C. *et al.* Coupling of activation and inactivation gate in a K+-channel: potassium and ligand sensitivity. *EMBO J.* **28,** 2825–34 (2009).
18. Ader, C. *et al.* A structural link between inactivation and block of a K+ channel. *Nat. Struct. Mol. Biol.* **15,** 605–612 (2008).
19. Cordero-Morales, J. F., Jogini, V., Chakrapani, S. & Perozo, E. A multipoint hydrogen-bond network underlying KcsA C-type inactivation. *Biophys. J.* **100,** 2387–93 (2011).
20. Cordero-Morales, J. F. *et al.* Molecular driving forces determining potassium channel slow inactivation. *Nat. Struct. Mol. Biol.* **14,** 1062–9 (2007).

21. Cuello, L. G., Jogini, V., Cortes, D. M. & Perozo, E. Structural mechanism of C-type inactivation in K(+) channels. *Nature* **466,** 203–208 (2010).
22. Cuello, L. G. *et al.* Structural basis for the coupling between activation and inactivation gates in K(+) channels. *Nature* **466,** 272–5 (2010).
23. Liu, Y. S., Sompornpisut, P. & Perozo, E. Structure of the KcsA channel intracellular gate in the open state. *Nat. Struct. Biol.* **8,** 883–7 (2001).
24. Chakrapani, S. *et al.* On the structural basis of modal gating behavior in K(+) channels. *Nat. Struct. Mol. Biol.* **18,** 67–74 (2011).
25. Escribá, P. V *et al.* Membranes: a meeting point for lipids, proteins and therapies. *J. Cell. Mol. Med.* **12,** 829–75 (2008).
26. Lee, A. G. How lipids affect the activities of integral membrane proteins. *Biochim. Biophys. Acta* **1666,** 62–87 (2004).
27. Marius, P. *et al.* Binding of anionic lipids to at least three nonannular sites on the potassium channel KcsA is required for channel opening. *Biophys. J.* **94,** 1689–98 (2008).
28. Tillman, T. S. & Cascio, M. Effects of membrane lipids on ion channel structure and function. *Cell Biochem. Biophys.* **38,** 161–90 (2003).
29. Xu, Y., Ramu, Y. & Lu, Z. Removal of phospho-head groups of membrane lipids immobilizes voltage sensors of K+ channels. *Nature* **451,** 826–9 (2008).
30. Zimmerberg, J. & Gawrisch, K. The physical chemistry of biological membranes. *Nat. Chem. Biol.* **2,** 564–7 (2006).
31. Heginbotham, L. Functional Reconstitution of a Prokaryotic K+ Channel. *J. Gen. Physiol.* **111,** 741–749 (1998).
32. Schmidt, D., Jiang, Q.-X. & MacKinnon, R. Phospholipids and the origin of cationic gating charges in voltage sensors. *Nature* **444,** 775–9 (2006).
33. Valiyaveetil, F. I., Zhou, Y. & MacKinnon, R. Lipids in the structure, folding, and function of the KcsA K+ channel. *Biochemistry* **41,** 10771–7 (2002).
34. Andrew, E. R., Bradbury, A. & Eades, R. G. Nuclear Magnetic Resonance Spectra from a Crystal rotated at High Speed. *Nature* **182,** 1659 (1958).
35. Laws, D. D., Bitter, H.-M. L. & Jerschow, A. Solid-state NMR spectroscopic methods in chemistry. *Angew. Chem. Int. Ed. Engl.* **41,** 3096–129 (2002).
36. Nand, D. Solid-state NMR on Complex Biomolecules: Novel Methods and Applications. (2011). doi:ISBN 978-90-393-5635-7
37. Baldus, M. Correlation experiments for assignment and structure elucidation of immobilized polypeptides under magic angle spinning. *Prog. Nucl. Magn. Reson. Spectrosc.* **41,** 1–47 (2002).
38. Schaefer, J. & Stejskal, E. O. Carbon-13 nuclear magnetic resonance of polymers spinning at the magic angle. *J. Am. Chem. Soc.* **98,** 1031–1032 (1976).
39. Baldus, M., Petkova, A. T., Herzfeld, J. & Griffin, R. G. Cross polarization in the tilted frame: assignment and spectral simplification in heteronuclear spin systems. *Mol. Phys.* **95,** 1197–1207 (1998).
40. Pines, A. Proton-Enhanced Nuclear Induction Spectroscopy. A Method for High Resolution NMR of Dilute Spins in Solids. *J. Chem. Phys.* **56,** 1776 (1972).
41. Overhauser, A. Polarization of Nuclei in Metals. *Phys. Rev.* **92,** 411–415 (1953).
42. Maly, T. *et al.* Dynamic nuclear polarization at high magnetic fields. *J. Chem. Phys.* **128,** 52211 (2008).
43. Rossini, A. J. *et al.* Dynamic nuclear polarization surface enhanced NMR spectroscopy. *Acc. Chem. Res.* **46,** 1942–51 (2013).

44. Ni, Q. Z. *et al.* High Frequency Dynamic Nuclear Polarization. (2013). at <http://pubs.acs.org.proxy.library.uu.nl/doi/abs/10.1021/ar300348n>
45. Salnikov, E. *et al.* Solid-state NMR spectroscopy of oriented membrane polypeptides at 100 K with signal enhancement by dynamic nuclear polarization. *J. Am. Chem. Soc.* **132,** 5940–5941 (2010).
46. Koers, E. J. *et al.* Dynamic Nuclear Polarization NMR Spectroscopy: Revealing Multiple Conformations in Lipid-Anchored Peptide Vaccines. *Angew. Chemie Int. Ed.* **52,** 10905–10908 (2013).
47. Barnes, A. B. *et al.* Cryogenic sample exchange NMR probe for magic angle spinning dynamic nuclear polarization. *J. Magn. Reson.* **198,** 261–270 (2009).
48. Linden, A. H. *et al.* Cryogenic temperature effects and resolution upon slow cooling of protein preparations in solid state NMR. *J. Biomol. NMR* **51,** 283–292 (2011).
49. Reggie, L., Lopez, J. J., Collinson, I., Glaubitz, C. & Lorch, M. Dynamic nuclear polarization-enhanced solid-state NMR of a 13C-labeled signal peptide bound to lipid-reconstituted Sec translocon. *J. Am. Chem. Soc.* **133,** 19084–19086 (2011).
50. Andreas, L. B. *et al.* Dynamic nuclear polarization study of inhibitor binding to the M2(18-60) proton transporter from influenza A. *Biochemistry* **52,** 2774–2782 (2013).
51. Renault, M. *et al.* Cellular solid-state nuclear magnetic resonance spectroscopy. *Proc. Natl. Acad. Sci. U. S. A.* (2012). doi:10.1073/pnas.1116478109
52. Takahashi, H. *et al.* Solid-State NMR on Bacterial Cells: Selective Cell Wall Signal Enhancement and Resolution Improvement using Dynamic Nuclear Polarization. *J. Am. Chem. Soc.* **135,** 5105–5110 (2013).
53. Wang, T. *et al.* Sensitivity-enhanced solid-state NMR detection of expansin's target in plant cell walls. *Proc. Natl. Acad. Sci. U. S. A.* **110,** 16444–16449 (2013).
54. Gelis, I. *et al.* Solid-state NMR enhanced by dynamic nuclear polarization as a novel tool for ribosome structural biology. *J. Biomol. NMR* **56,** 85–93 (2013).
55. Long, S. B., Tao, X., Campbell, E. B. & MacKinnon, R. Atomic structure of a voltage-dependent K+ channel in a lipid membrane-like environment. *Nature* **450,** 376–82 (2007).
56. Bezanilla, F. How membrane proteins sense voltage. *Nat. Rev. Mol. Cell Biol.* **9,** 323–32 (2008).
57. Baukrowitz, T. & Yellen, G. Modulation of K+ current by frequency and external [K+]: a tale of two inactivation mechanisms. *Neuron* **15,** 951–60 (1995).
58. Baukrowitz, T. & Yellen, G. Use-Dependent Blockers and Exit Rate of the Last Ion from the Multi-Ion Pore of a K+ Channel. *Science (80-.).* **271,** 653–656 (1996).
59. Panyi, G. & Deutsch, C. Cross talk between activation and slow inactivation gates of Shaker potassium channels. *J. Gen. Physiol.* **128,** 547–59 (2006).
60. Panyi, G. & Deutsch, C. Probing the cavity of the slow inactivated conformation of shaker potassium channels. *J. Gen. Physiol.* **129,** 403–18 (2007).
61. Liu, Y., Jurman, M. E. & Yellen, G. Dynamic rearrangement of the outer mouth of a K+ channel during gating. *Neuron* **16,** 859–67 (1996).
62. Larsson, H. P. & Elinder, F. A conserved glutamate is important for slow inactivation in K+ channels. *Neuron* **27,** 573–83 (2000).

63. Wang, D. T., Hill, A. P., Mann, S. A., Tan, P. S. & Vandenberg, J. I. Mapping the sequence of conformational changes underlying selectivity filter gating in the K(v)11.1 potassium channel. *Nat. Struct. Mol. Biol.* **18,** 35–41 (2011).
64. Broomand, A., Männikkö, R., Larsson, H. P. & Elinder, F. Molecular movement of the voltage sensor in a K channel. *J. Gen. Physiol.* **122,** 741–8 (2003).
65. Gandhi, C. S., Clark, E., Loots, E., Pralle, A. & Isacoff, E. Y. The orientation and molecular movement of a k(+) channel voltage-sensing domain. *Neuron* **40,** 515–25 (2003).
66. Lee, S.-Y., Banerjee, A. & MacKinnon, R. Two separate interfaces between the voltage sensor and pore are required for the function of voltage-dependent K(+) channels. *PLoS Biol.* **7,** e47 (2009).
67. Catterall, W. A. Ion channel voltage sensors: structure, function, and pathophysiology. *Neuron* **67,** 915–28 (2010).
68. Lange, A. *et al.* Toxin-induced conformational changes in a potassium channel revealed by solid-state NMR. *Nature* **440,** 959–62 (2006).
69. Schneider, R. *et al.* Solid-state NMR spectroscopy applied to a chimeric potassium channel in lipid bilayers. *J. Am. Chem. Soc.* **130,** 7427–7435 (2008).
70. Cuello, L. G. *et al.* Design and characterization of a constitutively open KcsA. *FEBS Lett.* **584,** 1133–8 (2010).
71. Uysal, S. *et al.* Crystal structure of full-length KcsA in its closed conformation. *Proc. Natl. Acad. Sci. U. S. A.* **106,** 6644–6649 (2009).
72. De Vries, S. J., van Dijk, M. & Bonvin, A. M. J. J. The HADDOCK web server for data-driven biomolecular docking. *Nat. Protoc.* **5,** 883–97 (2010).
73. Nand, D., Cukkemane, A., Becker, S. & Baldus, M. Fractional deuteration applied to biomolecular solid-state NMR spectroscopy. *J. Biomol. NMR* **52,** 91–101 (2012).
74. Brünger, A. T. *et al.* Crystallography & NMR system: A new software suite for macromolecular structure determination. *Acta Crystallogr. D. Biol. Crystallogr.* **54,** 905–21 (1998).
75. Zachariae, U. *et al.* The molecular mechanism of toxin-induced conformational changes in a potassium channel: relation to C-type inactivation. *Structure* **16,** 747–754 (2008).
76. Chakrapani, S., Cordero-Morales, J. F. & Perozo, E. A quantitative description of KcsA gating I: macroscopic currents. *J. Gen. Physiol.* **130,** 465–78 (2007).
77. Ader, C. *et al.* Structural rearrangements of membrane proteins probed by water-edited solid-state NMR spectroscopy. *J. Am. Chem. Soc.* **131,** 170–6 (2009).
78. Uysal, S. *et al.* Mechanism of activation gating in the full-length KcsA K+ channel. *Proc. Natl. Acad. Sci. U. S. A.* **108,** 11896–9 (2011).
79. Yifrach, O. & MacKinnon, R. Energetics of pore opening in a voltage-gated K(+) channel. *Cell* **111,** 231–9 (2002).
80. Weingarth, M. *et al.* Supramolecular structure of membrane-associated polypeptides by combining solid-state NMR and molecular dynamics simulations. *Biophys. J.* **103,** 29–37 (2012).
81. Hess, B., Kutzner, C., van der Spoel, D. & Lindahl, E. GROMACS 4: Algorithms for Highly Efficient, Load-Balanced, and Scalable Molecular Simulation. *J. Chem. Theory Comput.* **4,** 435–447 (2008).
82. Broomand, A., Osterberg, F., Wardi, T. & Elinder, F. Electrostatic domino effect in the Shaker K channel turret. *Biophys. J.* **93,** 2307–14 (2007).

83. Weingarth, M. *et al.* Structural determinants of specific lipid binding to potassium channels. *J. Am. Chem. Soc.* **135,** 3983–8 (2013).
84. Gajewski, C., Dagcan, A., Roux, B. & Deutsch, C. Biogenesis of the pore architecture of a voltage-gated potassium channel. *Proc. Natl. Acad. Sci. U. S. A.* **108,** 3240–5 (2011).
85. Seidel, K. *et al.* Protein solid-state NMR resonance assignments from (13C,13C) correlation spectroscopy. *Phys. Chem. Chem. Phys.* **6,** 5090–5093 (2004).
86. Fung, B. M., Khitrin, A. K. & Ermolaev, K. An improved broadband decoupling sequence for liquid crystals and solids. *J. Magn. Reson.* **142,** 97–101 (2000).
87. Soares, T. A. *et al.* An improved nucleic acid parameter set for the GROMOS force field. *J. Comput. Chem.* **26,** 725–737 (2005).
88. Berjanskii, M. V, Neal, S. & Wishart, D. S. PREDITOR: a web server for predicting protein torsion angle restraints. *Nucleic Acids Res.* **34,** W63–9 (2006).
89. Shen, Y. & Bax, A. SPARTA+: a modest improvement in empirical NMR chemical shift prediction by means of an artificial neural network. *J. Biomol. NMR* **48,** 13–22 (2010).
90. Van den Bogaart, G. *et al.* Membrane protein sequestering by ionic protein-lipid interactions. *Nature* **479,** 552–5 (2011).
91. Zheng, H., Liu, W., Anderson, L. Y. & Jiang, Q.-X. Lipid-dependent gating of a voltage-gated potassium channel. *Nat. Commun.* **2,** 250 (2011).
92. Milescu, M. *et al.* Interactions between lipids and voltage sensor paddles detected with tarantula toxins. *Nat. Struct. Mol. Biol.* **16,** 1080–5 (2009).
93. Phillips, R., Ursell, T., Wiggins, P. & Sens, P. Emerging roles for lipids in shaping membrane-protein function. *Nature* **459,** 379–85 (2009).
94. Eddy, M. T. *et al.* Lipid dynamics and protein-lipid interactions in 2D crystals formed with the β-barrel integral membrane protein VDAC1. *J. Am. Chem. Soc.* **134,** 6375–87 (2012).
95. Niemelä, P. S. *et al.* Membrane proteins diffuse as dynamic complexes with lipids. *J. Am. Chem. Soc.* **132,** 7574–5 (2010).
96. Domene, C., Bond, P. J., Deol, S. S. & Sansom, M. S. P. Lipid/protein interactions and the membrane/water interfacial region. *J. Am. Chem. Soc.* **125,** 14966–7 (2003).
97. Lee, A. G. Lipid-protein interactions. *Biochem. Soc. Trans.* **39,** 761–6 (2011).
98. Marius, P., Alvis, S. J., East, J. M. & Lee, A. G. The interfacial lipid binding site on the potassium channel KcsA is specific for anionic phospholipids. *Biophys. J.* **89,** 4081–9 (2005).
99. Marius, P., de Planque, M. R. R. & Williamson, P. T. F. Probing the interaction of lipids with the non-annular binding sites of the potassium channel KcsA by magic-angle spinning NMR. *Biochim. Biophys. Acta* **1818,** 90–6 (2012).
100. Miller, C. An overview of the potassium channel family. *Genome Biol.* **1,** REVIEWS0004 (2000).
101. Ramu, Y., Xu, Y. & Lu, Z. Enzymatic activation of voltage-gated potassium channels. *Nature* **442,** 696–9 (2006).
102. Marrink, S. J., Risselada, H. J., Yefimov, S., Tieleman, D. P. & de Vries, A. H. The MARTINI force field: coarse grained model for biomolecular simulations. *J. Phys. Chem. B* **111,** 7812–24 (2007).
103. Monticelli, L. *et al.* The MARTINI Coarse-Grained Force Field: Extension to Proteins. *J. Chem. Theory Comput.* **4,** 819–834 (2008).

104. Deol, S. S., Domene, C., Bond, P. J. & Sansom, M. S. P. Anionic phospholipid interactions with the potassium channel KcsA: simulation studies. *Biophys. J.* **90,** 822–30 (2006).
105. Huijbregts, R. P., de Kroon AI & de Kruijff B. Topology and transport of membrane lipids in bacteria. *Biochim. Biophys. Acta* **1469,** 43–61 (2000).
106. Alvis, S. J., Williamson, I. M., East, J. M. & Lee, A. G. Interactions of anionic phospholipids and phosphatidylethanolamine with the potassium channel KcsA. *Biophys. J.* **85,** 3828–38 (2003).
107. Raleigh, D. P., Levitt, M. H. & Griffin, R. G. Rotational resonance in solid state NMR. *Chem. Phys. Lett.* **146,** 71–76 (1988).
108. Weingarth, M., Bodenhausen, G. & Tekely, P. Broadband carbon-13 correlation spectra of microcrystalline proteins in very high magnetic fields. *J. Am. Chem. Soc.* **131,** 13937–9 (2009).
109. Weingarth, M., Tekely, P., Brüschweiler, R. & Bodenhausen, G. Improving the quality of 2D solid-state NMR spectra of microcrystalline proteins by covariance analysis. *Chem. Commun. (Camb).* **46,** 952–4 (2010).
110. Jiang, Y. *et al.* X-ray structure of a voltage-dependent K+ channel. *Nature* **423,** 33–41 (2003).
111. Lee, C. W. & Griffin, R. G. Two-dimensional 1H/13C heteronuclear chemical shift correlation spectroscopy of lipid bilayers. *Biophys. J.* **55,** 355–8 (1989).
112. Bernèche, S. & Roux, B. A gate in the selectivity filter of potassium channels. *Structure* **13,** 591–600 (2005).
113. Rotem, D., Mason, A. & Bayley, H. Inactivation of the KcsA potassium channel explored with heterotetramers. *J. Gen. Physiol.* **135,** 29–42 (2010).
114. Sackin, H., Nanazashvili, M., Li, H., Palmer, L. G. & Walters, D. E. An intersubunit salt bridge near the selectivity filter stabilizes the active state of Kir1.1. *Biophys. J.* **97,** 1058–66 (2009).
115. Iwamoto, M. & Oiki, S. Amphipathic antenna of an inward rectifier K+ channel responds to changes in the inner membrane leaflet. *Proc. Natl. Acad. Sci. U. S. A.* **110,** 749–54 (2013).
116. Bogdanov, M., Xie, J. & Dowhan, W. Lipid-protein interactions drive membrane protein topogenesis in accordance with the positive inside rule. *J. Biol. Chem.* **284,** 9637–41 (2009).
117. Bogdanov, M., Heacock, P., Guan, Z. & Dowhan, W. Plasticity of lipid-protein interactions in the function and topogenesis of the membrane protein lactose permease from Escherichia coli. *Proc. Natl. Acad. Sci. U. S. A.* **107,** 15057–62 (2010).
118. Vostrikov, V. V, Hall, B. A., Greathouse, D. V, Koeppe, R. E. & Sansom, M. S. P. Changes in transmembrane helix alignment by arginine residues revealed by solid-state NMR experiments and coarse-grained MD simulations. *J. Am. Chem. Soc.* **132,** 5803–11 (2010).
119. Schäfer, L. V *et al.* Lipid packing drives the segregation of transmembrane helices into disordered lipid domains in model membranes. *Proc. Natl. Acad. Sci. U. S. A.* **108,** 1343–8 (2011).
120. Periole, X., Knepp, A. M., Sakmar, T. P., Marrink, S. J. & Huber, T. Structural determinants of the supramolecular organization of G protein-coupled receptors in bilayers. *J. Am. Chem. Soc.* **134,** 10959–65 (2012).
121. Berger, O., Edholm, O. & Jähnig, F. Molecular dynamics simulations of a fluid bilayer of dipalmitoylphosphatidylcholine at full hydration, constant pressure, and constant temperature. *Biophys. J.* **72,** 2002–13 (1997).

122. Kandt, C., Ash, W. L. & Tieleman, D. P. Setting up and running molecular dynamics simulations of membrane proteins. *Methods* **41,** 475–88 (2007).
123. Weingarth, M., Bodenhausen, G. & Tekely, P. Probing the quenching of rotary resonance by PISSARRO decoupling. *Chem. Phys. Lett.* **502,** 259–265 (2011).
124. Peng, X., Libich, D., Janik, R., Harauz, G. & Ladizhansky, V. Dipolar chemical shift correlation spectroscopy for homonuclear carbon distance measurements in proteins in the solid state: application to structure determination and refinement. *J. Am. Chem. Soc.* **130,** 359–69 (2008).
125. Yellen, G. The voltage-gated potassium channels and their relatives. *Nature* **419,** 35–42 (2002).
126. Shimizu, H. *et al.* Global twisting motion of single molecular KcsA potassium channel upon gating. *Cell* **132,** 67–78 (2008).
127. Imai, S., Osawa, M., Takeuchi, K. & Shimada, I. Structural basis underlying the dual gate properties of KcsA. *Proc. Natl. Acad. Sci. U. S. A.* **107,** 6216–21 (2010).
128. Cuello, L. G., Jogini, V., Cortes, D. M. & Perozo, E. Structural mechanism of C-type inactivation in K(+) channels. *Nature* **466,** 203–8 (2010).
129. Domene, C., Klein, M. L., Branduardi, D., Gervasio, F. L. & Parrinello, M. Conformational changes and gating at the selectivity filter of potassium channels. *J. Am. Chem. Soc.* **130,** 9474–80 (2008).
130. Ostmeyer, J., Chakrapani, S., Pan, A. C., Perozo, E. & Roux, B. Recovery from slow inactivation in K+ channels is controlled by water molecules. *Nature* **501,** 121–4 (2013).
131. Van der Cruijsen, E. A. W. *et al.* Importance of lipid-pore loop interface for potassium channel structure and function. *Proc. Natl. Acad. Sci. U. S. A.* **110,** 13008–13 (2013).
132. Lange, A., Seidel, K., Verdier, L., Luca, S. & Baldus, M. Analysis of proton-proton transfer dynamics in rotating solids and their use for 3D structure determination. *J. Am. Chem. Soc.* **125,** 12640–8 (2003).
133. Weingarth, M., Demco, D. E., Bodenhausen, G. & Tekely, P. Improved magnetization transfer in solid-state NMR with fast magic angle spinning. *Chem. Phys. Lett.* **469,** 342–348 (2009).
134. Roux, B. & MacKinnon, R. The cavity and pore helices in the KcsA K+ channel: electrostatic stabilization of monovalent cations. *Science* **285,** 100–2 (1999).
135. Parthasarathy, S., Nishiyama, Y. & Ishii, Y. Sensitivity and resolution enhanced solid-state NMR for paramagnetic systems and biomolecules under very fast magic angle spinning. *Acc. Chem. Res.* **46,** 2127–35 (2013).
136. Zhou, D. H. & Rienstra, C. M. Rapid analysis of organic compounds by proton-detected heteronuclear correlation NMR spectroscopy with 40 kHz magic-angle spinning. *Angew. Chem. Int. Ed. Engl.* **47,** 7328–31 (2008).
137. McDermott, A. ., Creuzet, F. ., Kolbert, A. . & Griffin, R. . High-resolution magic-angle-spinning NMR spectra of protons in deuterated solids. *J. Magn. Reson.* **98,** 408–413 (1992).
138. Chevelkov, V., Rehbein, K., Diehl, A. & Reif, B. Ultrahigh resolution in proton solid-state NMR spectroscopy at high levels of deuteration. *Angew. Chem. Int. Ed. Engl.* **45,** 3878–81 (2006).
139. Shi, L., Kawamura, I., Jung, K.-H., Brown, L. S. & Ladizhansky, V. Conformation of a seven-helical transmembrane photosensor in the lipid environment. *Angew. Chem. Int. Ed. Engl.* **50,** 1302–5 (2011).

140. Zhou, D. H. *et al.* Solid-state NMR analysis of membrane proteins and protein aggregates by proton detected spectroscopy. *J. Biomol. NMR* **54,** 291–305 (2012).
141. Marchetti, A. *et al.* Backbone assignment of fully protonated solid proteins by 1H detection and ultrafast magic-angle-spinning NMR spectroscopy. *Angew. Chem. Int. Ed. Engl.* **51,** 10756–9 (2012).
142. Pan, a. C., Cuello, L. G., Perozo, E. & Roux, B. Thermodynamic coupling between activation and inactivation gating in potassium channels revealed by free energy molecular dynamics simulations. *J. Gen. Physiol.* **138,** 571–580 (2011).
143. Ritter, C. *et al.* Correlation of structural elements and infectivity of the HET-s prion. *Nature* **435,** 844–8 (2005).
144. Van Melckebeke, H. *et al.* Probing water accessibility in HET-s(218-289) amyloid fibrils by solid-state NMR. *J. Mol. Biol.* **405,** 765–72 (2011).
145. Popescu, G. K. Modes of glutamate receptor gating. *J. Physiol.* **590,** 73–91 (2012).
146. Weingarth, M. *et al.* Structural determinants of specific lipid binding to potassium channels. *J. Am. Chem. Soc.* **135,** 3983–8 (2013).
147. Hung, L. W. *et al.* Crystal structure of the ATP-binding subunit of an ABC transporter. *Nature* **396,** 703–7 (1998).
148. Angel, T. E., Chance, M. R. & Palczewski, K. Conserved waters mediate structural and functional activation of family A (rhodopsin-like) G protein-coupled receptors. *Proc. Natl. Acad. Sci. U. S. A.* **106,** 8555–60 (2009).
149. Schmidt, B., McCracken, J. & Ferguson-Miller, S. A discrete water exit pathway in the membrane protein cytochrome c oxidase. *Proc. Natl. Acad. Sci. U. S. A.* **100,** 15539–42 (2003).
150. Denisov, V. P., Peters, J., Hörlein, H. D. & Halle, B. Using buried water molecules to explore the energy landscape of proteins. *Nat. Struct. Biol.* **3,** 505–9 (1996).
151. Persson, F. & Halle, B. Transient access to the protein interior: simulation versus NMR. *J. Am. Chem. Soc.* **135,** 8735–48 (2013).
152. Ader, C., Pongs, O., Becker, S. & Baldus, M. Protein dynamics detected in a membrane-embedded potassium channel using two-dimensional solid-state NMR spectroscopy. *Biochim. Biophys. Acta* **1798,** 286–90 (2010).
153. Luo, W. & Hong, M. Conformational changes of an ion channel detected through water-protein interactions using solid-state NMR spectroscopy. *J. Am. Chem. Soc.* **132,** 2378–84 (2010).
154. Kumashiro, K. K. *et al.* A Novel Tool for Probing Membrane Protein Structure: Solid-State NMR with Proton Spin Diffusion and X-Nucleus Detection. *J. Am. Chem. Soc.* **120,** 5043–5051 (1998).
155. Weingarth, M., Tekely, P. & Bodenhausen, G. Efficient heteronuclear decoupling by quenching rotary resonance in solid-state NMR. *Chem. Phys. Lett.* **466,** 247–251 (2008).
156. Weingarth, M., Bodenhausen, G. & Tekely, P. Low-power decoupling at high spinning frequencies in high static fields. *J. Magn. Reson.* **199,** 238–41 (2009).
157. Zhou, D. H. & Rienstra, C. M. High-performance solvent suppression for proton detected solid-state NMR. *J. Magn. Reson.* **192,** 167–172 (2008).
158. Shaw, D. E. *et al.* Millisecond-scale molecular dynamics simulations on Anton. in *Proc. Conf. High Perform. Comput. Networking, Storage Anal. - SC '09* 1 (ACM Press, 2009). doi:10.1145/1654059.1654099

159. Perozo, E. Structural Rearrangements Underlying K+-Channel Activation Gating. *Science (80-.).* **285,** 73–78 (1999).
160. Cuello, L. G., Romero, J. G., Cortes, D. M. & Perozo, E. pH-dependent gating in the Streptomyces lividans K+ channel. *Biochemistry* **37,** 3229–36 (1998).
161. Heginbotham, L. Single Streptomyces lividans K+ Channels: Functional Asymmetries and Sidedness of Proton Activation. *J. Gen. Physiol.* **114,** 551–560 (1999).
162. Meuser, D., Splitt, H., Wagner, R. & Schrempf, H. Exploring the open pore of the potassium channel from Streptomyces lividans. *FEBS Lett.* **462,** 447–452 (1999).
163. Olofsson, G. & Sparr, E. Ionization constants pKa of cardiolipin. *PLoS One* **8,** e73040 (2013).
164. Chakrapani, S., Cordero-Morales, J. F. & Perozo, E. A quantitative description of KcsA gating II: single-channel currents. *J. Gen. Physiol.* **130,** 479–496 (2007).
165. Irizarry, S. N., Kutluay, E., Drews, G., Hart, S. J. & Heginbotham, L. Opening the KcsA K + Channel: Tryptophan Scanning and Complementation Analysis Lead to Mutants with Altered Gating †. *Biochemistry* **41,** 13653–13662 (2002).
166. Keim, P., Vigna, R. A., Morrow, J. S., Marshall, R. C. & Gurd, F. R. Carbon 13 nuclear magnetic resonance of pentapeptides of glycine containing central residues of serine, threonine, aspartic and glutamic acids, asparagine, and glutamine. *J. Biol. Chem.* **248,** 7811–8 (1973).
167. Dalmas, O., Hyde, H. C., Hulse, R. E. & Perozo, E. Symmetry-constrained analysis of pulsed double electron-electron resonance (DEER) spectroscopy reveals the dynamic nature of the KcsA activation gate. *J. Am. Chem. Soc.* **134,** 16360–9 (2012).
168. Hulse, R. E. *et al.* Conformational Dynamics at the Inner Gate of KcsA during Activation. *Biochemistry* **53,** 2557–9 (2014).
169. Imai, S. *et al.* Functional equilibrium of the KcsA structure revealed by NMR. *J. Biol. Chem.* **287,** 39634–41 (2012).
170. Sigworth, F. J. & Sine, S. M. Data transformations for improved display and fitting of single-channel dwell time histograms. *Biophys. J.* **52,** 1047–54 (1987).
171. Hall, D. A. *et al.* Polarization-enhanced NMR spectroscopy of biomolecules in frozen solution. *Science (80-.).* **276,** 930–932 (1997).
172. Ardenkjaer-Larsen, J. H. *et al.* Increase in signal-to-noise ratio of > 10,000 times in liquid-state NMR. *Proc. Natl. Acad. Sci. U. S. A.* **100,** 10158–10163 (2003).
173. Gallagher, F. A. *et al.* Magnetic resonance imaging of pH in vivo using hyperpolarized 13C-labelled bicarbonate. *Nature* **453,** 940–943 (2008).
174. Cassidy, M. C., Chan, H. R., Ross, B. D., Bhattacharya, P. K. & Marcus, C. M. In-vivo magnetic resonance imaging of hyperpolarized silicon particles. (2013). at <http://arxiv.org/abs/1305.3332>
175. Lauterbur, P. C. Image formation by induced local interactions. Examples employing nuclear magnetic resonance. *Nature* 190–191 (1973). at 176. Otting, G. Protein NMR using paramagnetic ions. *Annu. Rev. Biophys.* **39,** 387–405 (2010).
177. Bertini, I., Luchinat, C., Parigi, G. & Pierattelli, R. NMR spectroscopy of paramagnetic metalloproteins. *Chembiochem* **6,** 1536–49 (2005).

178. Buffy, J. J. *et al.* Solid-state NMR investigation of the depth of insertion of protegrin-1 in lipid bilayers using paramagnetic Mn2+. *Biophys. J.* **85,** 2363–2373 (2003).
179. Nadaud, P. S., Helmus, J. J., Höfer, N. & Jaroniec, C. P. Long-Range Structural Restraints in Spin-Labeled Proteins Probed by Solid-State Nuclear Magnetic Resonance Spectroscopy. *J. Am. Chem. Soc.* **129,** 7502–7503 (2007).
180. Wickramasinghe, N. P. *et al.* Nanomole-scale protein solid-state NMR by breaking intrinsic 1HT1 boundaries. *Nat. Methods* **6,** 215–8 (2009).
181. Matsuki, Y. *et al.* Dynamic nuclear polarization experiments at 14.1 T for solid-state NMR. *Phys. Chem. Chem. Phys.* **12,** 5799–5803 (2010).
182. Barnes, A. B. *et al.* Dynamic nuclear polarization at 700MHz/460GHz. *J. Magn. Reson.* **224,** 1–7 (2012).
183. Uysal, S. *et al.* Crystal structure of full-length KcsA in its closed conformation. *Proc. Natl. Acad. Sci. U. S. A.* **106,** 6644–9 (2009).
184. Schneider, R. *et al.* Solid-state NMR spectroscopy applied to a chimeric potassium channel in lipid bilayers. *J. Am. Chem. Soc.* **130,** 7427–35 (2008).
185. Weingarth, M. *et al.* Quantitative analysis of the water occupancy around the selectivity filter of a K+ channel in different gating modes. *J. Am. Chem. Soc.* **136,** 2000–7 (2014).
186. Rosay, M. *et al.* Solid-state dynamic nuclear polarization at 263 GHz: spectrometer design and experimental results. *Phys. Chem. Chem. Phys.* **12,** 5850–5860 (2010).
187. Hohwy, M., Rienstra, C. M., Jaroniec, C. P. & Griffin, R. G. Fivefold symmetric homonuclear dipolar recoupling in rotating solids: Application to double quantum spectroscopy. *J. Chem. Phys.* **110,** 7983 (1999).
188. Sengupta, I., Nadaud, P. S., Helmus, J. J., Schwieters, C. D. & Jaroniec, C. P. Protein fold determined by paramagnetic magic-angle spinning solid-state NMR spectroscopy. *Nat. Chem.* **4,** 410–417 (2012).
189. Hocking, H. G., Zangger, K. & Madl, T. Studying the structure and dynamics of biomolecules by using soluble paramagnetic probes. *ChemPhysChem* **14,** 3082–94 (2013).
190. Esposito, G. *et al.* Probing protein structure by solvent perturbation of nuclear magnetic resonance spectra. *J. Mol. Biol.* **224,** 659–670 (1992).
191. Pintacuda, G. & Otting, G. Identification of Protein Surfaces by NMR Measurements with a Paramagnetic Gd(III) Chelate. *J. Am. Chem. Soc.* **124,** 372–373 (2002).
192. Bernini, A. *et al.* NMR studies of lysozyme surface accessibility by using different paramagnetic relaxation probes. *J. Am. Chem. Soc.* **128,** 9290–1 (2006).
193. Luca, S., Heise, H., Lange, A. & Baldus, M. Investigation of ligand-receptor systems by high-resolution solid-state NMR: recent progress and perspectives. *Arch. Pharm. (Weinheim).* **338,** 217–228 (2005).
194. Havlin, R. H. & Tycko, R. Probing site-specific conformational distributions in protein folding with solid-state NMR. *Proc. Natl. Acad. Sci. U. S. A.* **102,** 3284–9 (2005).
195. Siemer, A. B., Huang, K.-Y. & McDermott, A. E. Protein linewidth and solvent dynamics in frozen solution NMR. *PLoS One* **7,** e47242 (2012).
196. Zachariae, U. *et al.* The molecular mechanism of toxin-induced conformational changes in a potassium channel: relation to C-type inactivation. *Structure* **16,** 747–54 (2008).

197. Kagawa, A., Murokawa, Y., Takeda, K. & Kitagawa, M. Optimization of 1H spin density for dynamic nuclear polarization using photo-excited triplet electron spins. *J. Magn. Reson.* **197,** 9–13 (2009).
198. Akbey, Ü. *et al.* Dynamic nuclear polarization of deuterated proteins. *Angew. Chemie Int. Ed.* **49,** 7803–7806 (2010).
199. Linden, A. H. *et al.* Neurotoxin II Bound to Acetylcholine Receptors in Native Membranes. *J. Am. Chem. Soc.* **133,** 19266–19269 (2011).
200. Renault, M. *et al.* Solid-state NMR spectroscopy on cellular preparations enhanced by dynamic nuclear polarization. *Angew. Chem. Int. Ed. Engl.* **51,** 2998–3001 (2012).
201. Jacso, T. *et al.* Characterization of membrane proteins in isolated native cellular membranes by dynamic nuclear polarization solid-state NMR spectroscopy without purification and reconstitution. *Angew. Chem. Int. Ed. Engl.* **51,** 432–435 (2012).
202. Solomon, I. Relaxation Processes in a System of Two Spins. *Phys. Rev.* **99,** 559–565 (1955).
203. Bloembergen, N. & Morgan, L. O. Proton Relaxation Times in Paramagnetic Solutions. Effects of Electron Spin Relaxation. *J. Chem. Phys.* **34,** 842 (1961).
204. Van der Wel, P. C. a, Hu, K.-N., Lewandowski, J. & Griffin, R. G. Dynamic nuclear polarization of amyloidogenic peptide nanocrystals: GNNQQNY, a core segment of the yeast prion protein Sup35p. *J. Am. Chem. Soc.* **128,** 10840–10846 (2006).
205. Hu, K. N., Debelouchina, G. T., Smith, A. A. & Griffin, R. G. Quantum mechanical theory of dynamic nuclear polarization in solid dielectrics. *J. Chem. Phys.* **134,** 125105+ (2011).
206. Sauvée, C. *et al.* Highly Efficient, Water-Soluble Polarizing Agents for Dynamic Nuclear Polarization at High Frequency. *Angew. Chem. Int. Ed. Engl.* (2013). doi:10.1002/anie.201304657
207. Haze, O., Corzilius, B., Smith, A. a, Griffin, R. G. & Swager, T. M. Water-soluble narrow-line radicals for dynamic nuclear polarization. *J. Am. Chem. Soc.* **134,** 14287–14290 (2012).
208. Rossini, A. J. *et al.* Dynamic nuclear polarization surface enhanced NMR spectroscopy. *Acc. Chem. Res.* **46,** 1942–51 (2013).
209. Maly, T., Cui, D., Griffin, R. G. & Miller, A.-F. 1H dynamic nuclear polarization based on an endogenous radical. *J. Phys. Chem. B* **116,** 7055–7065 (2012).
210. Zagdoun, A. *et al.* Improved dynamic nuclear polarization surface-enhanced NMR spectroscopy through controlled incorporation of deuterated functional groups. *Angew. Chem. Int. Ed. Engl.* **52,** 1222–5 (2013).
211. Kagawa, A., Murokawa, Y., Takeda, K. & Kitagawa, M. Optimization of 1H spin density for dynamic nuclear polarization using photo-excited triplet electron spins. *J. Magn. Reson.* **197,** 9–13 (2009).
212. Shen, Y. & Bax, A. SPARTA+: a modest improvement in empirical NMR chemical shift prediction by means of an artificial neural network. *J. Biomol. NMR* **48,** 13–22 (2010).
213. Giepmans, B. N. G., Adams, S. R., Ellisman, M. H. & Tsien, R. Y. The fluorescent toolbox for assessing protein location and function. *Science* **312,** 217–24 (2006).
214. Reiner, A. & Isacoff, E. Y. The Brain Prize 2013: the optogenetics revolution. *Trends Neurosci.* **36,** 557–60 (2013).

215. Buurmans, I. L. C. *et al.* Catalytic activity in individual cracking catalyst particles imaged throughout different life stages by selective staining. *Nat. Chem.* **3,** 862–7 (2011).
216. Griffin, R. G. & Prisner, T. F. High field dynamic nuclear polarization--the renaissance. *Phys. Chem. Chem. Phys.* **12,** 5737–40 (2010).
217. Song, C., Hu, K.-N., Joo, C.-G., Swager, T. M. & Griffin, R. G. TOTAPOL: A Biradical Polarizing Agent for Dynamic Nuclear Polarization Experiments in Aqueous Media. *J. Am. Chem. Soc.* **128,** 11385–11390 (2006).
218. Vitzthum, V. *et al.* Fractional spin-labeling of polymers for enhancing NMR sensitivity by solvent-free dynamic nuclear polarization. *Chemphyschem* **12,** 2929–2932 (2011).
219. Hubbell, W. L., Cafiso, D. S. & Altenbach, C. Identifying conformational changes with site-directed spin labeling. *Nat. Struct. Biol.* **7,** 735–9 (2000).
220. Klare, J. P. & Steinhoff, H.-J. Spin labeling EPR. *Photosynth. Res.* **102,** 377–90
221. Hu, K.-N., Song, C., Yu, H.-H., Swager, T. M. & Griffin, R. G. High-frequency dynamic nuclear polarization using biradicals: a multifrequency EPR lineshape analysis. *J. Chem. Phys.* **128,** 52302 (2008).
222. Polyhach, Y., Bordignon, E. & Jeschke, G. Rotamer libraries of spin labelled cysteines for protein studies. *Phys. Chem. Chem. Phys.* **13,** 2356–66 (2011).
223. Sato, H. *et al.* Impact of electron-electron spin interaction on electron spin relaxation of nitroxide diradicals and tetraradical in glassy solvents between 10 and 300 k. *J. Phys. Chem. B* **112,** 2818–28 (2008).
224. Zagdoun, A. *et al.* Large molecular weight nitroxide biradicals providing efficient dynamic nuclear polarization at temperatures up to 200 K. *J. Am. Chem. Soc.* **135,** 12790–7 (2013).
225. Kaptein, R., Dijkstra, K. & Nicolay, K. Laser photo-CIDNP as a surface probe for proteins in solution. *Nature* **274,** 293–4 (1978).
226. Barnes, A. B. & Corzilius, B. Resolution and polarization distribution in cryogenic DNP/MAS experiments. *Phys. Chem. …* **12,** 5861–5867 (2010).
227. Fleissner, M. R. *et al.* Site-directed spin labeling of a genetically encoded unnatural amino acid. *Proc. Natl. Acad. Sci. U. S. A.* **106,** 21637–42 (2009).
228. Cassidy, M. C., Chan, H. R., Ross, B. D., Bhattacharya, P. K. & Marcus, C. M. In vivo magnetic resonance imaging of hyperpolarized silicon particles. *Nat. Nanotechnol.* **8,** 363–8 (2013).
229. Morais-Cabral, J. H., Zhou, Y. & MacKinnon, R. Energetic optimization of ion conduction rate by the K+ selectivity filter. *Nature* **414,** 37–42 (2001).

Acknowledgements

When I look back at this period of 4 years, it was a great adventure, inside the Bloembergen building as well as outside this bunker. Where people around me took a very important place within the projects I worked on and in the support I received from colleagues, friends and family. This makes this acknowledgement really justified.

First of all, I thank my supervisor Marc Baldus for the interesting projects he ensured me with, his support and creating a collaborative team with specialized people to accelerate and widen the projects.

Besides all collaboration within the university with Alexandre Bonvin and Antoinette Killian, I would also like to thank Eduardo Perozo, Benoît Roux, Raymond Hulse, Jared Ostmeyer (University of Chicago), Claire Sauvée, Olivier Ouri and Paul Tordo (Aix-Marseille University), Olaf Pongs (Saarland University), Melanie Rosay, Werner Maas (Bruker BioSpin Corporation) for all their input the last 4 years.

Before I started my PhD, I was already intrigued by NMR, so I take this opportunity to thank Martin Jäger, Ruud Aspers, Maria van Dongen and Cor de Korte for introducing me to NMR.

At the beginning of my PhD, I start trying to express KcsA, but this did not go really smoothly. Now we can speak of a "KcsA factory" at the Bloembergen building. For this, I have to thank Abhishek Cukkemane and Mark Daniels for all the (wet lab) support. Deepak, thank you for introducing me to the ion channels KcsA.

Markus, I would like to thank you for your always positive support, your deep ssNMR knowledge and for your KcsA simulations. Thanks to Eline, our DNP expert, for measuring the DNP related samples and pushing me to put on my running shoes….

Sasha "proteases" Prokofyev, It was a pleasure to work together with you in the KcsA factory and I would like to thank you for your contribution on the functional part of KcsA.

I want to thank Klaartje for sharing your knowledge and our collaboration with the KcsA-dynamics project.

Kitty and Sylke, Master students and of course being member of the KcsA Factory, I really enjoyed your presence as well as boosting the output of the project and making it your own.

Tessa, my office mate, my source for small questions, I will miss our candy-spot and thanks for the help with the Dutch summary of this thesis. Lindsay thanks for all the checks on my English. Deni, you can do it! Mohammed, Sabine, thanks for the discussions and for the nice atmosphere in the lab. Johan, thank you for your support in having "operating" systems including my computer. Barbara, many thanks for all the bureaucratic help. I thank Rolf Boelens, Alexandre Bonvin and

Rob Kaptein for their useful remarks in our regular group seminars and all the NMR research group members for their friendliness and creating a pleasant atmosphere to do science.
As team manager, I was quite proud of our "Balvin" team, except for our 17-0 defeat once… Thanks to Darkus, sliding Mohammed, kamikaze Adrien, Koen, Ermanimal, our pink shirt keeper Gydo, Rockdrigo, our (top)striker Mark and our top scorer João we had a great indoor futsal team.
Ook zou ik graag mijn vrienden willen bedanken voor de steun en nog belangrijker voor de nodige afleiding. De Sjampoos, Mirjam en Peter, Laurens en Mijke, Josien en Erwin, Frank en Anneleen, Jorien en Gerard, Mark en José, Kampong Zaterdag 2.
Verder heb ik gedurende mijn PhD veel steun gehad van mijn schoonfamilie, bedankt Jan en Mannie, Timon en Elsemiek en natuurlijk Oma Burgers. Bedankt voor alle steun en interesse van mijn broer en zus en de leuke afleiding door mijn neefje en nichtjes. Miquèl en Wendy, Mariëlle en Hans Peter, Sam, Fleur, Melanie, Naomi en Milan.

Een speciale dank aan mijn ouders, Ton en Trude, die altijd mijn sterke punten bleven zien waardoor ik met zelfvertrouwen het schoolsysteem doorliep tot en met dit proefschrift.

En nu, mijn grootste steun door dik en dun, mijn vrouw, Jorien, bedankt voor het bijsturen en voor het besef dat er ook nog andere dingen zijn dan werken. Ondanks dat ik je geduld aardig op de proef stelde door vaak laat thuis te komen, stond het eten altijd klaar. Zonder jou zou mijn PhD periode veel zwaarder zijn geweest. Ik kijk uit naar het avontuur dat we hierna aangaan! Niet met ons tweeën maar met ons drieën.

Curriculum Vitae

Elwin van der Cruijsen was born January 18, 1985 in Schoonhoven, the Netherlands. From 2004 to 2008, he did his Bachelor (HLO) of Chemistry in Deventer at the Hogeschool Saxion. His bachelor graduation project was done at Schering Plough/Organon in Oss under the supervision of Prof. Dr. Martin Jäger and Ing. Ruud Aspers and titled "Study on the Conformation of testosterone with NMR". In 2008 he moved to Amsterdam to complete a Masters in Chemistry, analytical sciences track, at the Free University. His Master graduation project at MSD/Solvay under the supervision of Dr. Maria van Dongen and Ing. Cor de Korte was titled "Application of NMR experiments for measurement of long-range heteronuclear coupling constants in small molecules at natural abundance, in relation to molecular conformation". After graduation in the summer of 2010, he worked as PhD student in the solid-state NMR group of Prof. Dr. Marc Baldus at the Bijvoet Center for Biomolecular Research at Utrecht University until October 2014. In the NMR Spectroscopy Research Group, he focused on the relationship between function and structure of potassium channels. He used solid-state NMR to dissect protein structure & dynamics in membranes during the gating cycle of a potassium channel.

List of publications

Work presented in this thesis is based on the following publications or manuscripts:

M. Weingarth, A. Prokofyev, **E.A.W. van der Cruijsen**, D. Nand, A.M.J.J. Bonvin, O. Pongs, M. Baldus, Structural determinants of specific lipid binding to potassium channels.
Journal of the American chemical society 2013 Feb 135(10):3983–88

E.A.W. van der Cruijsen*, D. Nand*, M. Weingarth, A. Prokofyev, S. Hornig, A.A. Cukkemane, A.M.J.J. Bonvin, S. Becker, R.E. Hulse, E. Perozo, O. Pongs, M. Baldus, The importance of the lipid-pore loop interface for potassium channel structure and function.
Proceedings of the National Academy of Sciences of the U S A. 2013 Aug 6;110(32):13008-13

M. Weingarth, **E.A.W. van der Cruijsen**, J. Ostmeyer, S. Lievestro, B. Roux, M. Baldus, Quantitative analysis of the water occupancy around the selectivity filter of a K+ channel in different gating modes.
Journal of the American chemical society 2013 Feb 135(10):3983–88

E.A.W. van der Cruijsen*, E.J. Koers*, R.E. Hulse, E. Perozo, M. Baldus, Biomolecular DNP- supported NMR spectroscopy using site-directed spin labeling.
Under review

E.J. Koers*, **E.A.W. van der Cruijsen***, M. Rosay, M. Weingarth, A. Prokofyev, C. Sauvée, O. Ouari, O. Pongs, P. Tordo, W.E. Maas, Marc Baldus, NMR-Based structural biology enhanced by Dynamic Nulear Polarization at high magnetic fields.
Under review

A. Prokofyev*, **E.A.W. van der Cruijsen***, O. Pongs, M. Baldus : Open-conductive conformation of KcsA potassium channel: functional and structural aspects.
Manuscript in preparation

* - Contributed equally